Assessment of Battery Capacity Fading in Partially-Decoupled Battery-Supercapacitor Hybrid Energy Storage System Topologies for Electric Vehicles

by

Ahmad Abuaish

A thesis
presented to the University of Waterloo
in fulfillment of the
thesis requirement for the degree of
Masters of Applied Science
in
Electrical and Computer Engineering

Waterloo, Ontario, Canada

© Ahmad Abuaish 2016

AUTHOR'S DECLARATION

I hereby declare that I am the sole author of this thesis. This is a true copy of the thesis, including any required final revisions, as accepted by my examiners.

I understand that my thesis may be made electronically available to the public.

Abstract

Battery energy storage system (ESS) is a major component of an electric vehicle (EV), as it supplies the entire propulsion power, constitutes a significant share of the EV's cost and weight, and plays a key role in EV performance. Consequently, extending the battery lifetime is vital, given that batteries in EV propulsion applications experience accelerated capacity fading due to aggressive traction demand and regenerative braking power spikes. Subsequently, it is beneficial to relieve the battery stress by adopting a hybrid energy storage scheme that combines the battery pack with an auxiliary energy storage device of high specific power such as supercapacitor (SC). The SC is used as a power buffer to process the high-frequency component of the traction demand and regenerative braking power.

There are many topologies through which the battery and SC can be interfaced with the DC bus. Two partially-decoupled topologies have proved to be the most promising candidate topologies for a hybrid energy storage system (HESS). In the first HESS topology, the battery is connected directly to the DC bus and the SC is interfaced with the DC bus through a DC/DC converter, whereas in the second topology, the SC is connected directly to the DC bus and the battery is interfaced with the DC bus through a DC/DC converter with a bypass diode. Comparative assessment of these topologies in terms of battery capacity fading based on a qualitative analysis is unclear and inconclusive. Therefore, a quantitative analysis is necessary to assess the pros and cons of these HESS topologies in comparison with one another.

Generally, HESS is most effective in urban drive cycles rather than highway drive cycles, due to the more frequent occurrence and higher intensity of regenerative braking in urban drive cycles, as the SC is dedicated to processing the generative braking energy. From the study reported in this thesis, it is observed that the second topology is superior to the first topology in extending the battery lifetime. For the same battery pack size in the second HESS topology and battery-only ESS, the battery lifetime in HESS is extended by 18, 4.5, and 8.7% for urban, highway, and urban-highway hybrid drive cycles, respectively, with respect to battery-only ESS. However, for battery-only ESS with an extended battery pack with a monetary value equivalent to that of the second HESS topology, the battery pack lifetime of the former is longer than the latter.

In this thesis, an onboard integrated charger scheme is proposed, which eliminates the active rectifier in the original onboard charger, yielding significant cost savings. In the integrated charger scheme, the traction inverter and HESS DC/DC converter are used to realize the two-stage charger topology. Also, two single-pole-double-throw (SPDT) switches are added between the traction inverter and motor, which connect the

inverter to the motor during propulsion and to the charger outlet during charging. Further, it is observed that HESS lifetime is about 4% higher compared to that of the battery-only ESS with and extended battery pack, where the monetary value of battery pack extension is equal to the cost of the SC minus the cost of the original active rectifier.

Acknowledgements

First and foremost, I would like to start by expressing my deepest gratitude to my parents, Kawther and Yousuf for their endless love and support as well as their encouragement that motivated me to pursue my graduate studies. I am also grateful for my siblings, Sameera, Rashad, Mohammad, and Yara for being there for me whenever I needed someone to talk to. Thank you, Rashad, for your invaluable guidance and encouragement during my tough days.

I would like to express my sincere gratitude to my supervisor Dr. Mehrdad Kazerani for his invaluable supervision. His close guidance, patience, and encouragement have helped me tremendously and kept me on track to complete this thesis.

Also, I would like to acknowledge the financial support I received from the Ministry of Higher Education of Saudi Arabia, without which my graduate studies would have been impossible.

Dedication

To my family…

Table of Contents

AUTHOR'S DECLARATION ii
Abstract iii
Acknowledgements v
Dedication vi
Table of Contents vii
List of Figures ix
List of Tables xii
Acronyms xiii
Chapter 1 Introduction 1
1.1 Motivation 1
1.2 Literature Review 3
1.2.1 HESS topologies 5
1.3 Objectives 10
1.4 Thesis Outline 10
Chapter 2 Background 11
2.1 Battery 11
2.1.1 Definitions 13
2.1.2 Battery electrical model 16
2.1.3 Battery thermal model 19
2.1.4 Battery capacity fading model 20
2.2 Supercapacitor (SC) 23
2.3 Traction powertrain 25
2.3.1 Traction propulsion demand 25
2.3.2 Transmission 27
2.3.3 Electric motor 27
2.3.4 Traction DC/AC converter (inverter) 32
2.3.5 Minimum value of DC bus voltage 34
2.3.6 DC/DC converter 34
2.4 Dynamic programming 39
Chapter 3 Simulation Results and Discussion 42
3.1 Simulation models parameters 42

3.2 Energy management 47
3.2.1 SC-DC simplified model 48
3.2.2 Bat-DC simplified model 49
3.3 Case study 1: effect of drive cycle type and initial SC SoC 51
3.4 Case study 2: effect of restricting final SC SoC 61
3.5 Case study 3: effect of realistic urban-highway hybrid drive cycle 63
3.6 Case study 4: effect of increasing the battery pack size in battery-only ESS for extending the battery lifetime 65
3.7 Summary 66
Chapter 4 Integrated Charger 68
Chapter 5 Conclusion 73
5.1 Summary 73
5.2 Contributions 74
5.3 Future Work 74
Appendix A 75
References 76

List of Figures

Figure 1.1: Traction power demand at the DC bus of the traction inverter 2
Figure 1.2: Specific energy and power map of various ESSs and fuel cell [15] 3
Figure 1.3: Battery-Supercapacitor Hybrid Energy Storage System Topologies: (a) passive, (b) partially-decoupled with battery DC bus connection, (c) partially-decoupled with SC DC bus connection, (d) cascaded fully-decoupled with SC connected downstream, (e) cascaded fully-decoupled with battery connected downstream, and (f) fully-decoupled 6
Figure 1.4: Proposed partially-decoupled HESS topology in [10], [24] 8
Figure 2.1: Ragone plot: specific energy and specific power of various batteries [30] 11
Figure 2.2: Performance comparison of Li-ion batteries [34] 13
Figure 2.3: Discharge characteristics at room temperature of the battery cell APR18650 manufactured by A123 Systems [37] 14
Figure 2.4: Battery cell electrical equivalent circuit model 16
Figure 2.5: Pulse current relaxation technique for battery parameters characterization 17
Figure 2.6: Cylindrical battery lumped thermal model [41] 19
Figure 2.7: Electrical equivalent circuit of battery cell thermal model 20
Figure 2.8: Cycle life performance at 100% DoD for different operating temperatures and discharge C-rates of the battery cell ANR26650 manufactured by A123 Systems [42] 21
Figure 2.9: Discharge cycle current waveform 21
Figure 2.10: Supercapacitor equivalent circuit model [43] 24
Figure 2.11: Traction powertrain of EVs with partially-decoupled HESS 25
Figure 2.12: Vehicle forces free body diagram [44] 26
Figure 2.13: Ideal torque-speed characteristics of vehicles power plant 28
Figure 2.14: IC engines torque-speed characteristics [45] 28
Figure 2.15: Induction machine per-phase equivalent circuit model 29
Figure 2.16: Thevenin equivalent circuit of IM 30
Figure 2.17: Traction inverter connected to IM 33
Figure 2.18: IM torque-speed characteristics for various synchronous speed values at constant V/F ratio 34
Figure 2.19: Half-bridge converter 35
Figure 2.20: I-V characteristics of SKM 300GB066D module: (a) IGBT, and (b) diode [49] 36
Figure 2.21: DC/DC converter currents during boost operation (pu): (a) inductor, (b) IGBT, and (c) Diode 37

Figure 2.22: DP of single state system 41
Figure 3.1: Simplified block diagram of the simulation model 42
Figure 3.2: Combined inverter-motor system efficiency map 44
Figure 3.3: DC/DC converter efficiency map 46
Figure 3.4: Simplified SC-DC equivalent circuit model 49
Figure 3.5: Simplified Bat-DC equivalent circuit model: (a) bypass diode not conducting, and (b) bypass diode conducting 51
Figure 3.6: Simulation drive cycles: (a) urban and (b) highway 52
Figure 3.7: Battery capacity loss after a single urban drive cycle with different SC pack dimensions: (a) SC-DC topology and (b) Bat-DC topology 55
Figure 3.8: System states and control trajectories with 100% initial SC SoC for (a) SC-DC topology in urban driving, (b) SC-DC topology in highway driving, (c) Bat-DC topology in urban driving, (d) Bat-DC topology in highway driving 56
Figure 3.9: Battery normalized capacity versus number of drive cycles with 100% initial SC SoC for (a) urban drive cycle and (b) highway drive cycle 58
Figure 3.10: Normalized battery capacity versus number of drive cycles with 45% SC initial SoC for (a) urban drive cycle and (b) highway drive cycle 59
Figure 3.11: System states and control trajectories with 45% SC initial SoC for (a) SC-DC topology in urban driving, (b) SC-DC topology in highway driving, (c) Bat-DC topology in urban driving, (d) Bat-DC topology in highway driving 60
Figure 3.12: Normalized battery capacity versus number of drive cycles with 100% SC initial and final SoC for (a) urban drive cycle and (b) highway drive cycle 62
Figure 3.13: System states and control trajectories with 100% SC initial and final SoC for (a) SC-DC topology in urban driving, (b) SC-DC topology in highway driving, (c) Bat-DC topology in urban driving, (d) Bat-DC topology in highway driving 63
Figure 3.14: Realistic daily commute drive cycle 64
Figure 3.15: Normalized battery capacity versus number of drive cycles 64
Figure 3.16: Normalized battery capacity fading with expanded battery pack in battery-only ESS (a) n_b=110, m_b=46 and (b) n_b=110, m_b=38 66
Figure 4.1: Two-stage onboard battery charger topology 69
Figure 4.2: Connection diagram of EV onboard charger 70
Figure 4.3: Connection diagram of EV onboard integrated charger with Bat-DC HESS topology 70

Figure 4.4: Battery normalized capacity versus number of drive cycles for (a) urban drive cycle, (b) highway drive cycle, and (c) hybrid drive cycle 72

List of Tables

Table 2-1: Parameter of SC equivalent circuit [43] 24
Table 3-1: Nissan Leaf and environment parameters 43
Table 3-2: Traction inverter power loss model parameters [26] 43
Table 3-3: IM per-phase equivalent circuit parameters [26] 43
Table 3-4: DC/DC converter conduction power loss model parameters 45
Table 3-5: DC/DC converter switching power loss model parameters [50] 45
Table 3-6: Battery cell APR26650 specifications 47
Table 3-7: SC cell BCAP350F specifications 47
Table 3-8: Possible dimensions of SC pack for SC-DC topology 54
Table 3-9: Possible dimensions of SC pack for Bat-DC topology 54
Table 3-10: Battery pack lifetime in terms of number drive cycles with 100% initial SC SoC 58
Table 3-11: Battery pack lifetime in terms of number drive cycle with 45% initial SC SoC 61
Table 3-12: Battery lifetime as a number of drive cycles 65
Table 4-1: Specifications of charging levels [62] 68
Table 4-2: Battery lifetime as a number of drive cycles 72
Table A-1: Parameters of battery cell equivalent circuit [40] 75

Acronyms

Bat-DC	HESS with battery connected to the DC bus and SC connected at the low voltage side
CCCV	Constant-current-constant-voltage
DoD	Depth of discharge of the battery
DP	Dynamic programming
EoL	End of life of the battery
ESS	Energy storage system
EV	Electric Vehicle
GHG	Green-house-gas
HESS	Hybrid energy storage system
IEC	Internal combustion engine
IM	Induction motor
PMSM	Permanent magnet synchronous machine
SAE	Society of Automotive Engineers
SC	Supercapacitor
SC-DC	HESS with SC connected to the DC bus and battery connected at the low voltage side
SoC	State of charge of the battery
SoH	State of health of the battery
SPDT	Single-pole-double-throw
VSC	Voltage source converter

Chapter 1
Introduction

1.1 Motivation

Traditional internal combustion engine (ICE)-based vehicles have served humanity for many years. However, as the global population and number of users have increased over the years, the consequences of the high utilization of ICE-based vehicles have become significant, and their environmental impact has become more prevalent. The main issues relevant to high ICE-based vehicles utilization are air pollution and sustainability of fuel resources. The term air pollution encompasses both greenhouse gas (GHG) emission that causes global warming and toxic pollutants emission that are harmful to humans' health. Typically, in most developed jurisdictions, the GHG emission by the transportation sector comprises about one-fourth to one-third of the total GHG emission [1], [2], [3], [4]. In particular, in Canada, GHG emission caused by the transportation sector is about 23% as of 2014, ranking it the second in the GHG emission by sector list [5]. The major GHG emitted by ICE-based vehicles is carbon dioxide (CO_2). Similarly, the major pollutants emitted by ICE-based vehicles are nitrogen oxides (NO_x), carbon monoxide (CO), volatile organic compounds (VOCs), and fine particulate matter ($PM_{2.5}$). All of these pollutants have a negative impact on human's health; most notably, some VOCs are cancer-causing agents [6]. Also, ground level ozone is created from a side reaction of NO_x with VOCs, which could cause inflammation of humans' airways [6].

Currently, the clean sources of energy are nuclear and renewable energy sources such as solar, wind, and hydro. The output of the current technologies for harvesting energy from these sources is in the form of electrical energy. Consequently, electrification of vehicles is required in order to power transportation vehicles by clean energy sources.

In regards to sustainability, the constant reliance on ICE-based vehicles will accelerate the exhaustion of the earth's finite reserve of fossil fuels. Consequently, it is paramount to utilize renewable energy sources to power the vehicles on the roads. This action also calls for vehicle electrification.

In most of the world, electricity generation capacity from renewable energy sources is lower than the electrical demand, excluding electric vehicle (EV) charging demands. Consequently, fossil fuel-based electricity generation plants will be used to supply energy to charge the EVs. This use could appear counter-effective in reducing vehicular transportation emissions, as the emissions are taking place at power generation plants instead. However, the emissions incurred at the power generation plants will be less than

those caused by the ICE-based vehicles for the same total energy consumption. This is due to the fact that the fuel-to-wheel efficiency of EVs is higher than that of ICE-based vehicles [4]. Depending on the mix of sources of electricity generation, the equivalent emission of EVs will vary. For example, in California, it was estimated that an EV and ICE-based vehicle in the same class would incur an annual CO_2 emission of about 2,500 and 12,000 lb, respectively [7]; whereas, in Kentucky, it was estimated that an EV would incur an annual CO_2 emission of about 9,000 lb, due to the high utilization of coal-based power generation in that state [7].

The battery pack is the energy source of EVs, and it comprises a significant portion of the vehicle cost and weight, with a major impact on performance. For example, the battery pack of Nissan Leaf comprises about 20% of both the vehicle's total cost and weight [8]. Also, if the power capability of the battery pack is low, it could become a bottleneck for the flow of power in the powertrain, which would deteriorate acceleration performance of the vehicle. Moreover, since the price of the battery pack is high, extending the battery pack lifetime is vital, especially, when battery packs usually experience premature capacity fading due to aggressive traction power demands [9], [10]. Figure 1.1 shows a traction electrical power demand profile at the DC bus of the traction inverter for urban driving. The traction power demand experiences a highly pulsating profile with negative power (implying regenerative braking). High power fluctuation and regenerative braking energy will increase the battery pack fading rate [9].

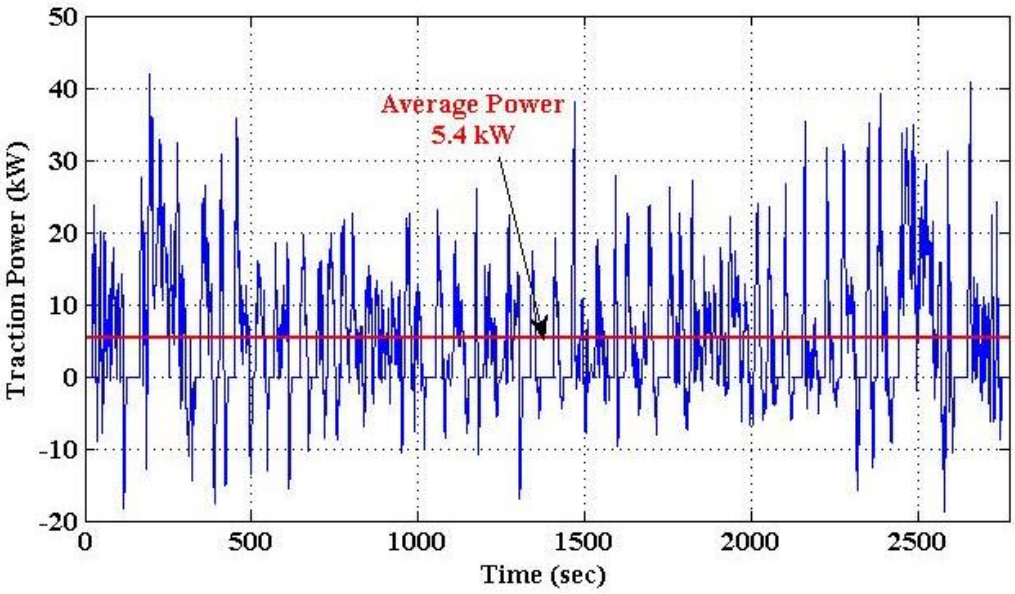


Figure 1.1: Traction power demand at the DC bus of the traction inverter

Consequently, hybridizing the battery pack with an auxiliary energy storage system that acts as a power buffer would help to reduce the battery capacity fading rate. The auxiliary ESS would supply and absorb the high-frequency component of the traction demand. Supercapacitor (SC) is the most promising electrical device to perform the power buffering function in EV applications, as it has a high power density and a simple system level integration [11], [12], [13]. Figure 1.2 shows the power and energy density map of batteries, SCs, and fuel cells. SCs could undergo a high number of cycles with low capacity loss. In fact, they could undergo more than 1 million cycles [14]. Fortunately, today, high voltage and power SC modules are commercially available from various manufacturers such as Maxwell Technologies and Saft.

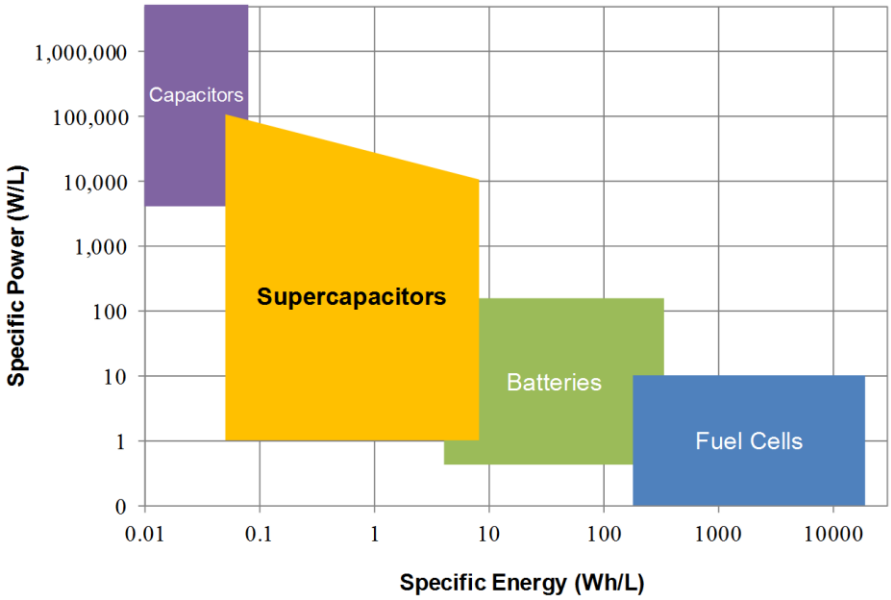


Figure 1.2: Specific energy and power map of various ESSs and fuel cell [15]

1.2 Literature Review

There are three main advantages that can be attained from using a hybrid energy storage system (HESS): 1) increase of powertrain efficiency, 2) increase of powertrain power capability, and 3) extension of battery lifetime. In regard to the first advantage, SCs supply power more efficiently than batteries, due to their lower internal impedances. In [16], under pulsed load conditions, it was illustrated how hybridizing the battery-only ESS with an SC through parallel connection would increase the system run time, compared to the battery-only ESS, due to the efficiency gain. However, the battery current could not be controlled, as the load current is passively split between the battery and SC according to their internal impedances. Consequently, the study in [16] was extended in [17], whereby a buck converter was used to connect the

battery to the SC that was connected across the load. Also, a low pass filter was added at the input of the buck converter to smooth out its pulsating input current. Under pulsed load conditions, the battery current was controlled to a relatively constant value. Although the battery current profile has been improved, the system run time has dropped compared to the battery-only ESS, implying a drop in efficiency. The reason is that the DC/DC converter losses had to be supplied by the battery. This result was also consistent with what was observed in [18] and [19]. Consequently, hybridization of the battery ESS for the purpose of increasing the system run time or powertrain efficiency is not practical.

The second advantage of HESS is to increase the power capability of the powertrain. It was demonstrated in [17] that the partially-decoupled HESS had a power capability seven times greater than the battery-only ESS for a prototype that consisted of two 18650 Li-ion battery cells and two 100 F SC cells. However, then the question is: "Is the power capability of commercial battery packs insufficient to meet the EV traction power demand?" An argument that is always raised in the literature is that the battery-only ESS needs to be oversized to meet the power requirement of the EV traction load. As a result, lowering the battery pack size and hybridizing the smaller battery pack with an SC allows for moderate sizing of the battery pack while achieving the required power capability as well as lowering the total cost. Unfortunately, this argument is not entirely true. Today's commercial lithium-ion battery packs have the power capability to meet the traction power demand in EV applications. The power capability of the battery pack increases as the number battery cells in the pack increases. Generally, in passenger EV applications, the traction energy requirement calls for a large battery pack comprising a high number of battery cells, which would indirectly meet the traction power requirement as well. Moreover, battery packs in PHEVs are relatively small; yet they are capable of supplying the total traction load that is equivalent to what is normally supplied by the large battery packs of EVs. This example illustrates how even smaller commercial battery packs are capable of meeting the traction power requirement. Further, range anxiety is another reason to increase the battery pack size. If an SC pack is to be added to the EV's ESS, the battery pack size must be reduced to accommodate the SC pack volume and cost. Therefore, using HESS to increase the power capability of passenger EV powertrains is not a reasonable endeavor.

The third advantage of HESS is to extend the battery lifetime. EV traction power demand exhibits rapid fluctuations with high power spikes, which would draw pulsating current from the battery. Pulsating current causes higher capacity loss to the battery compared to constant current, for the same total charge expenditure [9]. Consequently, using HESS with effective energy management, the battery pack lifetime could be extended by simply shifting the high-frequency component of the load current to the SC and

allowing the battery to supply the average load current. Therefore, pursuing HESS in EV applications to extend the battery lifetime is the most practical advantage among the three HESS advantages mentioned above.

Generally, the work in the literature of battery-supercapacitor HESS can be classified into two main research areas: 1) design of HESS topologies and 2) design of energy management algorithms. In the former area, this work addresses the selection of the number of DC/DC converters as well as DC/DC converter topologies through which the SC and battery are interfaced with the DC bus. In the latter area, this work covers the construction of energy management algorithms that dictate the load power split between the battery and SC packs. The focus of this thesis is on assessment of HESS topologies rather than the energy management algorithms. In the following, various HESS topologies will be reviewed.

1.2.1 HESS topologies

Figure 1.3 shows the basic HESS topologies through which the battery and SC are interfaced with the DC bus of the traction inverter. Each HESS topology inherently enjoys and suffers from certain advantages and drawbacks. The DC/DC converter in all HESS topologies is assumed to have bidirectional power capability. The passive topology in Figure 1.3(a) calls for no DC/DC converters, which facilitates system implementation and operation while avoiding the additional cost, weight, and energy losses incurred by the DC/DC converters. Also, the DC bus voltage will have small voltage variations as the battery is connected to DC bus. However, the battery will passively supply a portion of the traction power demand spikes, which would degrade the battery capacity. The traction power demand split between the battery and SC is governed by their internal impedances. Also, the SC energy capacity is not effectively utilized as its voltage magnitude excursions are limited by the battery.

In [16], a thorough analytical study of the passive HESS topology was presented to illustrate the gain in power capability, efficiency, and run time of the passive HESS compared to battery-only ESS under pulsed load conditions. For a system consisting of a 1.35 Ah, 7.2 V lithium-ion battery pack and a 23 F SC pack, the system power capability increased five times, and the power loss decreased by 74% compared to the battery-only ESS. However, no quantification of battery capacity fading was analyzed or pursued.

Next, the partially-decoupled HESS topology in Figure 1.3 (b) calls for a single DC/DC converter. This HESS topology will be abbreviated as SC-DC, as the SC is connected to the DC bus through the DC/DC converter. In this HESS topology, the DC bus will have small voltage fluctuations, as the battery is connected to the DC bus. Also, the SC energy capacity can be fully utilized, since it can be discharged to,

theoretically, zero volts. But, normally the SC voltage excursion is limited to about 50 to 70% from SC rated maximum voltage to avoid operating the DC/DC converter in the low-efficiency region. The DC/DC converter power rating must be sufficiently high to match the traction power demand spikes, as the SC is responsible for supplying them. Consequently, the DC/DC converter will call for bulkier, heavily, and expensive inductor, heat sink, and IGBT module to handle the demand power spikes. Also, to prevent the battery from passively supplying the demand power spikes, the DC/DC converter must regulate the processed power quickly, which is deemed a challenging task and increases implementation complexity. The SC-DC topology is the most commonly adopted HESS topology by researchers, the reasoning being based on the high SC capacity utilization and small DC bus voltage fluctuation [12], [13], [20], [21], [22]. In fact, the first scientific paper on the topic of battery-SC HESS for EVs adopted the SC-DC topology [23].

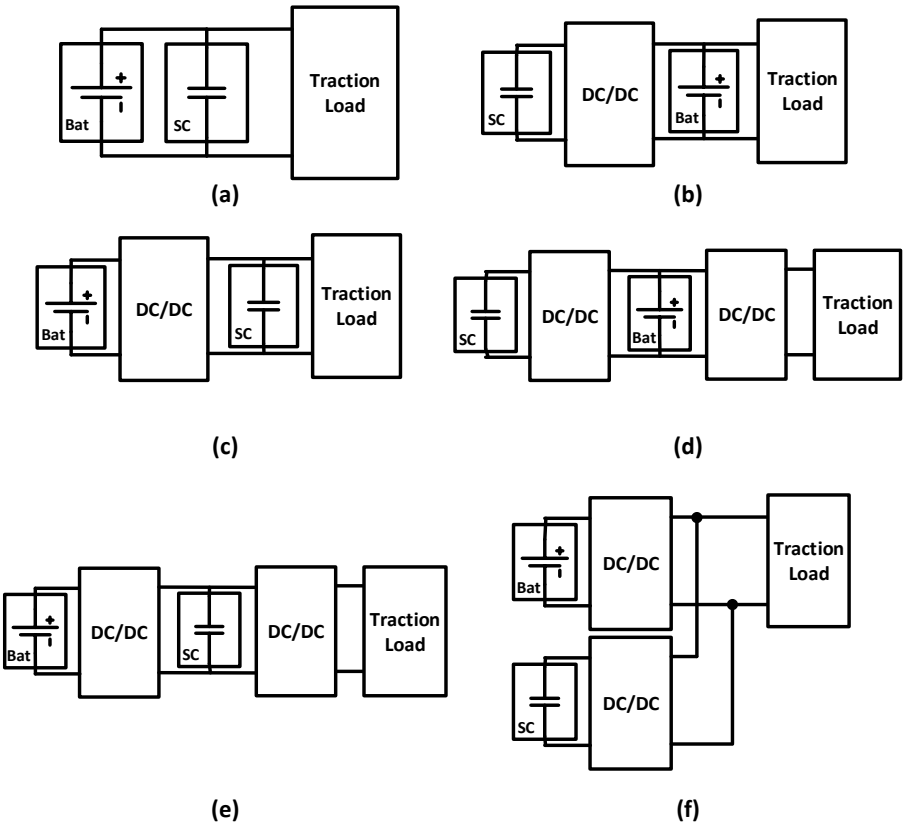


Figure 1.3: Battery-Supercapacitor Hybrid Energy Storage System Topologies: (a) passive, (b) partially-decoupled with battery DC bus connection, (c) partially-decoupled with SC DC bus connection, (d) cascaded fully-decoupled with SC connected downstream, (e) cascaded fully-decoupled with battery connected downstream, and (f) fully-decoupled

On the other hand, the second partially-decoupled HESS topology, shown in Figure 1.3 (c), interchanges the positions of the battery and SC compared to SC-DC topology. Consequently, DC bus voltage could experience high fluctuations, as the SC supplies and absorbs the demand power spikes and regenerative braking power at the DC bus. Also, the SC capacity utilization is low due to the limited allowable SC voltage excursions. The minimum SC voltage must respect the minimum input voltage range of the traction inverter.

Unlike the SC-DC topology, the battery output power and current is accurately controlled via the DC/DC converter. The rating of the DC/DC converter would rationally be expected to be low because the battery output power is controlled to be relatively equal to the average of the traction power demand, which tends to be an order of magnitude lower than the peak power demand in urban drive cycles. However, in some situations, when the SC voltage drops below the lower limit of the traction inverter input voltage range, the full traction power must be supplied by the battery through the DC/DC converter to sustain the SC and DC bus voltage. Accordingly, the rating of the DC/DC converter must also be as high as the traction power demand, which is the same as in the SC-DC topology.

However, in [10], [24], the partially-decoupled HESS topology of Figure 1.3 (c) was modified to allow for a low rating DC/DC converter. A bypass diode was used to bypass the DC/DC converter when the voltage level of the SC is lower than or equal to that of the battery. Figure 1.4 shows the modified HESS topology, where the DC/DC converter assumes the common half-bridge topology. Further, in [25], a HESS topology similar to the one in Figure 1.4 is proposed, but with the DC/DC converter allowing only unidirectional power flow from the DC bus to the battery. The battery supplies power to the load only through the bypass diode. The converter draws power from the DC bus and feeds the battery only when the DC bus voltage exceeds its rated limit. For these HESS topologies with the bypass diode, it was implicitly assumed that the input voltage range of the traction inverter includes the SC maximum voltage and battery nominal voltage plus some tolerance to account for the voltage drops in the internal impedances and the gradual reduction in the battery SoC-dependent voltage source. The partially-decoupled HESS topology shown in Figure 1.3 (c) will be abbreviated as Bat-DC.

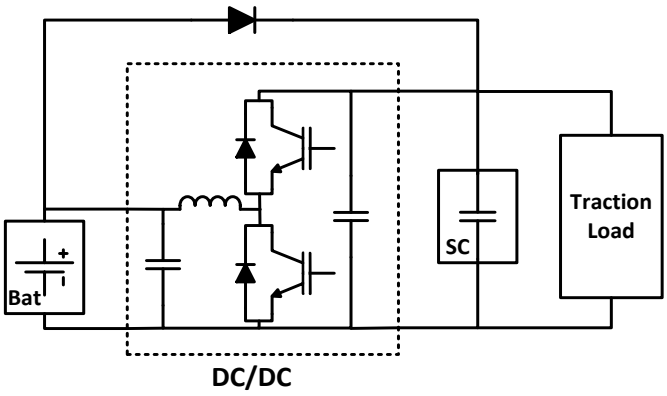


Figure 1.4: Proposed partially-decoupled HESS topology in [10], [24]

The cascaded HESS topologies shown in Figure 1.3 (d) and (e) call for two DC/DC converters. The losses in these topologies are relatively high, since there are two converters in these topologies. Also, the rating of the upstream DC/DC converter must match the full traction power demand, as it processes the full load power. Moreover, for the topology in Figure 1.3 (e), the second DC/DC converter rating must match the full traction demand because, in certain situations, the battery needs to supply the full traction load to sustain the DC bus voltage. The DC bus voltage in these two topologies can be solidly regulated via the upstream DC/DC converter.

The fully-decoupled HESS topology in Figure 1.3 (f) calls for two DC/DC converters connecting the battery and SC to the DC bus in parallel. Similar to the cascaded topologies, the DC bus voltage can be solidly regulated. Also, the output power and current of both battery and SC can be accurately controlled. The SC DC/DC converter must match the full traction power load, as it is responsible for supplying demand power spikes. Similarly, the battery DC/DC converter must also match the full traction power demand. This is necessary because in situations when the SC is depleted, the battery would have to supply the full traction load. The rating of the battery DC/DC converter can be lowered using the same idea mentioned for Bat-DC topology. A bypass diode can be used to bypass the DC/DC converter and clamp the battery to the DC bus when the DC bus voltage level drops to that of the battery.

Partially-decoupled HESS topologies are the most promising candidates for EV application [10], [21], [24], [26], [27]. They can support any energy management algorithm that the cascaded and fully-decoupled topologies support. Also, they call only for a single DC/DC converter. Further, they can regulate the battery current, unlike the passive topology. Consequently, the partially-decoupled topologies will be considered in this thesis.

Based on the aforementioned qualitative analysis of the two partially-decoupled HESS topologies, it is still unclear which topology is superior. Consequently, a thorough quantitative analysis is deemed necessary, whereby analytical simulation are performed to quantify the performance index. This performance index could be battery capacity fading or system power losses.

Reference [18] presented a quantitative analysis of four HESS topologies, passive, partially-decoupled Bat-DC and SC-DC, and fully-decoupled. The quantitative analysis was conducted via simulations, whereby the HESS was used to drive a bus through a city drive cycle. The energy management and dimensioning of the battery and SC packs for all topologies were determined via dynamic programming (DP). This allowed for a meaningful and unbiased comparison between all HESS topologies, as DP optimization technique finds the global optimal solution for the energy management as well as battery and SC packs' dimensions for the chosen drive cycle and HESS topology. The dimension of a pack refers to the number of series cells in a string and number of parallel strings. The objective of the DP optimization was to maximize the battery SoC at the end of the drive cycle, which implies maximizing the driving range. The results of the battery end of drive cycle SoC in descending order are as follows, 41.13, 40.49, 39.09, 35.58, and 30.10% for passive HESS, battery-only ESS, SC-DC HESS, Bat-DC HESS, fully-decoupled HESS, respectively. The active HESS topologies perform worse than the battery-only ESS, due to the losses incurred in the DC/DC converters. However, the passive HESS performs better than the battery-only ESS. The reason is that the SC could supply power bursts more efficiently compared to the battery. Also, there is no DC/DC converter in the passive HESS, thus conserving more energy compared to the active HESS topologies. However, in passive HESS and battery-only ESS, the battery is exposed to high power bursts and negative power, which could shorten the battery lifetime. Battery capacity fading was not pursued in this work. Also, the adopted topology of the DC/DC converter was not presented. Further, in SC-DC topology, the voltage level of both sides of the DC/DC converter could vary and be higher or lower than one another over the drive cycle. Therefore, the common half-bridge converter could not be used.

In [28], a comparative study of four partially-decoupled HESS topologies were conducted. The topologies were, SC-DC, Bat-DC with and without bypass diode, and Bat-DC with bypass diode and unidirectional DC/DC converter (direction of power is from DC bus to the battery). Drive cycle simulation was performed, and battery capacity fading was computed based on a Li-ion battery capacity fading model presented in [25]. Also, an incremental cost analysis was used to size the SC pack. The capacity fading results of all topologies were close to one another. However, no clear description of the converter topology was presented.

1.3 Objectives

It has been proven that battery-supercapacitor HESS outperforms battery-only ESS in both vehicular propulsion performance and extending battery lifetime. However, there is more than one HESS topology to choose from. Also, qualitative analysis is not sufficient to draw a solid conclusion about the superiority of one topology over another. Thus, quantitative analysis is deemed necessary to assess the HESS topologies performances. Further, an accurate economic feasibility analysis of the HESS requires quantification of the battery lifetime extension. Consequently, the objectives of this research are to:

- Compare SC-DC HESS, Bat-DC HESS, and battery-only ESS by conducting analytical simulations to quantify the battery lifetime.
- Construct an onboard integrated charger scheme that utilizes the existing powertrain traction inverter and HESS DC/DC converter to realize a two-stage charger topology.

1.4 Thesis Outline

In Chapter 2, all the background and theory used to conduct the research are presented and discussed. First, the adopted electrical, thermal, and capacity fading models of the battery and the electrical model of the SC are presented. Next, the models of the powertrain components are discussed. Then, dynamic programming, a mathematical optimization technique for solving optimal control problem of dynamical systems, is described.

The complete simulation platform is presented in Chapter 3, followed by the simulation results and analysis. The effect of the drive cycle type on the battery pack capacity fading is discussed. The battery capacity fading is tested for both highway and urban drive cycles. Then, a conclusion on the superiority of the HESS topology is drawn based on the quantitative analysis.

In Chapter 4, the onboard integrated charger scheme is introduced, which lowers the cost of HESS. Finally, in Chapter 5, a summary of the research findings is presented, followed by a recap of the contributions and future work.

Chapter 2
Background

All the necessary background and knowledge used in the proceeding work is presented in this chapter. First, the adopted battery electrical, thermal, and capacity fading models will be presented, followed by the adopted electrical model of the SC. Next, the simulation model of EV traction powertrain will be discussed. Finally, the dynamic programming optimization technique will be illustrated.

2.1 Battery

Five commercially developed battery types, NiCad, NiMH, ZEBRA, lead-acid, and Li-ion, were reviewed in [29]. The specific power and specific energy in W/kg and Wh/kg, respectively, of all battery types are illustrated by the Ragone plot in Figure 2.1 [30]. Each battery type proposes a different degree of suitability for vehicular propulsion applications in plugin-hybrid electric, hybrid electric, and electric vehicles.

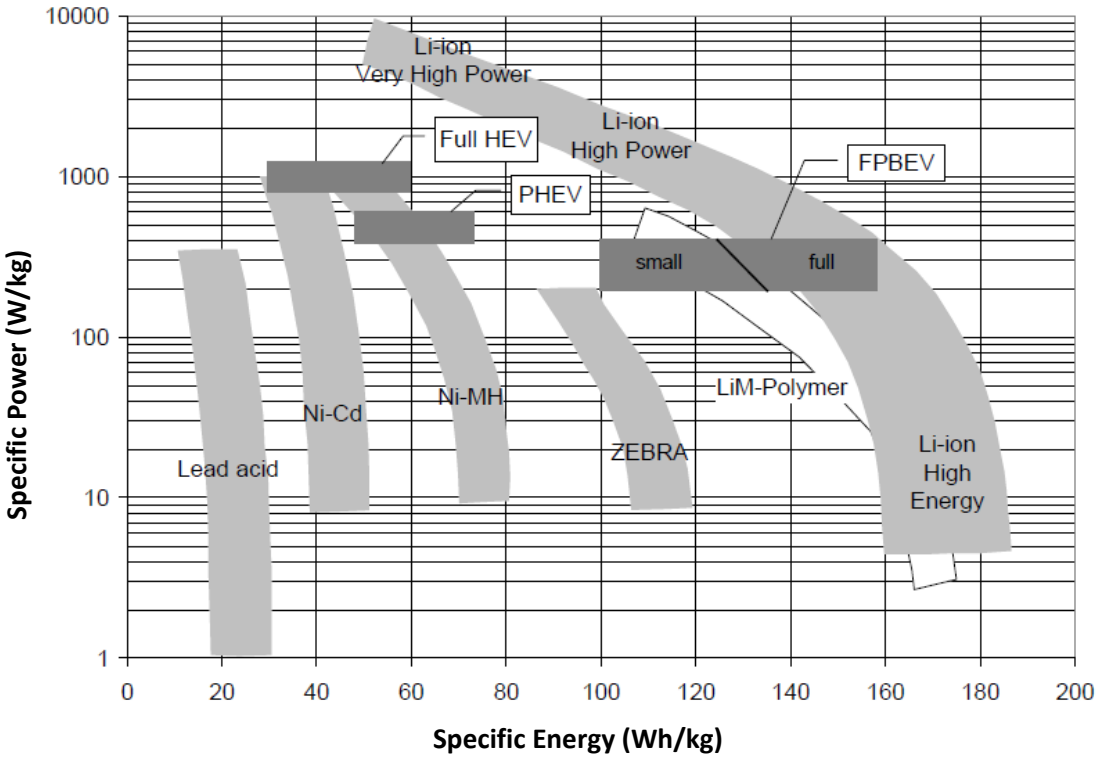


Figure 2.1: Ragone plot: specific energy and specific power of various batteries [30]

Due to safety and environmental constraints, NiCad and ZEBRA can be eliminated from the list of candidate batteries for EV application. Cadmium is a highly environmentally polluting element [9]. Also, NiCad batteries have low power and energy densities. ZEBRA battery, on the other hand, nominally operates at high temperatures, in the range of 270-350 °C [30]. It uses its own energy to maintain its high temperature, which reduces efficiency significantly. More importantly, such high operating temperature in EV applications is very hazardous.

The lead-acid battery is the most mature battery technology in the industry. It is available for high volume production today for a relatively low cost [29]. In fact, lead-acid battery packs were used in the first EV, which gave a driving range of 100 km [31]. However, lead-acid batteries experience few operation drawbacks that significantly hinders their candidacy for EV application today. Their energy density is low, calling for a high number of battery cells, which will occupy more space and increase the EV weight and cost. It has a limited SoC operating range, which limits its degree of utilization. Also, it has a relatively low cycle life [9], [29].

According to the Ragone plot, shown in Figure 2.1, the NiMH battery has relatively moderate specific energy and power densities. In HEV applications, the battery pack power capability is more of interest rather than the energy capability, as the battery is used as a power buffer. Therefore, batteries with moderately low energy and high power capacities, such as NiMH, are sufficient for HEV propulsion. Some HEVs, such as Toyota Prius, use NiMH battery instead of the more popular Li-ion battery, mainly due to its low cost per Watt ($/W). However, for EV applications, energy capacity is vital; thus, NiMH battery packs cannot be used, as a high number of NiMH battery cells will be required, thereby increasing the vehicle's weight, occupied space by ESS, as well as the cost. Also, similar to the lead-acid battery, the NiMH battery has a limited SoC range of operation [29].

The Li-ion battery enjoys the highest energy and power densities, as well as the highest cycle-life among all five battery types [32]. All EVs on the Canadian market today adopt the Li-ion battery as an ESS [33]. Other advantages of the Li-ion battery are recyclability, low self-discharge, high coulomb efficiency, and high reliability at high-temperature operation [32]. Further, the Li-ion battery voltage, depending on the particular Li-ion battery type, is in the range of 3.3-3.7 V, which is higher than that of all of the other battery types mentioned above. This high voltage range allows for a lower number of series cells to realize a high pack voltage; thus, lowering the balancing circuit requirements.

Further, there are five main Li-ion battery types, each with its own cons and pros. These are lithium manganese oxide ($LiMn_2O_4$), lithium nickel manganese oxide ($LiNiMnCoO_2$ or NMC), lithium iron

phosphate ($LiFePO_4$), lithium nickel cobalt aluminum oxide ($LiNiCoAlO_2$), and lithium titanate ($Li_4Ti_5O_{12}$). A comparative study on these Li-ion battery types was conducted in [32], [34]. Six metrics were used to compare these battery types, specific energy, specific power, safety, performance, lifespan, and cost. Figure 2.2 shows the comparison results on a radar plot [34].

The $LiFePO_4$ battery enjoys the most moderate balance among the comparison metrics. Also, most researchers share the same belief that $LiFePO_4$ battery is the most promising Li-ion battery type for future EVs [9], [25], [35], [36]. Consequently, $LiFePO_4$ battery will be adopted in this work.

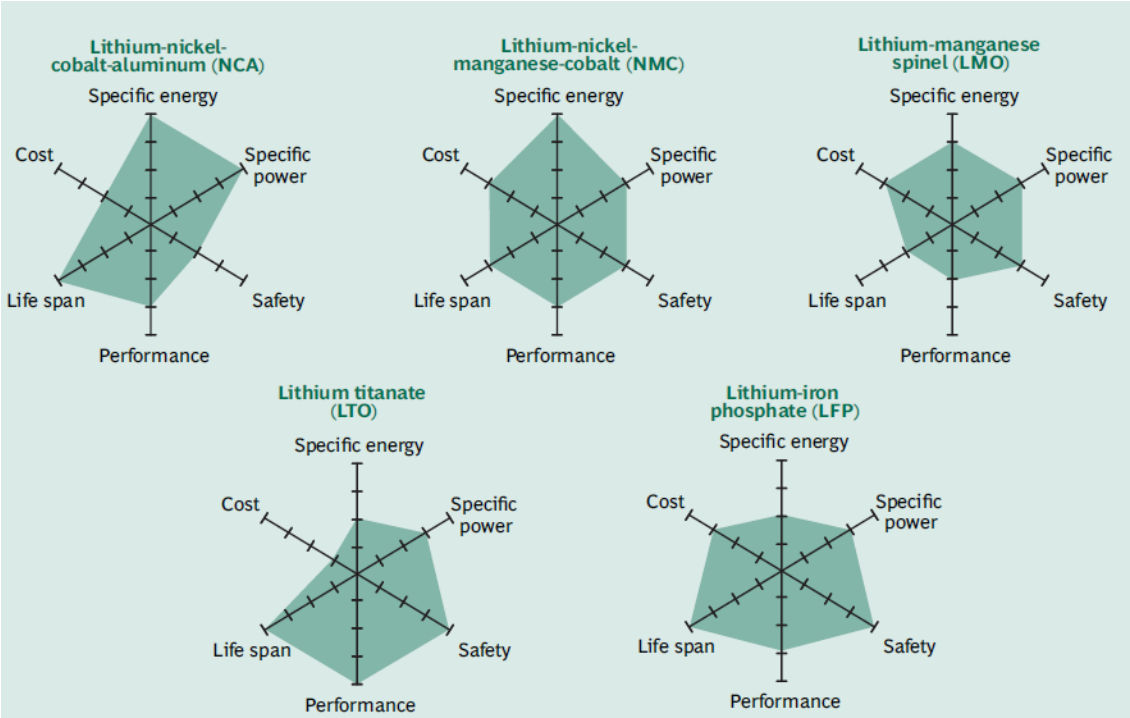


Figure 2.2: Performance comparison of Li-ion batteries [34]

2.1.1 Definitions

In the literature, different naming conventions and terminologies are used to describe the battery characteristics and operational states. This sub-section will clearly state and define the battery terminologies adopted in this work. They are similar to what have been adopted in [9].

i. Cutoff voltage (V_{off})

When the battery cell terminal voltage reaches the cutoff voltage, the battery operational capacity is said to be depleted. The value of V_{off} may vary for different manufacturers with a range of 2.0-2.5 V. However, most manufacturers recommend 2.5 V as the cutoff voltage [9], [32].

ii. Operational capacity (PC_{Ah})

Normally, the battery cell capacity is reported in terms of the charge that can be delivered by the battery. The conventional charge unit used in the battery literature is Ampere-hour (Ah) rather than coulomb (C). Battery manufacturers will provide the battery operational capacity for different discharge currents. For example, Figure 2.3 shows the APR18650 battery cell voltage and stored charge characteristics for different discharge currents [37]. For higher discharge current, the battery reaches V_{off} with a lower total charge expenditure. As shown in Figure 2.3, in ascending order, the total discharged Ah corresponds to that of 20, 10, and 5 A discharge currents. This is mainly due to the fact that the voltage drop across the internal impedance is higher for higher discharge currents. Thus, at high discharge current, the battery voltage would reach V_{off} even though it has some charge that could be extracted with lower discharge current. Consequently, PC_{cap} is defined as the Ah charge that can be extracted from the battery cell at a particular discharge current.

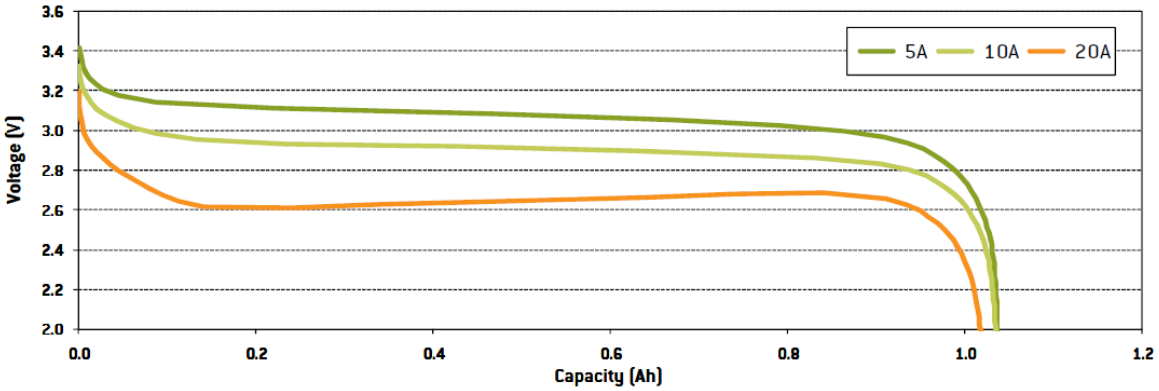


Figure 2.3: Discharge characteristics at room temperature of the battery cell APR18650 manufactured by A123 Systems [37]

iii. True capacity (C_{Ah})

C_{Ah} is defined as the battery Ah that can be extracted when the discharge current is set to a sufficiently low value so that the voltage drop across the internal impedance is essentially zero. For example, the

APR18650 battery cell is reported to have a charge capacity of 1.1 Ah, which is higher than what is observed in Figure 2.3 for all three discharge currents.

iv. Capacity loss (ξ)

ξ is the Ah capacity loss from the battery C_{Ah} that will not be accessible in the future.

v. State of health (SoH)

The battery end of life (EoL) is said to be reached, if at reference temperature condition, the battery energy or power capacity is degraded to a level that prevents the battery from meeting the load power and energy requirements. Also, another guideline in EV applications is used to determine EoL is when the battery C_{Ah} is degraded to 80% of its rated value, even though the battery is still capable of meeting the load power and energy requirements [9], [38].

SoH is a subjective term. By definition, SoH is a figure that is one or 100% for a brand new battery and zero or 0% when the battery reaches EoL. If the second EoL guideline presented above is adopted, SoH would be 0% when the battery C_{Ah} is degraded to 80% of its rated value. Further, SoH will linearly span the battery C_{Ah} from 100 to 80% of its rated value. This can be mathematically represented as follows:

$$SoH = \left(1 - \frac{\xi}{0.2 \times C_{Ah}}\right) \times 100\% \qquad (2\text{-}1)$$

For example, if the capacity of a 2.3 Ah battery cell has degraded to 2 Ah, the battery cell SoH would be 35%.

vi. State of charge (SoC)

SoC is defined as the ratio of Ah remaining in the battery to the C_{Ah} of the battery.

vii. Depth of discharge (DoD)

DoD is defined as the ratio of the total Ah extracted from the battery to the C_{Ah} of the battery.

viii. C-rate

C-rate is a dimensionless figure that represents the ratio of the discharge current to the true capacity of the battery. For example, a 2 Ah battery discharged with 3 A current is said to be discharged at 1.5 C-rate.

2.1.2 Battery electrical model

The battery is a complex electrochemical system. Electrochemical models are not suited for electrical system simulation, as they are meant for design optimization of the battery physical system. Consequently, electrical equivalent circuit-based models were developed in the literature. They can be easily integrated in electrical system design and computer simulation. The terminal I-V characteristics of the equivalent circuit model must coincide with that of the actual battery. Most researchers have agreed that the simple equivalent circuit in Figure 2.4 could capture the battery terminal I-V characteristics with great details [39], [36], [40].

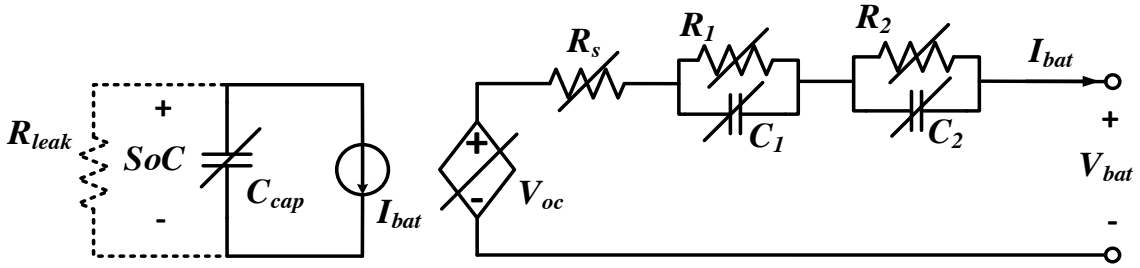


Figure 2.4: Battery cell electrical equivalent circuit model

The sub-circuit on right governs the terminal I-V characteristics. The resistor R_s models the instantaneous terminal voltage drop due to the ohmic resistance, whereas the R-C networks model the terminal voltage dynamics due to the Li-ion diffusion in the electrolyte and solid phase [40]. The values of the passive components in the right-hand-side sub-circuit are functions of SoC, temperature, and direction of the current. However, the controlled voltage source V_{OC} is only a function of SoC. On the other hand, the sub-circuit on the left governs the charge conservation of the battery. The voltage across the capacitor C_{cap} swings between 0 and 1 V and represents the battery SoC. The charge stored in C_{cap} represents the battery charge ($C_{cap} \times SoC$). The resistance R_{leak} models the battery self-discharge, which is usually omitted for Li-ion batteries due to their low self-discharge characteristics [9], [36], [39].

Current pulse relaxation technique is used to parametrize the battery equivalent circuit components [36], [39], [40]. First, the battery would be charged to 100% SoC via constant-current-constant-voltage (CCCV) charging protocol. Then, the battery is cycled with a pulsating current, as shown in Figure 2.5. After a current pulse, the battery is rested, during which the battery voltage will rise exhibiting a transient response that has two characteristic components. The first component is the instantaneous voltage rise due to the ohmic resistance. The second component is an exponential rise transient response associated with Li-ion diffusion. The values of the passive components in the battery are parametrized by curve fitting the transient

response of the equivalent circuit terminal voltage with that of the actual battery. Passive components parametrization is done for every current pulse during the current pulse relaxation experiment to observe the effect of SoC. Further, to observe the effect of temperature and direction of the current, the above process can be repeated for different temperatures and with charging pulsating current.

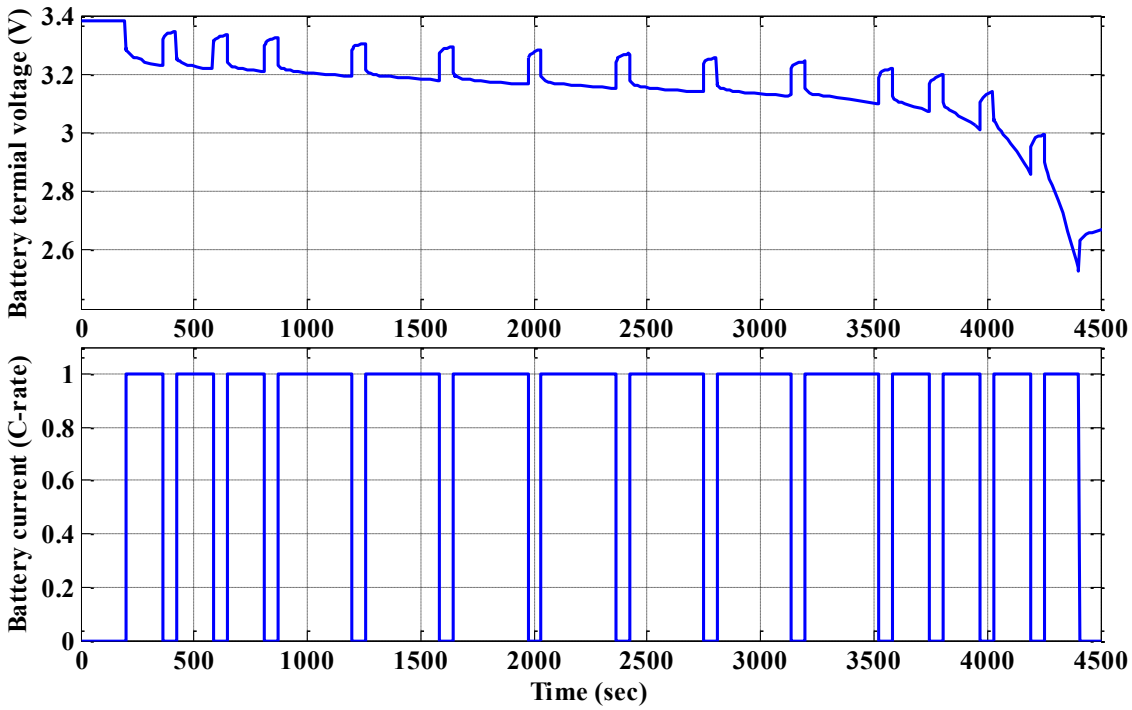


Figure 2.5: Pulse current relaxation technique for battery parameters characterization

The cylindrical battery cell ANR26650 manufactured by A123 Systems is adopted in this work. Its both electrical equivalent circuit and thermal models have been reported in [40], [41]. The governing equations of the passive components and SoC-dependent voltage source are as follows:

$$R_s = R_{s_{0*}} e^{\left(\frac{T_{refR_{s*}}}{T_m - T_{shiftR_{s*}}}\right)} \tag{2-2}$$

$$R_{1_*} = \left(R_{10_*} + R_{11_*}SoC + R_{12_*}SoC^2\right) e^{\left(\frac{T_{refR_{1*}}}{T_m - T_{shiftR_{1*}}}\right)} \tag{2-3}$$

$$C_{1_*} = C_{10_*} + C_{11_*}SoC + C_{12_*}SoC^2 + \left(C_{13_*} + C_{14_*}SoC + C_{15_*}SoC^2\right)T_m \tag{2-4}$$

$$R_{2_*} = \left(R_{20_*} + R_{21_*}SoC + R_{22_*}SoC^2\right)e^{\left(\frac{T_{refR_{2*}}}{T_m}\right)} \tag{2-5}$$

$$C_{2_*} = C_{20_*} + C_{21_*}SoC + C_{22_*}SoC^2 + \left(C_{23_*} + C_{24_*}SoC + C_{25_*}SoC^2\right)T_m \tag{2-6}$$

$$V_{oc} = a_1 e^{-a_2 SoC} + a_3 + a_4 SoC + a_5 e^{-\frac{a_6}{1-SoC}} \tag{2-7}$$

where the subscript "*" is replaced with "d" or "c" for charging and discharging, respectively, and T_m is the average of the battery cell core and surface temperatures in degrees Celsius. The constants in equations (2-2) to (2-7) are reported in Table A-1 in Appendix A.

The capacitor C_{cap} must be sized such that it can hold the battery rated true capacity when its voltage is 1 V, which corresponds to 100% battery SoC. The value of C_{cap} can be calculated by (2-8).

$$C_{cap} = 3600 C_{Ah} \tag{2-8}$$

It is worth mentioning that according to [9] and [35], C_{cap} is susceptible to temperature. The battery would experience a temporary capacity C_{Ah} rise at higher temperatures. Also, the passive components are susceptible to C-rate. However, the variation in C_{cap} and other passive components due to temperature and C-rate are minor. Consequently, these effects will not be considered.

The battery pack is constructed from multiple battery cells connected in series, and battery strings connected in parallel. n_b and m_b denote the number of series battery cells in a string and parallel battery strings in this pack, respectively. The battery pack can be modeled by an equivalent circuit that is identical to that of the single battery cell, except for the values of the passive components and controlled voltage source, which are scaled by n_b and m_b. The expressions for the parameters in the battery pack equivalent circuit are as follows:

$$V_{oc}' = n_b V_{oc} \tag{2-9}$$

$$R_s' = \frac{n_b}{m_b} R_s \tag{2-10}$$

$$R_1' = \frac{n_b}{m_b} R_1 \tag{2-11}$$

$$R_2' = \frac{n_b}{m_b} R_2 \tag{2-12}$$

$$C_1' = \frac{m_b}{n_b} C_1 \tag{2-13}$$

$$C_2' = \frac{m_b}{n_b} C_2 \tag{2-14}$$

$$C_{cap}' = m_b C_{cap} \tag{2-15}$$

In (2-9) to (2-15), the superscript "′" denotes the parameters of the battery pack equivalent circuit.

2.1.3 Battery thermal model

In [40], [41], a lumped thermal model of the cylindrical battery cell ANR26650 was constructed via laboratory experiments. The model captures the dynamics of the battery core and surface temperatures. In the lumped thermal model, dissipated heat Q is assumed to be generated at the core of the battery cell. Further, the dissipated heat is transferred from the code to surface of the battery by conduction through the battery's material thermal resistance R_c. Similarly, the heat is transferred from the battery surface to the cooling medium through thermal convection resistance R_u. Figure 2.6 shows the lumped thermal model diagram of the battery [41].

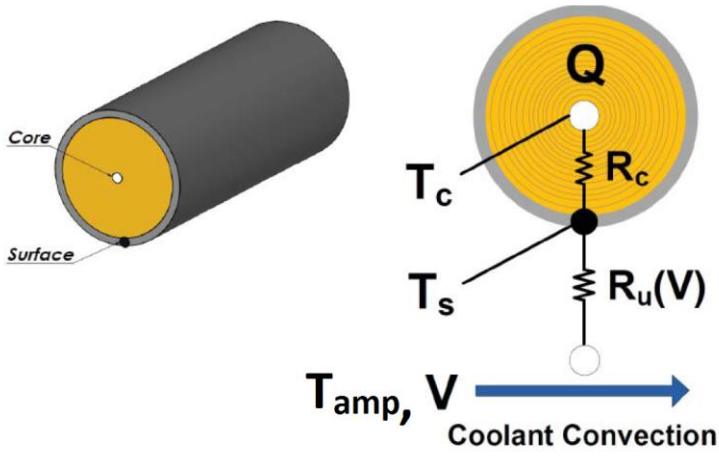


Figure 2.6: Cylindrical battery lumped thermal model [41]

The heat generated Q is computed from the battery electrical equivalent circuit model by multiplying the battery cell current by the voltage drop across the internal impedance:

$$Q = (V_{oc} - V_{bat}) I_{bat} \tag{2-16}$$

The dynamics of the battery thermal model can be equivalently modeled by the equivalent electrical circuit in Figure 2.7. The capacitances C_C and C_s represent the effective thermal capacities of the battery core and surface, respectively. The voltages T_C, T_s, and T_{amp} represent the battery core, battery surface, and cooling medium temperatures, respectively.

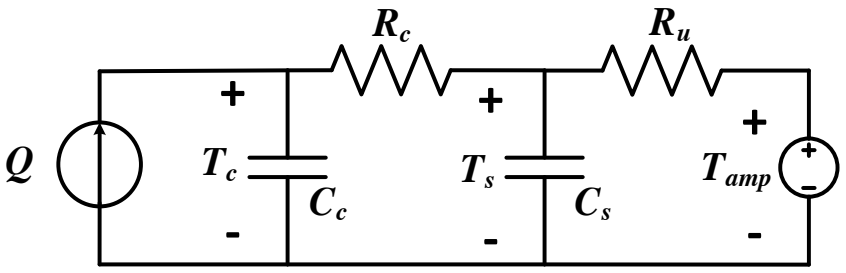


Figure 2.7: Electrical equivalent circuit of battery cell thermal model

It is implicitly assumed that all battery cells in the pack have the same temperature, as the battery cooling system would uniformly cool all battery cells. Consequently, it is only required to model the temperature of a single battery cell. The heat generated Q in the battery cell can be calculated in terms of the battery pack quantities by simply scaling down the power losses in the battery pack internal impedance by n_b and m_b, as described by (2-17).

$$Q = \frac{(V_{oc}{}' - V_{bat}{}')I_{bat}{}'}{n_b m_b} \tag{2-17}$$

2.1.4 Battery capacity fading model

Battery manufacturers provide Ah capacity fading information on datasheets of their commercial products. For example, Figure 2.8 shows the normalized battery capacity as a function of number of cycles for different operating temperatures and discharge C-rates [42]. In these experimental tests done by manufacturers, typically, the battery would be charged to 100% SoC via CCCV charging protocol. Then, the battery is discharged with a constant current with a particular C-rate at a particular temperature for different DoD levels [9]. However, this cycling scheme does not resemble the battery discharge current profile in EV applications, for which the battery is subjected to pulsating current profile that might have charging intervals [9]. Also, batteries in EVs do not normally get discharged by the same DoD in every cycle. Therefore, it is not clear how one could quantify the battery capacity fading in EV applications using the typical data presented in manufacturers' datasheets. Consequently, researchers have tried to construct battery capacity fading models that could capture the effect of various stress factors and conditions that are

commonly present in EV traction power demand, such as discharge current waveforms, intermittent charging currents, and initial operating SoC.

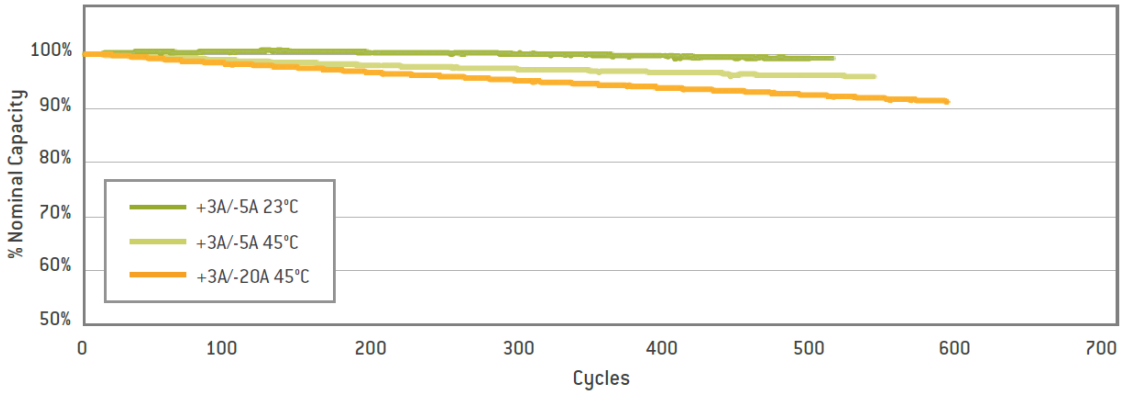


Figure 2.8: Cycle life performance at 100% DoD for different operating temperatures and discharge C-rates of the battery cell ANR26650 manufactured by A123 Systems [42]

In [9], [35], a capacity fading model for $LiFePO_4$ batteries was proposed in which the battery capacity loss is measured versus Ah processed instead operating cycles. The battery Ah processed is defined by (2-18).

$$Ah_{proc} = \frac{1}{3600}\int |ibat(t)|dt \qquad (2\text{-}18)$$

Four stress factors were identified, i.e., DoD and initial SoC, discharge C-rate, temperature, and regenerative braking C-rate. To parameterize the fading model, the battery cell was exposed to a single stress factor at a time. The battery cycling current had a waveform shown in Figure 2.9.

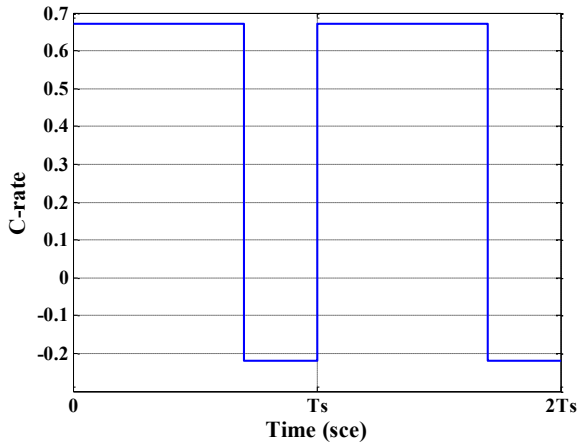


Figure 2.9: Discharge cycle current waveform

To test the effect of DoD and initial SoC, different battery cells were discharged with different DoDs and initial SoCs. However, no consistent relationship was found between the battery capacity fading and DoD and initial SoC. Instead, the average and normalized standard deviation of SoC were adopted as a stress factor, as they had a consistent relationship with the battery capacity fading. The average and normalized standard deviation of SoC will be abbreviated as SoC_{avg} and SoC_{dev}, respectively. Similarly, to test the effect of temperature, different batteries were cycled at different temperatures. A clear relationship was found, and the model was parameterized. Next, to test the effect of the discharge C-rate, two batteries were discharged with the current profile of Figure 2.9. But, the value of the positive current pulse was set to 1 C-rate for one of the batteries and 1.82 C-rate for the other. The capacity fading results of the two batteries were the same, which implies that the capacity fading was unaffected by discharge C-rate. However, in manufacturers' datasheets, the battery capacity fades faster for higher discharge C-rate, as shown in Figure 2.8. The authors in [9], [35] attribute the increase in battery capacity fading rate to the increase in the battery temperature, due to the high discharge C-rate, rather than the magnitude of the current itself. Next, to test the regenerative braking C-rate, different batteries were cycled with different current profiles at the same reference temperature. Three battery cells were cycled. The first battery was cycled with constant current, second with pulsating current with a resting period, and third with the original current profile in Figure 2.9. It was found that the battery cells cycled with the constant current and current profile in Figure 2.9 faded at the same rate as a function of Ah_{proc}. However, the battery cycled with the current profile with resting period faded faster compared to the other batteries. A second experiment was conducted in which different battery cells were cycled with the original current profile in Figure 2.9 but with different re-charge C-rate. It was found that at low temperatures, in the range of 0 °C, higher re-change C-rate increases battery fading rate. However, not enough data were obtained to deduce a relationship and parametrize the fading model. Therefore, it was concluded that the C-rate magnitude of regenerative braking charging current has no effect on battery capacity fading rate. Consequently, the final fading model was mathematically formulated as follows [9], [35]:

$$\xi\left(T, SoC_{avg}, SoC_{dev}, Ah\right) = \sum_{i}\left(\left(k_{s1}SoC_{dev,i}\cdot e^{\left(k_{s2}\cdot SoC_{avg,i}\right)} + k_{s3}e^{\left(k_{s4}\cdot SoC_{dev,i}\right)}\right)\cdot e^{\left(-\frac{E_a}{R}\left(\frac{1}{T_i}-\frac{1}{T_{ref}}\right)\right)}\right)\cdot Ah_i \tag{2-19}$$

$$SoC_{avg} = \frac{1}{\Delta Ah_m}\int_{Ah_{m-1}}^{Ah_m} SoC(Ah)dAh \tag{2-20}$$

$$SoC_{dev} = \sqrt{\frac{3}{\Delta Ah_m}\int_{Ah_{m-1}}^{Ah_m} \left(SoC(Ah) - SoC_{avg}\right)^2 dAh} \tag{2-21}$$

where, T is battery temperature in K, E_a activation energy (78060 mol/J), R ideal gas constant (8.314 J/mol·K), T_{ref} reference temperature (298 K), k_{s1} constant (-4.092×10^{-4}), k_{s2} constant (-2.167), k_{s3} constant (1.408×10^{-5}), and k_{s4} constant (6.130). The summation in (2-19) is indexed when the temperature data points are changed. Also, it is worth mentioning that the battery capacity fading that might occur during the time when the battery is at rest is not accounted for by the adopted battery capacity fading model. It only computes the capacity fading due to cycling.

2.2 Supercapacitor (SC)

A capacitor is constructed from two conductor plates separated by a dielectric. When electric charges are accumulated on one conductor plate, the same amount of charges with opposite polarity will be induced on the second conductor plate. Consequently, an electric field will be formed between the two plates. The capacitance is defined as the ratio of the accumulated charge on each plate to the voltage difference between the plates. In other words, it governs how much charge will be deposited on the capacitor plates for one volts of applied voltage across the capacitor plates. The value of the capacitance is a function of conductor plate geometry and permittivity of the dielectric material. The theoretical expression of the capacitance is as follows:

$$C = \frac{\varepsilon_r \varepsilon_o A}{d} \tag{2-22}$$

where, ε_o is the permittivity of free space, ε_r relative permittivity of the dielectric, A area of conductor plates, and d distance between plates.

Theoretically, the capacitance of supercapacitors is governed by the same equation used for conventional capacitors. Consequently, to increase the capacitance of an SC, the area A of the conductor plates must be increased and their separation distance d must be decreased. Also, dielectric materials with high relative permittivity can be used to increase the capacitance.

It was found that the terminal I-V characteristics of supercapacitors do not coincide with that of conventional capacitors [43]. Consequently, researchers have constructed equivalent circuit models of

supercapacitors to allow for electrical system design and computer simulation. In [43], the equivalent circuit of the supercapacitor cell BCAP0350 by Maxwell Technologies was derived and parametrized. Figure 2.10 depicts the equivalent circuit of the SC cell. The governing equations and constant values of the SC cell equivalent circuit passive components are summarized in Table 2-1.

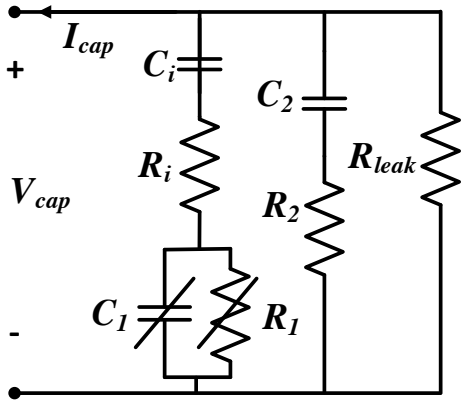


Figure 2.10: Supercapacitor equivalent circuit model [43]

Table 2-1: Parameter of SC equivalent circuit [43]

R_i (mΩ)	C_i (F)	C_1 (F)	R_1 (Ω)	R_2 (mΩ)	C_2 (F)	R_{leak} (Ω)
1.6	$2.18 + 88V_{cap}$	$\frac{C_i}{2}$	$\frac{2(1.57 + 0.643V_{cap})}{\pi^2 C_i}$	11.92	19	2500

The SC pack is modeled in the same way as the battery pack. All the resistances and capacitances are scaled by n_{sc}/m_{sc} and m_{sc}/n_{sc}, respectively. n_{sc} and m_{sc} denote the number of series SC cells in a string and parallel SC strings in the pack, respectively. The values of C_i and R_1 are dependent on the terminal voltage of the SC cell. Consequently, to compute the pre-scaled value of C_i and R_1 in the SC pack, the SC pack terminal voltage is scaled down by n_{sc}.

The SC stored energy E_{sc} is related to voltage and capacitance through the following equation:

$$E_{sc} = \frac{1}{2}CV^2 \tag{2-23}$$

The SC energy expenditure is related to its voltage excursion by equation (2-24), where U_{sc} represents the percentage of the SC stored energy at a voltage of V_{nom} that can be extracted if the SC is discharged to

V_{min}. The value of V_{nom} is constrained by the SC rated voltage and the external circuit, whereas V_{min} is constrained only by the external circuit.

$$U_{sc} = \frac{V_{nom}^2 - V_{min}^2}{V_{nom}^2} \tag{2-24}$$

2.3 Traction powertrain

Figure 2.11 depicts the traction powertrain of EVs with the partially-decoupled HESS. There are four main power processor units in the EV powertrain, i.e., transmission, electric motor, DC/AC converter (inverter), and DC/DC converter. The power drawn from the HESS is processed by these units to generate the traction propulsion power P_t at the wheels. The following subsections will discuss the adopted models for the traction powertrain components.

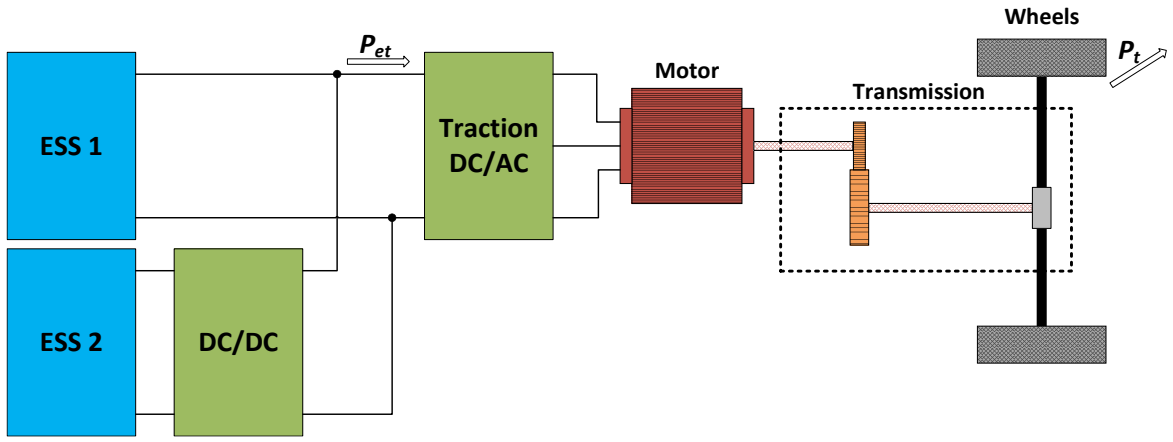


Figure 2.11: Traction powertrain of EVs with partially-decoupled HESS

2.3.1 Traction propulsion demand

The wheels traction power of the EV can be determined based on the vehicle longitudinal dynamics, drive cycle, and EV parameters. Figure 2.12 shows the forces free body diagram of a vehicle. Four forces resist the motion of the vehicle, i.e., aerodynamic drag (F_{ad}), rolling resistance (F_r), gradient resistance (F_g), and vehicle's inertia (F_i). The traction force (F_t) is applied in the direction of the vehicle's motion. The governing equations of these forces are as follows:

$$F_{ad} = \frac{1}{2}\rho A_f C_D v^2 \tag{2-25}$$

$$F_r = mgC_r \cos\alpha \tag{2-26}$$

$$F_g = mg \sin\alpha \tag{2-27}$$

$$F_i = m\frac{dv}{dt} \tag{2-28}$$

$$F_t = F_i + F_{ad} + F_r + F_g \tag{2-29}$$

where v is the vehicle speed in m/s, ρ air density in kg/m^3, A_f effective vehicle's frontal area in m^2, C_D aerodynamic drag coefficient, C_r rolling resistance coefficient, m vehicle's mass in kg, g gradational acceleration constant in m/s^2, and α gradient of the road in degrees.

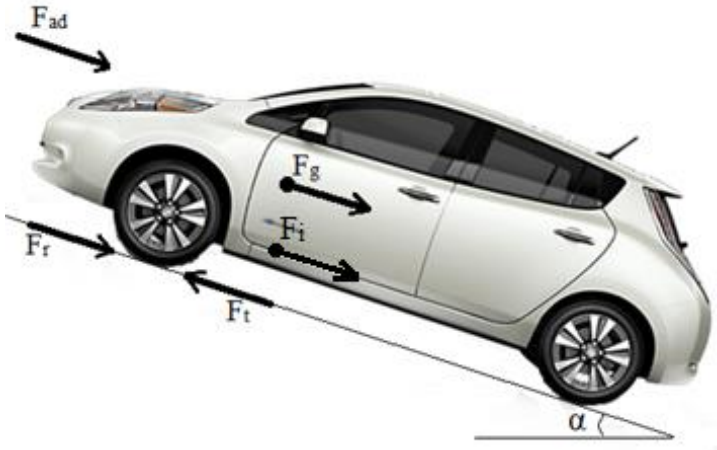


Figure 2.12: Vehicle forces free body diagram [44]

The wheels traction power P_t is computed by multiplying the traction force by the vehicle speed as follows:

$$P_t = F_t v \tag{2-30}$$

The wheels traction torque τ_w and rotational speed ω_w are calculated by scaling the traction force and vehicle's longitudinal speed by the wheels radius r_w as follows:

$$\tau_w = F_t r_w \tag{2-31}$$

$$\omega_w = \frac{v}{r_w} \tag{2-32}$$

2.3.2 Transmission

The transmission system is responsible for stepping up the motor's torque to drive the wheels. A fixed-gear-ratio (N_g) gearbox is assumed for the transmission. The efficiency η_t of the transmission system was assumed to be constant, following common practice [4]. Consequently, the relationship between the motor shaft torque τ_m and traction wheels torque τ_w is as follows:

$$\tau_m = \begin{cases} \tau_w \dfrac{1}{N_g \eta_t}, & \tau_w \geq 0 \\ \tau_w \dfrac{\eta_t}{N_g}, & otherwise \end{cases} \tag{2-33}$$

Similarly, the relationship between the motor shaft speed ω_m and traction wheels speed ω_w is as follows:

$$\omega_m = N_g \omega_w \tag{2-34}$$

2.3.3 Electric motor

In EV propulsion, AC machines are preferred over DC machines due their greater operating efficiency [27]. The squirrel cage induction machine (IM) is the most popular in EV applications, due to its low cost, lightweight, and high torque and power per volume capabilities. The second most popular AC machine is the permanent magnet synchronous machine (PMSM). It enjoys an even higher output torque per volume capability compared to the induction machine. However, it is generally more expensive than IM. Consequently, the induction machine will be assumed as the traction motor in this work.

When assessing the performance of a vehicle's power plant, acceleration from a stationary position to full speed is looked at. Ideally, it would be desired to maximize the power production as much as possible. Initially, the power plant would supply its maximum torque up to a particular speed at which the maximum power of the plant is reached. After that, the power plant maintains its maximum power output and allows the torque to drop gradually [4]. Figure 2.13 depicts the ideal torque-speed characteristics. Luckily, electrical IM drives normally operate according to the ideal toque-speed characteristics mentioned above, whereas IC engines' toque-speed characteristic deviates from the ideal characteristics, as shown in Figure 2.14.

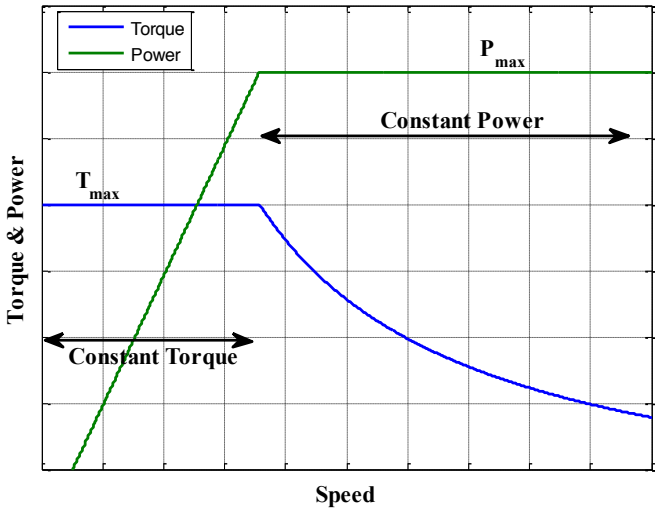


Figure 2.13: Ideal torque-speed characteristics of vehicles power plant

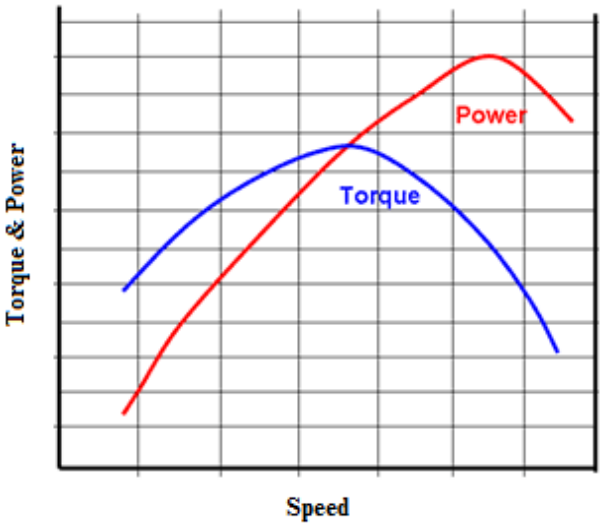


Figure 2.14: IC engines torque-speed characteristics [45]

Transient modeling of IM is not necessary for longitudinal dynamics simulation of EVs. Consequently, the classical per-phase induction machine equivalent circuit model will be used to model the power processed by the IM. Figure 2.15 depicts IM per-phase equivalent circuit with all components referred to the stator. The core resistance is normally omitted following common practice, in an attempt to simplify the analysis [46]. This allows for deduction of meaningful relationships with emphasis on the most dominant components. L_s and L_r are the stator and rotor leakage inductances, respectively, L_m magnetizing inductance, and R_s and R_r stator and rotor resistances, respectively. Further, the slip s is defined as follows:

$$s = \frac{w_{sy} - w_r}{w_{sy}} \tag{2-35}$$

where w_{sy} is the synchronous speed in rad/s and w_r rotor speed in rad/s. w_{sy} is defined in terms of the stator voltage frequency f_s and IM's number of poles N_p, as follows:

$$w_{sy} = \frac{4\pi}{N_p} f_s \tag{2-36}$$

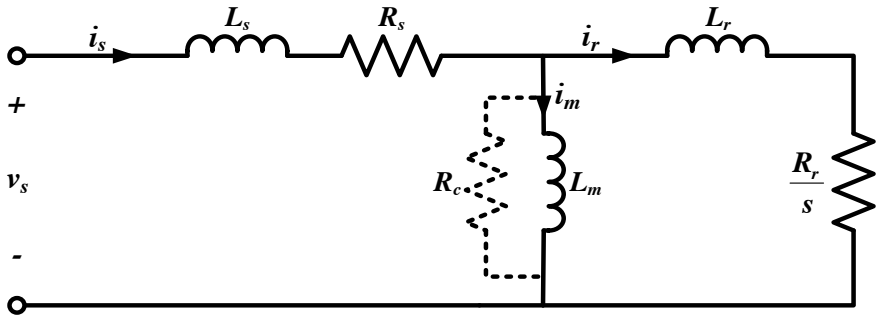


Figure 2.15: Induction machine per-phase equivalent circuit model

In the IM per-phase equivalent circuit model, the power consumed by the rotor resistance represents one-third of the air gap power P_{AG}. Consequently, the air gap power can be expressed in terms of the rotor current and R_r as follows:

$$P_{AG} = 3I_r^2 R_r \left(\frac{1}{s}\right) \tag{2-37}$$

Note that the use of capitalized letters for the current and voltage quantities represent their RMS values. For example, in (2-37) I_r represents the RMS value of i_r.

To construct a relationship between the rotor current and stator voltage, it is best to deduce the Thevenin equivalent circuit seen by the magnetization impedance looking back towards the input. Figure 2.15 shows the per-phase equivalent circuit model of IM with the input replaced by its Thevenin equivalent circuit.

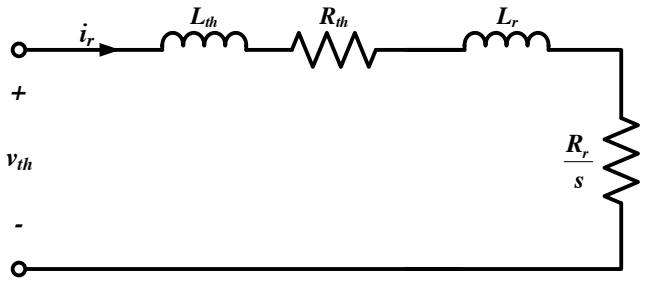


Figure 2.16: Thevenin equivalent circuit of IM

The Thevenin voltage v_{th} and impedance z_{th} are as follows:

$$v_{th} = \frac{jX_m}{R_s + j(X_s + X_m)} v_s \tag{2-38}$$

$$z_{th} = \frac{jX_m(R_1 + jX_1)}{R_1 + j(X_1 + X_m)} \tag{2-39}$$

The quantity X represents the reactance of the inductances, which is defined as $X=2\pi f_s L$. Typically, $X_m+X_s>>R_s$ and $X_m>>X_s$; thus, the real and imaginary parts R_{th} and X_{th} of the Thevenin impedance can be approximated as follows:

$$R_{th} \approx R_s \left(\frac{X_m}{X_s + X_m}\right)^2 \tag{2-40}$$

$$X_{th} \approx X_s \tag{2-41}$$

After applying the approximation mentioned above, the RMS value of v_{th} will be governed by (2-42). Similarly, the RMS value of the rotor current is governed by (2-43).

$$V_{th} \approx V_s \frac{X_m}{X_s + X_m} \tag{2-42}$$

$$I_r = \frac{V_{th}}{\sqrt{(R_{th} + R_r/s)^2 + (X_{th} + X_r)^2}} \tag{2-43}$$

The IM induced torque is equal to the load mechanical torque τ_{mech}, when core, friction, windage, and stray losses are neglected. Consequently, τ_{mech} can be expressed in terms of the air gap power and synchronous speed as follows:

$$\tau_{mech} = \frac{P_{AG}}{w_{sy}} = \frac{3V_{th}^2 R_r/s}{w_{sy}((R_{th} + R_r/s)^2 + (X_{th} + X_r)^2)} \tag{2-44}$$

Equation (2-44) governs the torque-speed characteristics of IM. An expression for the maximum torque can be deduced by either differentiating (2-44) with respect rotor speed or by circuit analysis. The circuit analysis approach will be followed, as it requires less mathematical effort. Maximizing P_{AG} implies maximizing τ_{mech}. From the IM equivalent circuit in Figure 2.16, based on circuit analysis, P_{AG} is maximum when the magnitude of the source impedance is equal to that of the load impedance.

$$R_r/s = \sqrt{R_{th}^2 + (X_{th} + X_r)^2} \tag{2-45}$$

Consequently, the slip s_{max} at which the maximum torque τ_{max} occurs is as follows:

$$s_{max} = \frac{R_r}{\sqrt{R_{th}^2 + (X_{th} + X_r)^2}} \tag{2-46}$$

From (2-44) and (2-46), τ_{max} can be deduced as follows:

$$\tau_{max} = \frac{3V_{th}^2}{2w_{sy}\left(R_{th} + \sqrt{R_{th}^2 + (X_{th} + X_r)^2}\right)} \tag{2-47}$$

The two user controlled variables are the stator voltage and frequency. However, no clear relation between theses quantities and τ_{max} are apparent from the expression in (2-47). Therefore, simplifications and expression manipulation will be pursued in an effort to construct a clear relationship between τ_{max} and the stator voltage and frequency. For most of the operating frequency range, $(X_{th}+X_r) >> R_{th}$. Consequently, from (2-36), (2-41), (2-42) and (2-47), τ_{max} becomes:

$$\tau_{max} \approx \frac{3}{16\pi^2} \frac{N_p L_m^2}{(L_m + L_s)^2 (L_r + L_s)} \left(\frac{V_s}{f_s}\right)^2 \tag{2-48}$$

From (2-48), maximum torque is directly proportional to the square of the stator voltage to frequency ratio. Therefore, in order to maintain the rated τ_{max} over a wind range of motor speed, it is necessary to increase V_s proportionally with f_s, as speed is increased.

The power factor *pf* of the IM is equal to the cosine of the phase difference, φ, between the IM line to neutral voltage and line current. Equivalently, φ can be computed as the negative of the phase angle of input

impedance z_{in} of the IM per-phase equivalent circuit. z_{in} and its angle are expressed in (2-49) and (2-50), respectively. Further, the IM *pf* is expressed in (2-51).

$$z_{in} = (R_s + jX_s) + (R_r + jX_r)||(jX_m) \tag{2-49}$$

$$\varphi = \tan\frac{Im\{z_{in}\}}{Re\{z_{in}\}} \tag{2-50}$$

$$pf = \cos(-\varphi) \tag{2-51}$$

The constant V/F IM drive control method is adopted. The ratio of V_s to f_s must be maintained constant as long as V_s has not saturated at its maximum value, constrained by the VSC and DC bus voltage. Consequently, V_s can be determined as follows:

$$V_s = \begin{cases} VF \cdot f_s, & V_s < V_{s,max} \\ V_{s,max}, & otherwise \end{cases} \tag{2-52}$$

where *VF* is the constant V_s to f_s ratio, which is chosen according to the desired maximum torque τ_{max} and the speed w_{base} at which the torque start to fall (see Figure 2.18). Further, the required f_s to operate the IM at the desired torque and speed can be computed by means of equations (2-44) and (2-52).

Similarly, the RMS value of stator current I_s can be calculated from z_{in} and V_s as follows:

$$I_s = \frac{V_s}{\sqrt{Im\{z_{in}\}^2 + Re\{z_{in}\}^2}} \tag{2-53}$$

2.3.4 Traction DC/AC converter (inverter)

The three-leg voltage source converter (VSC) is adopted by the industry as a motor drive for passenger EVs [4]. Figure 2.17 depicts the motor drive system in which the VSC is connected to the IM. In longitudinal dynamics simulation of EVs, the VSC is modeled as power processor that converts the DC power to AC power. The power losses in the VSC are accounted for by a pre-calculated efficiency map. The losses in the VSC are attributed to the switching and conduction losses. A detailed derivation of the VSC switching and conduction losses was presented in [26]. Equation (2-54) calculates the power losses in the VSC [26].

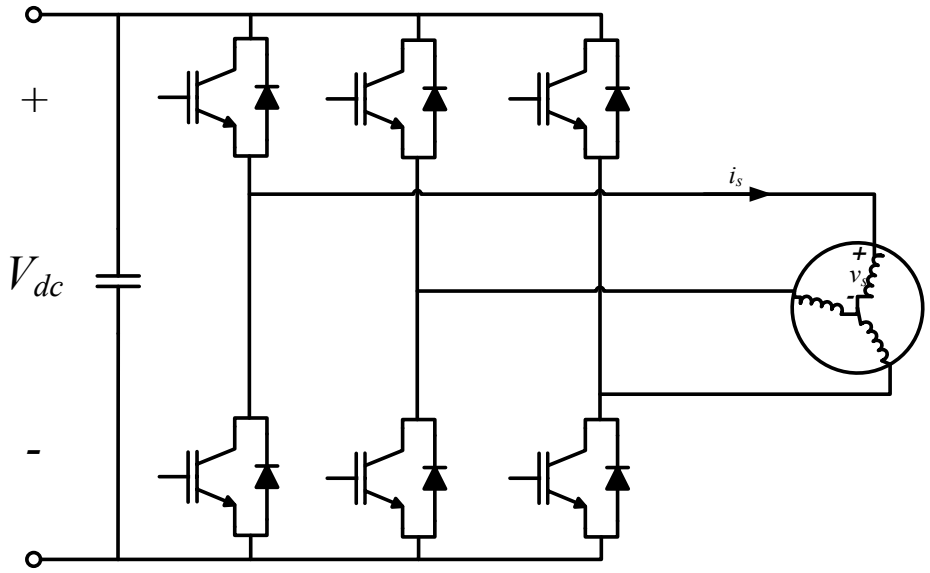


Figure 2.17: Traction inverter connected to IM

$$P_{loss}^{inv} = 3\left(\left(\frac{V_q - V_d}{4}\right)MIpf + \left(\frac{R_q + R_d}{4}\right)I_s^2 + \left(\frac{V_q + V_d}{\pi}\right)I_s + 2\left(\frac{R_q - R_d}{3\pi}\right)MI_s^2 pf + \frac{2k_{sw}\left(V_{dc}I_s\left(t_{on} + t_{off}\right)f_{sw}^{inv}\right)}{\pi}\right) \tag{2-54}$$

In (2-54), V_q and V_d are the constant voltage drops in the IGBT and diode, respectively, R_q and R_d on-resistances on of the IGBT and diode, respectively, k_{sw} a constant in the range of [1/6,1/2], t_{on} and t_{off} the turn-on and turn-off cross-over times, respectively, M PWM modulating index, I_s RMS of stator current, pf IM power factor, and f_{sw}^{inv} VSC switcing frequency.

The modulation index M can be calculated according to (2-55), which relates the DC bus voltage V_{dc} to the IM RMS fundamental AC line-to-neutral voltage V_s. The required value of pf, V_s, and I_s are determined according to the IM simulation model, governed by equations (2-51), (2-52), and (2-53), respectively.

$$V_s = \frac{1}{2\sqrt{2}}MV_{dc} \tag{2-55}$$

2.3.5 Minimum value of DC bus voltage

The maximum motor torque τ_{max} and the range of speed w_{base} for which τ_{max} can be sustained depend on the maximum AC voltage V_s that can be generated by the VSC at the motor stator. Figure 2.18 shows the torque-speed characteristic curves based on which the IM must be operated in order to maintain τ_{max}. After w_{base}, the IM torque will start to drop because the V/F ratio cannot be maintained constant, as V_s saturates at its maximum value, constrained by the VSC. The relationship between V_s and V_{dc} is governed by (2-55). Consequently, to find the minimum allowable DC bus voltage to meet the desired operation, (2-55) can be rearranged for V_{dc} while V_s and M take their maximum values. The maximum value of V_s can be determined according to the desired τ_{max} and w_{base} by using equation (2-47).

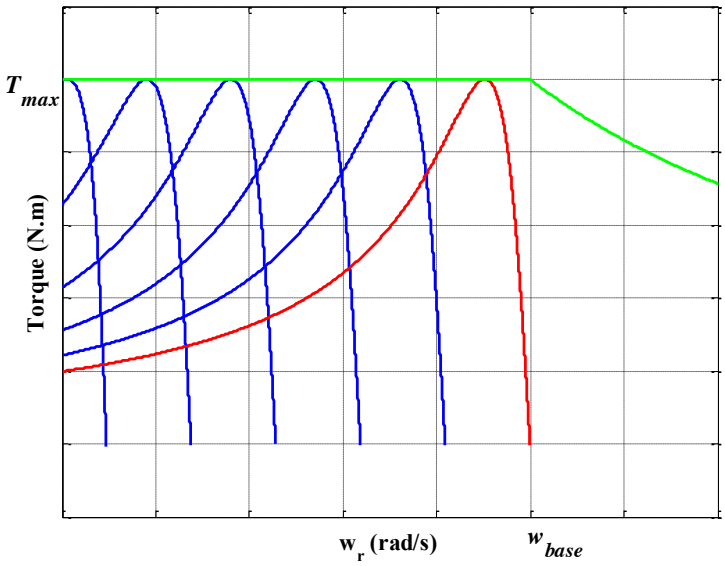


Figure 2.18: IM torque-speed characteristics for various synchronous speed values at constant V/F ratio

2.3.6 DC/DC converter

In EV drive cycle simulation, the short and fast dynamic transients of the currents and voltages in the DC/DC converter are not of interest, as these do not influence the magnitude of the power flow through the converter. Also, the DC/DC converter control system can regulate the converter's processed power very quickly. Consequently, the DC/DC converter can be modeled as a power transformer with an efficiency map to account for its power losses.

In this work, the half-bridge converter was adopted due to its operational simplicity, high efficiency, and low cost and weight [27], [47]. Figure 2.19 shows the half-bridge converter including the parasitic on-resistances and constant voltage drops of the semiconductor switches and inductor. The values of the semiconductors devices on-resistances and constant voltage drops are dependent on the adopted IGBT module. The method used in [48] is used to parametrize the on-resistances and constant voltage drops based on the IGBT module datasheet. The on-resistances and constant voltage drops can be determined from switches' I-V characteristics found in the IGBT module datasheet. Figure 2.20 shows the I-V characteristics of the power IGBT and diode. For the IGBT, the junction temperature and gate driving voltage affect the I-V characteristics. Normally, a high driving voltage is used to promote faster switching. In regards to the junction temperature, it is more conservative to choose the higher temperature, as the IGTB module will normally operate most of the time with high junction temperature. Consequently, the I-V characteristics curve with the higher junction temperature and gate driving voltage will be used to compute the on-resistances and constant voltage drops of the IGBT and diode.

The IGBT and diode I-V characteristics curves are fitted with a straight line. The inverse of the slope of the straight line is equal to the on-resistance, and the x-axis intercept of the straight line is equal to the constant voltage drop.

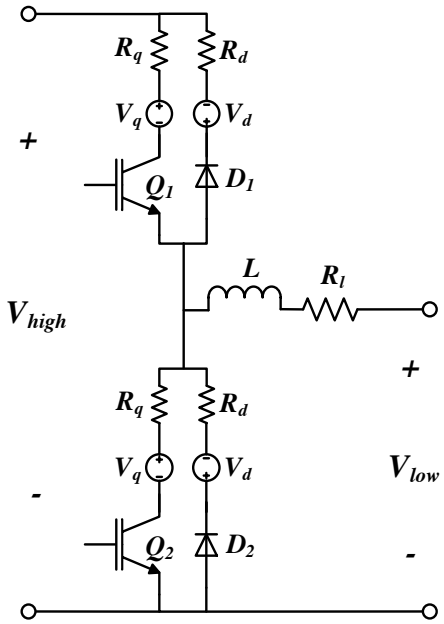


Figure 2.19: Half-bridge converter

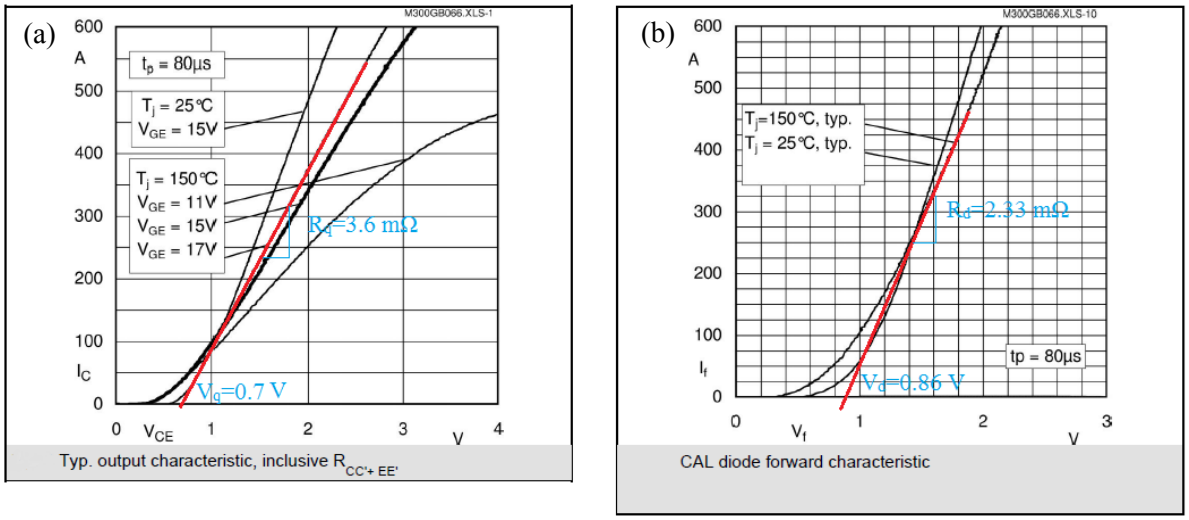


Figure 2.20: I-V characteristics of SKM 300GB066D module: (a) IGBT, and (b) diode [49]

In regards to the selection of the inductance value, a common guideline is to choose it according to the permissible inductor current ripple. Ignoring parasitic losses, the inductor ripple in the half-bridge converter can be estimated by (2-56) [27]. The inductor current ripple is lower when parasitic losses are included compared to what is obtained by (2-56). Thus, the result obtained by (2-56) is conservative.

$$\Delta i_L = \frac{1}{2Lf_{sw}^{DC}} \frac{V_{low}}{V_{high}} \left(V_{high} - V_{low}\right) \tag{2-56}$$

In (2-56), f_{sw}^{DC} is the DC/DC converter switching frequency. The conduction power losses $P_{R,loss}$ and $P_{V,loss}$ in the parasitic on-resistances and constant voltage drops are calculated according to the following equations:

$$P_{R,loss} = Ri_{RMS}^2 \tag{2-57}$$

$$P_{V,loss} = Vi_{avg} \tag{2-58}$$

Equations (2-57) and (2-58) call for the RMS and average values of the current through the converter elements. The inputs to the DC/DC converter efficiency map are the voltages of the low and high voltage sides, and the controlled average inductor current I_L. Consequently, i_{RMS} and i_{avg} must be expressed as a function of these quantities. During boost operation, where the power flows from the low to high voltage side, IGBT Q_2 and diode D_1 carry the inductor current. Figure 2.21 shows typical waveforms for the current through the inductor, IGBT Q_2, and diode D_1 during the boost operation.

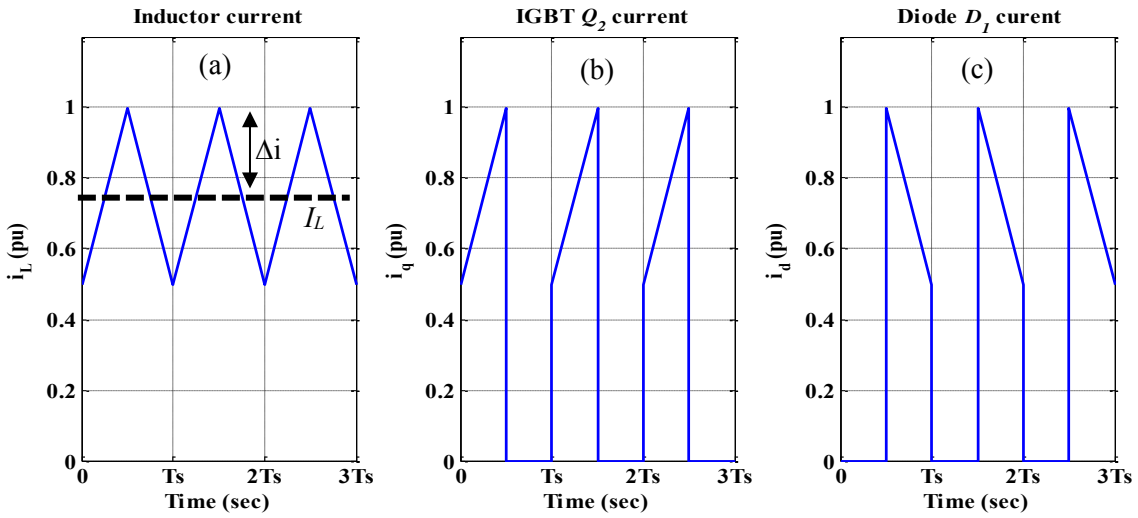


Figure 2.21: DC/DC converter currents during boost operation (pu): (a) inductor, (b) IGBT, and (c) Diode

Equation (2-59) governs the steady state duty cycle that the converter needs to operate at to maintain the average inductor current for given voltage levels at the high and low voltage sides. Equation (2-60) governs the inductor current ripple. Equations (2-61) to (2-65) govern the average and RMS values of the currents through the diode D_1, IGBT Q_2, and inductor. Equation (2-66) governs the total conduction losses in the converter during the boost operation.

$$D = \frac{V_{low} - I_L(R_L + R_q) + V_q}{I_L(R_d - R_q) + V_d + V_{high} - V_q} \tag{2-59}$$

$$\Delta i = \frac{(1-D)(V_{low} - I_L(R_L + R_q) - V_q)}{2Lf_{sw}^{DC}} \tag{2-60}$$

$$i_{d1,avg} = I_L D \tag{2-61}$$

$$i_{d1,RMS} = \sqrt{D(I_L - \Delta i)^2 + 2D\Delta i I_L} \tag{2-62}$$

$$i_{q2,avg} = (1-D)I_L \tag{2-63}$$

$$i_{q2,RMS} = \sqrt{(1-D)(I_L - \Delta i)^2 + 2(1-D)\Delta i I_L} \tag{2-64}$$

$$i_{L,RMS} = \sqrt{(I_L - \Delta i)^2 2\Delta i I_L} \tag{2-65}$$

$$P_{con}^{DC} = i_{d1,avg}V_d + {i_{d1,RMS}}^2 R_d + i_{q2,avg}V_q + {i_{q2,RMS}}^2 R_q + {i_{L,RMS}}^2 R_L \tag{2-66}$$

During the buck operation, on the other hand, the inductor current flows through the IGBT Q_1 and diode D_2. Equations (2-67) to (2-73) govern the duty cycle, inductor current ripple, average and RMS of the IGBT Q_1 and diode D_2 currents, and total conduction losses. The governing equation for the inductor current RMS is the same as that for the boost operation, which is (2-65).

$$D = \frac{-V_{low} - I_L(R_L + R_d) - V_d}{I_L(R_q - R_d) + V_q - V_{high} - V_d} \tag{2-67}$$

$$\Delta i = \frac{D\left(V_{high} - V_{low} - I_L(R_L + R_q) - V_q\right)}{2Lf_{sw}^{DC}} \tag{2-68}$$

$$i_{q1,avg} = I_L D \tag{2-69}$$

$$i_{q1,RMS} = \sqrt{D(I_L - \Delta i)^2 + 2D\Delta i I_L} \tag{2-70}$$

$$i_{d2,avg} = (1 - D)I_L \tag{2-71}$$

$$i_{d2,RMS} = \sqrt{(1 - D)(I_L - \Delta i)^2 + 2(1 - D)\Delta i I_L} \tag{2-72}$$

$$P_{con}^{DC} = i_{q1,avg}V_q + {i_{q1,RMS}}^2 R_q + i_{d2,avg}V_d + {i_{d2,RMS}}^2 R_d + {i_{L,RMS}}^2 R_L \tag{2-73}$$

The switching losses were accounted for by an empirical equation derived for Semikron IGBT modules [50]. Normally, for reference conditions of the current magnitude, high side voltage, and junction temperature, IGBT module datasheets include energy loss E_{off} and E_{on} in *mJ* during the switching on and off transitions of the IGBT. They also include switch loss E_{rr} of the diode due to reverse recovery. Equation (2-74) estimates the actual switching losses based on the reference conditions [50].

$$E_{sw} = E_{sw,ref}\left(\frac{I}{I_{ref}}\right)^{Ki}\left(\frac{V_{cc}}{V_{cc,ref}}\right)^{Kv}\left(1 + TC_{sw}\left(T_j - T_{j,ref}\right)\right) \tag{2-74}$$

where Ki is the exponent of current dependency, Kv exponent of voltage dependency, TC_{sw} temperature coefficient of switching losses, I input current in A, V_{cc} high side voltage in V, and T_j junction temperature in °C. The quantities with subscript *ref* are the reference conduction values quoted in the IGBT module datasheet. To compute the switching losses of the IGBT and diode, $E_{sw,ref}$ is set to be equal to E_{off}+E_{on} and E_{rr}, respectively.

Consequently, the total DC/DC converter losses P_{loss}^{DC} is computed as follows:

$$P_{loss}^{DC} = P_{con}^{DC} + f_{sw}^{DC}E_{sw} \tag{2-75}$$

2.4 Dynamic programming

Dynamic programming (DP) is a mathematical technique that is used to solve multistage decision optimization problems. A large problem is broken down into smaller sub-problems, and each sub-problem is solved independently. Then, the optimal solution to the complete problem is deduced from the solution of the sub-problems.

Dynamical system control problem is one of the classical DP optimization problems in which the DP solver will determine the optimal control and states trajectories to optimize a particular objective. Also, the DP solver grantees finding the global optimal solution.

The discrete form of DP will be adopted, as it calls for much easier and efficient software implementation compared to the continuous version of DP. Also, it is a common practice in the literature to use discrete DP to solve dynamical system optimal control problems [51]. A minor deviation from the global optimal solution will be induced in the discrete version of DP, due to the discretization of the search space. However, this deviation is minimal compared to that of the analytical solution solved the continuous version of DP [51].

The general mathematical formulation of discrete DP optimization problem is as follows:

$$J_0(x_0) = \min_{u_k} \left\{ g_N(x_N) + \sum_{k=0}^{N-1} g_k(x_k, u_k, w_k) \right\} \tag{2-76}$$

Subject to

$$x_{k+1} = f_k(x_k, u_k, w_k) \; \forall k = 0,1 \dots, N-1 \tag{2-77}$$

$$x_k \in X_k \; \forall k = 0,1 \dots, N \tag{2-78}$$

$$u_k \in U_k \; \forall k = 0,1 \dots, N-1 \tag{2-79}$$

where, x_k, u_k, and w_k are the vectors of system states, control inputs, and disturbances, respectively, X_k and U_k the sets for all admissible states and control inputs, respectively, $J_0(x_0)$ the optimized cost function, $g_k(\cdot)$ the performance index whose summation over time is the cost function to be optimized, and $f_k(\cdot)$ is the states update equation which is derived from the dynamical system governing differential equations.

The states-space is quantized into a grid. The cost function $J_k(x_k)$ is only evaluated on states-space grid points. The DP algorithm recursively solves for the optimal cost function at each states-space grid point for every stage backwards until it reaches the first stage. This is mathematically represented as follows:

Stage N:

$$J_N(x_N) = g_N(x_N) \tag{2-80}$$

Stage N-1 to 0:

$$J_k(x_k) = \min_{u_k}\{g_k(x_k, u_k, w_k) + J_{k+1}(x_{k+1})\} \tag{2-81}$$

Figure 2.22 demonstrates the computation of the cost function at a quantized point in the space of a single-state system. In this simple example, the states-space is quantized in three points, namely x^1, x^2, and x^3. The cost function at stage k at the quantized grid point x_k^2 is to be computed. All admissible controls are applied to the system. In this example, the control input space is quantized into three grid point as well, namely u^1, u^2, and u^3. Each control value drives the system state according the state update equation (2-77) from stage k to stage $k+1$. If the state x_{k+1} coincide with a quantized grid point at stage $k+1$, the cost-to-go $J_{k+1}(x_{k+1})$ will take the cost assigned to that gird point. Further, if the state x_{k+1} falls between grid points, the value of the cost-to-go $J_{k+1}(x_{k+1})$ will be linearly interpolated between the costs assigned to the bounding grid points. In the last case, if the state x_{k+1} falls out of the quantized grid space, the cost-to-go $J_{k+1}(x_{k+1})$ will be assigned a predetermined penalty value. The cost assigned to the grid point x_2 at stage k is the minimum of the summation of the cost-to-go and performance index $g_k(\cdot)$ cost for all admissible controls. Also, the optimal control quantized value is recorded for that state grid point.

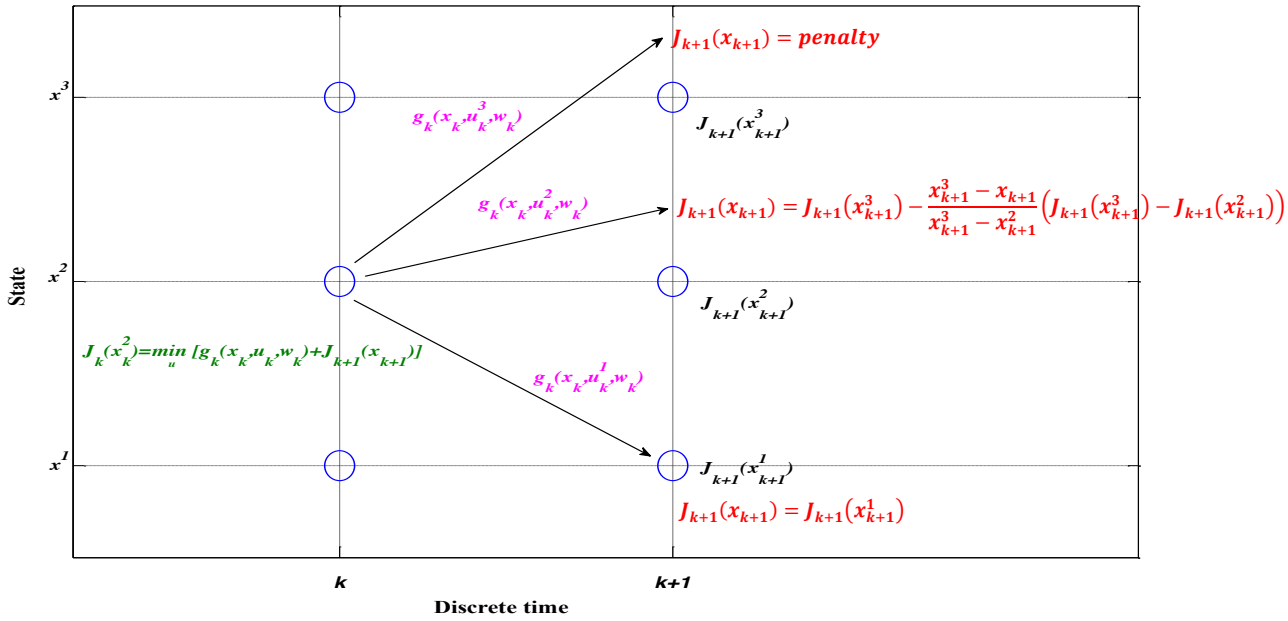


Figure 2.22: DP of single state system

The procedure described above is performed for every quantized states-space grid point at every stage. The cost at the last stage *N* is determined according to the problem constraints on hand. If it was desired to restrict the system's final states to a particular set, then the cost for all grid points outside that set must be assigned the penalty value. As an example for this case, consider the change sustenance energy management problem for HEV applications, whereby the battery SoC is required to be within a particular range at the end of the drive cycle.

The choice of the penalty value is not unique. It should not be infinity, as this may incorrectly penalize the cost at a state grid point when interpolation is used. However, it is chosen by an iterative process. It should be greater than the maximum cost at the first stage that would be invoked by the problem itself [51].

Finally, the recovery of the optimal control sequence is done as follows. At the first stage k=1, the recorded control value u_1 at the desired initial state is used to compute x_2 via $f_1(\cdot)$. If x_2 coincides with a quantized grid point, then u_2 takes the control value that was recorded for that grid point. If x_2 falls between grid points, then u_2 is found by linear interpolation between the recorded control values for the bounding states grid points. This process is followed to compute the control sequence until stage *N-1* is reached.

Chapter 3
Simulation Results and Discussion

In this chapter, the battery capacity fading quantification study is conducted via simulation, whereby the HESS is used to drive the EV over the drive cycle. Figure 3.1 shows a simplified block diagram of the vehicle simulation model. First, the drive cycle speed versus time data are fed to the vehicle longitudinal dynamics model to compute the required wheels torque and speed to meet the drive cycle. The wheels torque and speed data are then fed to the vehicle powertrain model and energy management system. Via dynamic programming, the energy management system determines the optimal power split between the battery and SC over the full drive cycle to minimize the battery capacity fading. The DC/DC converter low-side current is controlled to split the power between the battery and SC; thus, the output of the energy management is the optimal trajectory of the DC/DC converter low-side current set-points. Subsequently, the power flow in the vehicle powertrain is simulated, which ultimately outputs the battery data, i.e., SoC, Ah_{proc}, and cells temperature that are fed to the battery capacity fading model to compute the battery capacity loss. In the following subsection, the adopted values of the simulation models parameters are presented.

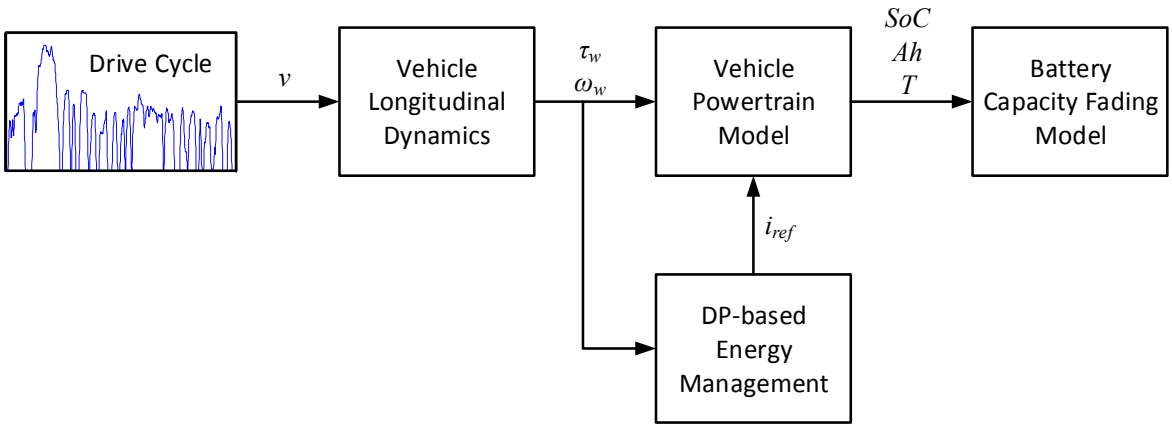


Figure 3.1: Simplified block diagram of the simulation model

3.1 Simulation models parameters

Nissan Leaf was chosen as the sample EV for this study. Table 3-1 summarizes Leaf's parameters as well as the environment parameters that are used in the vehicle longitudinal dynamics (2-25) to (2-29).

Table 3-1: Nissan Leaf and environment parameters

Effective vehicle frontal area A_f (m^2) [52]	2.59
Aerodynamic drag coefficient C_D [52]	0.28
Rolling resistance coefficient C_r [4]	0.0125
Vehicle mass (excluding ESS) (kg) [44]	1,177
Gearbox ratio N_g [53]	7.94
Wheel radius r_w (m) [44]	0.3
Air density ρ (kg/m^3)	1.225
Gravitational acceleration g (m/s^2)	9.81

A typical constant value of 96% was chosen for the transmission efficiency η_t [4]. Further, the parameters of the traction inverter power loss model and IM per-phase equivalent circuit model are summarized in Table 3-2 and Table 3-3, respectively [26]. The inverter switching frequency f_{sw}^{inv} is assumed to be 21 times the fundamental frequency of the stator current [26].

The desired values of the IM maximum torque τ_{max} and constant torque speed range ω_{base} dictate the acceleration performance of the vehicle. In this work, τ_{max} was set to 370 N.m and ω_{base} was set to 523 rad/s, which correspond to a longitudinal velocity of about 70 km/h.

Table 3-2: Traction inverter power loss model parameters [26]

R_q (mΩ)	R_d (mΩ)	V_q (V)	V_d (V)	t_{on} (μs)	t_{off} (μs)	k_{sw}
13.2	16	1.25	0.7	0.09	0.15	0.25

Table 3-3: IM per-phase equivalent circuit parameters [26]

L_m (μH)	L_s (μH)	L_r (μH)	R_s (mΩ)	R_r (mΩ)	N_p
1,438.01	38.77	38.77	7.43	4.73	4

The nominal value of the DC bus voltage must be chosen according to the desired τ_{max} and ω_{base}, which is computed by means (2-47) and (2-55). Further, the computed nominal DC bus voltage is scaled up by 20% as a safety margin to account for tolerances, such as voltage drops across internal impedances. Consequently, the required DC bus voltage to support the desired τ_{max} and ω_{base} is about 363 V. Further, the constant V/F ratio of the traction motor speed control system was accordingly set to 0.681.

The summation of core, friction, windage, and stray losses are modeled as a fixed percentage of the load power, which was taken to be 10% [26]. Accordingly, the efficiency map of the combined traction inverter-motor system is shown in Figure 3.2.

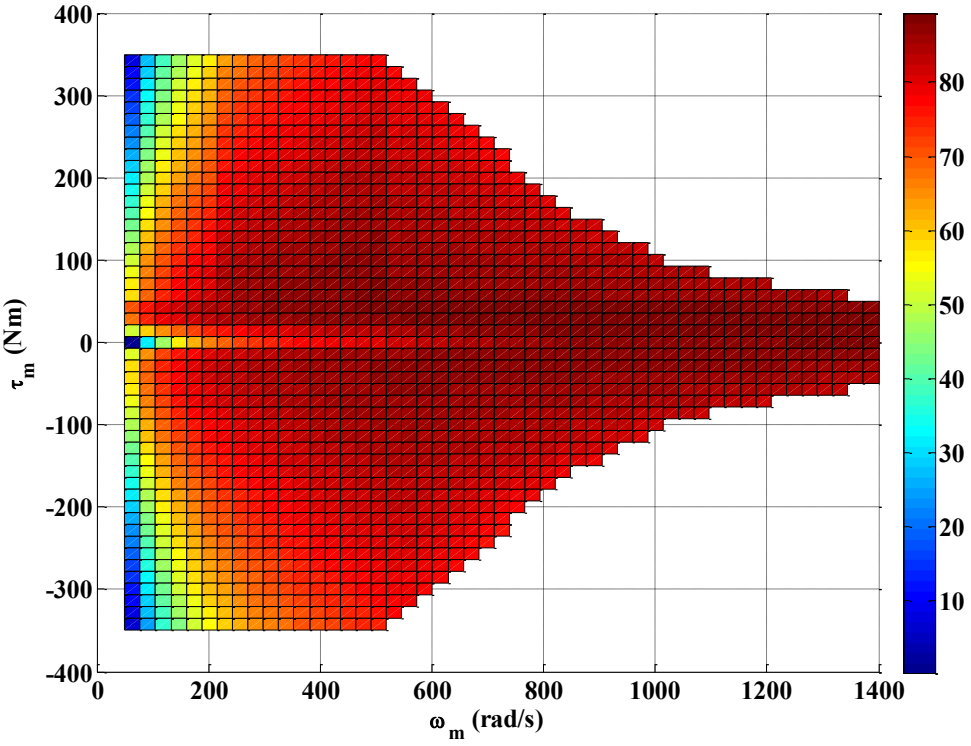


Figure 3.2: Combined inverter-motor system efficiency map

For the DC/DC converter, the IGBT module SKM 300GB066D by Semikron was adopted. Based on the module's datasheet, the values of the on-resistances and constant voltage drops for both the IGBT and diode were determined and summarized in Table 3-4. A typical value of 10% inductor current ripple was assumed. At nominal voltage levels of about 363 V and 265 V for the high and low-side of the DC/DC converter, respectively, nominal inductor current of 100 A, and switching frequency f_{sw}^{DC} of 20 kHz, the inductance value must be greater than 194 µH. Subsequently, the inductance value will be rounded up to 200 µH.

Further, the parasitic resistance of the inductor will be taken to be 10 mΩ. The values of the parameters used in the DC/DC converter switching loss model are summarized in Table 3-5. Consequently, the efficiency map of the DC/DC was constructed, and it is shown in Figure 3.3. Originally, the inputs to the DC/DC converter efficiency map were the high-side voltage, low-side voltage, and low-side current. However, the high-side voltage had a weak influence on the efficiency map. Therefore, the low-side voltage and low-side current are considered as the inputs to the efficiency map.

Table 3-4: DC/DC converter conduction power loss model parameters

R_q (mΩ)	R_d (mΩ)	V_q (V)	V_d (V)	L (μH)	R_L (mΩ)	f_{sw}^{DC} (kHz)
3.6	2.33	0.7	0.86	200	10	20

Table 3-5: DC/DC converter switching power loss model parameters [50]

Parameter	Value	Parameter	Value
$E_{on,ref}$ (mJ)	7.5	T_{ref} (°C)	150
$E_{off,ref}$ (mJ)	11.5	K_i	1.00 for IGBT 0.55 for diode
$E_{rr,ref}$ (mJ)	10.5	K_v	1.3 for IGBT 0.6 for diode
I_{ref} (A)	150	TC_{sw}	0.0030 for IGBT 0.0055 for diode
V_{ref} (V)	300		

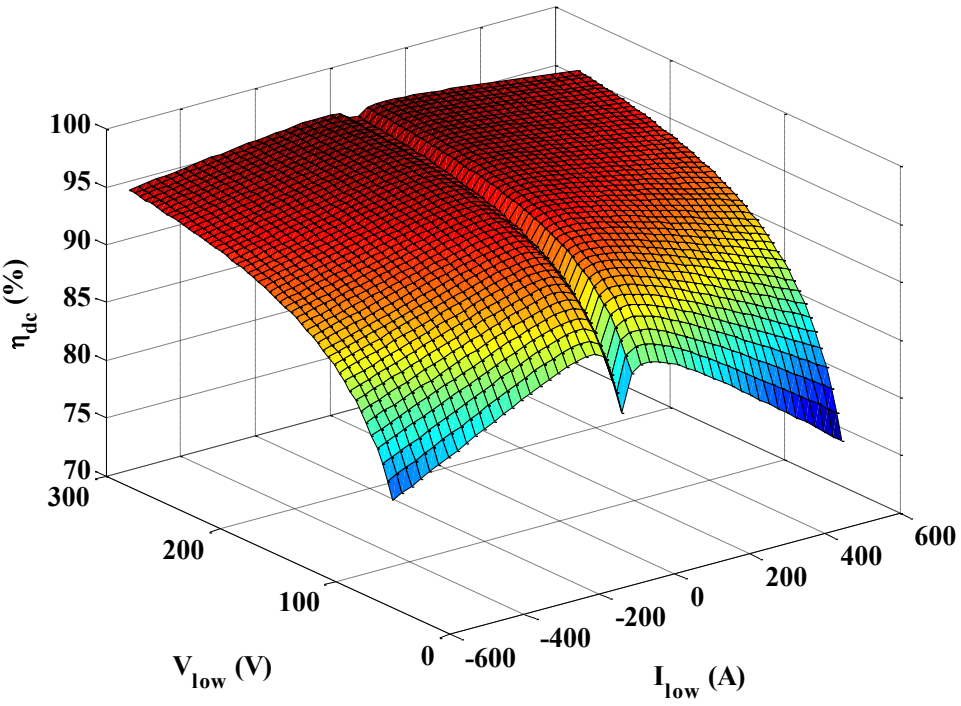


Figure 3.3: DC/DC converter efficiency map

The mass to power rating ratio (kg/kW) of DC/DC converters for EV applications is not readily available in the literature or from industry. Therefore, the following approach is followed to estimate that ratio. In [54], a commercial 50 kW DC/DC converter module that consisted only of the IGBT module, heat sink, and control boards weighed 13 kg. Further, in [55], a complete 40 kW half-bridge DC/DC converter for electric vehicles was designed. The weight of electrolytic capacitors, inductor, and housing constituted 69% of the converter's total weight. However, the total weight of the converter was not given. Thus, to estimate the mass per power ratio of DC/DC converters for EVs, the figures from [54] and [55] are used. Assuming that the IGBT module, heat sink, and control boards in [54] represent 31% of the total weight, the total weight of the 50 kW converter is 42 kg. As a result, the adopted converter mass per power ratio is 0.84 kg/kW.

The DC/DC converter rating in SC-DC topology is chosen to be 40 kW to match the traction demand; thus, its weight would be 33.6 kW. Similarly, the DC/DC converter rating in Bat-DC topology is chosen to be as low as 10 kW, as the battery will only supply the base power from the low-voltage side. Thus, the weight of the converter would be 8.4 kg.

The battery cell APR26650 by A123 Systems and the SC cell BCAP350F by Maxwell Technologies are adopted in this work. The parameters of their equivalent circuit models were presented in sections 2.1.2 and 2.2. Further, Table 3-6 and Table 3-7 represent the most notable specifications of the adopted battery and SC cells, respectively.

Table 3-6: Battery cell APR26650 specifications

Parameter	Value
Nominal voltage (V)	3.3
Charge capacity (Ah)	2.3
Nominal series resistance (mΩ)	10
Mass (g)	76

Table 3-7: SC cell BCAP350F specifications

Parameter	Value
Maximum voltage (V)	2.5
Capacitance (F)	350
Nominal series resistance (mΩ)	3.2
Mass (g)	60

3.2 Energy management

The energy management algorithm issues the DC/DC converter low-side current set-points to control the power split between the battery and SC. The energy management problem is formulated as a deterministic optimal control problem that is solved by dynamic programming. The battery capacity fading is the cost to be minimized in the optimization problem.

DP is computationally expensive, and the computational effort increases exponentially with the number of states. Therefore, the equivalent circuit models of the battery and SC cells must be simplified, as they comprise a system of eight states. From simulations, it was observed that the battery temperature rise over the drive cycle was in the order of tenths of a degree Celsius. This is due to the implicit assumption in the

adopted battery thermal model that the battery cooling system is circulating a cooling air at a specific flow rate and a temperature of 26°C. Thus, the temperature dynamics of the battery will be omitted, and the battery temperature will be fixed at 26°C. Similarly, the battery equivalent circuit model will be simplified to an SoC-dependent voltage source and a series resistance. The dynamics of the series R-C networks are slow, and their steady-state voltage drops are much lower than that of the series resistance. The value of the series resistance is taken to be constant, as it is only temperature dependent as per (2-2) and the battery cell temperature is maintained almost constant by the cooling system. Similarly, the SC equivalent circuit model is simplified to a capacitor and a series resistor, with constant capacitance and resistance, respectively. The simplified models of the battery and SC cells will still preserve terminal voltage and current characteristics with acceptable details.

It is worth mentioning that the regenerative braking power throughout the drive cycle simulation is always lower than the ratings of traction motor and inverter. Therefore, the EV's braking power is assumed to be entirely processed by the HESS rather than mechanical braking. Furthermore, since the temperature dynamics of the battery are omitted, the battery capacity fading governed by (2-19) would solely be susceptible to the battery Ah processed. Consequently, the performance index $g_k(\cdot)$ of the DP optimization problem is chosen to be:

$$g_k(x_k, u_k, w_k) = \left|i_{bat,k}\right| \tag{3-1}$$

3.2.1 SC-DC simplified model

Figure 3.4 depicts the simplified equivalent circuit of the SC-DC topology. The following set of equations governs the power flow in the HESS as well as the states dynamics. Equations (3-2) to (3-9) are solved sequentially to compute $i_{sc,k}$ and $i_{bat,k}$. Equations (3-10) and (3-11) are the states update equations. All variables and their sign conventions used in (3-2) to (3-11) are labeled in Figure 3.4. The symbol ⊡ in Figure 3.4 represents a power source that realizes (3-5). Recall that the parameters with a superscript "′" represent the lumped pack element, which scales the single cell elements by the number of series cells in a string and parallel strings, as presented in sections 2.1 and 2.2.

$$i_{sc,k} = i_{dc,k} \tag{3-2}$$

$$v_{sc,k} = v_{c,k} - i_{sc,k} r_{sc}{}' \tag{3-3}$$

$$P_{sc,k} = v_{sc,k} i_{sc,k} \tag{3-4}$$

$$P_{high,k} = \begin{cases} P_{sc,k}\eta_{dc,k}, & i_{sc,k} \geq 0 \\ \dfrac{P_{sc,k}}{\eta_{dc,k}}, & i_{sc,k} < 0 \end{cases} \tag{3-5}$$

$$P_{bat,k} = P_{te,k} + P_{a,k} - P_{high,k} \tag{3-6}$$

$$v_{oc,k}{}' = \left(a_1 e^{-a_2 SoC_k} + a_3 + a_4 SoC_k + a_5 e^{\left(-a_6/1-SoC_k\right)}\right) n_b \tag{3-7}$$

$$V_{bat,k} = \frac{v_{oc,k}{}'}{2} + \frac{\sqrt{v_{oc,k}{}' - 4r_b{}' P_{bat,k}}}{2} \tag{3-8}$$

$$i_{bat,k} = \frac{P_{bat,k}}{v_{bat,k}} \tag{3-9}$$

$$SoC_{k+1} = SoC_k - \frac{i_{ibat,k}}{Q \cdot 3600 \cdot m_b} \tag{3-10}$$

$$v_{c,k+1} = v_{c,k} - \frac{i_{sc,k}}{C'} \tag{3-11}$$

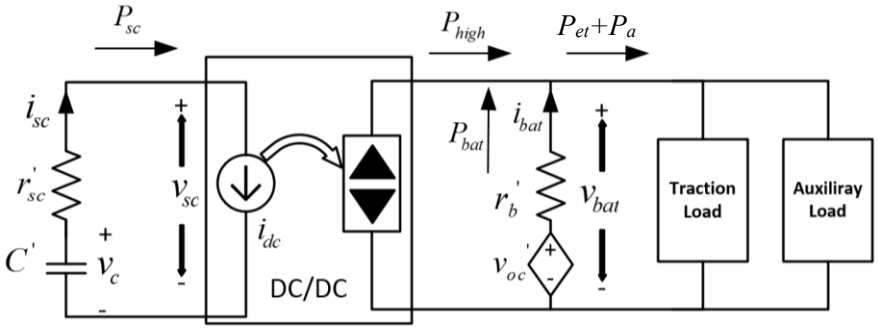


Figure 3.4: Simplified SC-DC equivalent circuit model

3.2.2 Bat-DC simplified model

Bat-DC topology has a variable structure. When the DC bus voltage drops to the level of the battery terminal voltage, the bypass diode clamps the battery voltage to that of the DC bus. Figure 3.5 depicts the simplified equivalent circuit models for both possible structures of Bat-DC. The following set of equations governs the power flow in the Bat-DC HESS. The states update equations for the Bat-DC topology are the same as those for the SC-DC topology. Note that the bypass diode is modeled as an ideal diode.

$$v_{bat1,k} = \frac{v_{oc,k}{}' - r_b{}' i_{dc,k}}{2} + \frac{\sqrt{\left(v_{oc,k}{}' - r_b{}' i_{dc,k}\right)^2 - 4 r_b{}' P_a}}{2} \tag{3-12}$$

$$v_{bat2,k} = \frac{\frac{v_{oc,k}{}'}{r_b{}'} + \frac{v_{c,k}}{r_{sc}{}'}}{2 r_{eq}} + \frac{\sqrt{\left(\frac{v_{oc,k}{}'}{r_b{}'} + \frac{v_{c,k}}{r_{sc}{}'}\right)^2 - 4 r_{eq}\left(P_{a,k} + P_{te,k}\right)}}{2 r_{eq}} \tag{3-13}$$

$$v_{bat,k} = \begin{cases} \alpha_k v_{bat1,k} + (1 - \alpha_k) v_{bat2,k}, & P_{te,k} \geq 0 \\ v_{bat1,k}, & P_{te,k} < 0 \end{cases} \tag{3-14}$$

$$P_{dc,k} = v_{bat1,k} i_{dc,k} \tag{3-15}$$

$$P_{high,k} = \begin{cases} P_{dc,k} \eta_{dc,k}, & i_{dc,k} \geq 0 \\ \frac{P_{dc,k}}{\eta_{dc,k}}, & i_{dc,k} < 0 \end{cases} \tag{3-16}$$

$$P_{sc,k} = P_{te,k} - P_{dc,k} \tag{3-17}$$

$$V_{sc1,k} = \frac{v_{c,k}}{2} + \frac{\sqrt{v_{c,k} - 4 r_{sc}{}' P_{sc,k}}}{2} \tag{3-18}$$

$$V_{sc2,k} = v_{bat2,k} \tag{3-19}$$

$$v_{sc,k} = \begin{cases} \alpha_k v_{sc1,k} + (1 - \alpha_k) v_{sc2,k}, & P_{te,k} \geq 0 \\ v_{sc1,k}, & P_{te,k} < 0 \end{cases} \tag{3-20}$$

$$\alpha_k = \begin{cases} 1, & v_{sc1,k} - v_{bat1,k} \geq 0 \\ 0, & v_{sc1,k} - v_{bat1,k} < 0 \end{cases} \tag{3-21}$$

$$i_{bat,k} = \frac{v_{oc,k}{}' - v_{bat,k}}{r_b{}'} \tag{3-22}$$

$$i_{sc,k} = \frac{v_{c,k} - v_{sc,k}}{r_{sc}{}'} \tag{3-23}$$

The variables v_{bat1} and v_{sc1} represent the battery and SC packs' terminal voltages when the bypass diode is not conducting. Similarly, v_{bat2} and v_{sc2} are the battery and SC packs' terminal voltages when the bypass diode is conducting. Further, the variable r_{eq} in equation (3-13) is equal to ($1/r_b{}' + 1/r_{sc}{}'$).

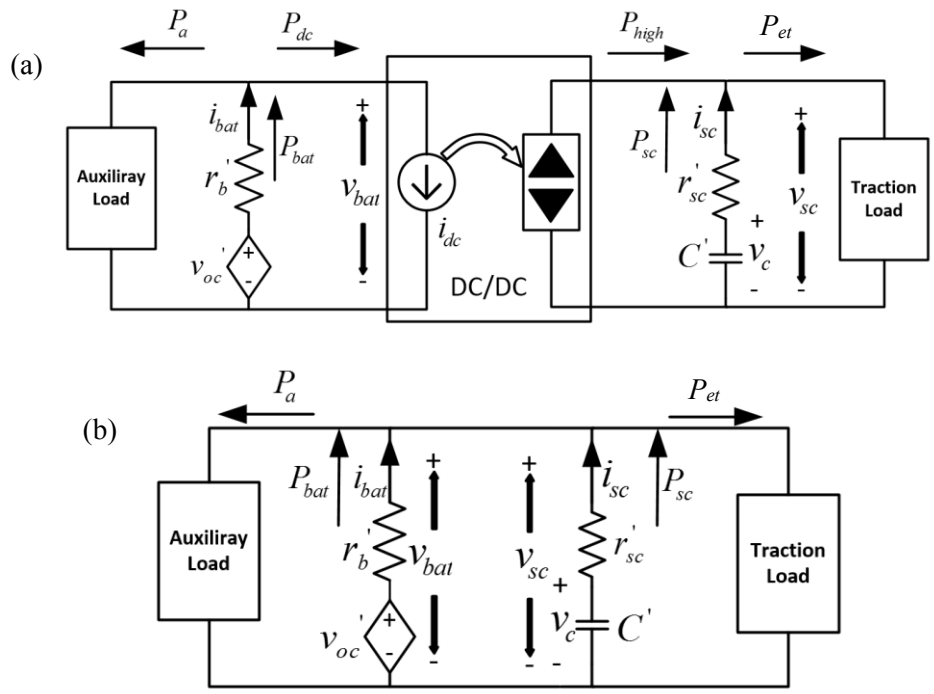


Figure 3.5: Simplified Bat-DC equivalent circuit model: (a) bypass diode not conducting, and (b) bypass diode conducting

3.3 Case study 1: effect of drive cycle type and initial SC SoC

In this case study, two drive cycles were considered, urban and highway. Both drive cycles comprise a total driving distance of 24 km. For the urban drive cycle, the FTP-72 drive cycle was duplicated to emulate a round trip, whereas for the highway drive cycle, the EPA highway drive cycle was modified and extended such that the driving distance was 24 km. Figure 3.6 depicts the drive cycles.

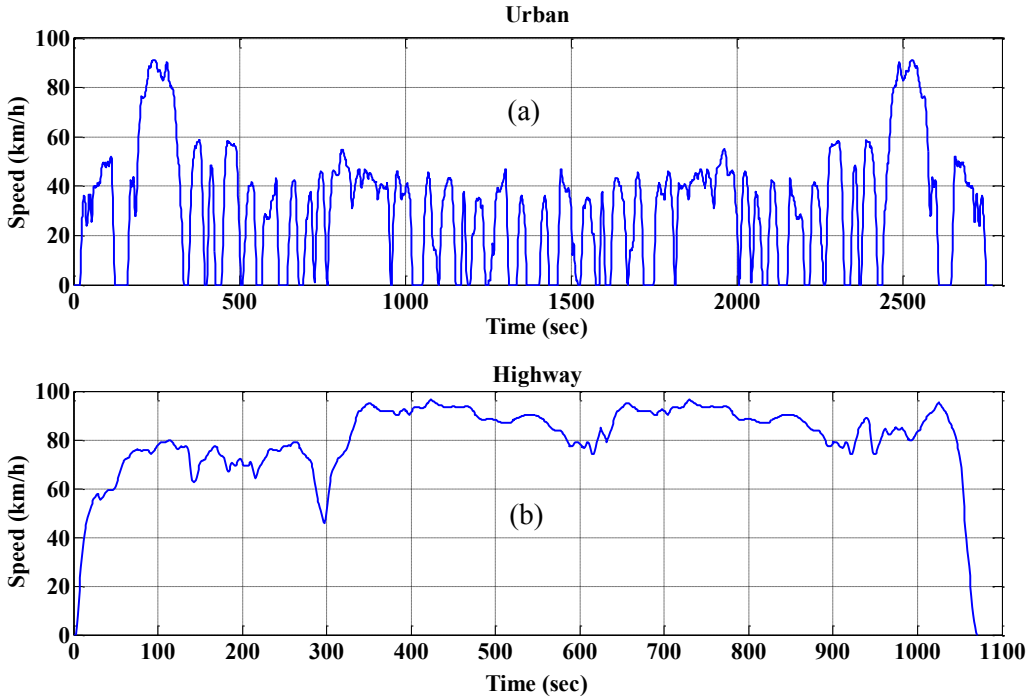


Figure 3.6: Simulation drive cycles: (a) urban and (b) highway

The battery capacity was chosen to be the same as that of Nissan Leaf, i.e., 24 kWh. The size of the SC pack was chosen according to the guidelines presented in [22]. A pessimistic and aggressive traction power demand scenario was considered to ensure SC pack operational compliance with the nominal traction demand. The pessimistic scenario assumes that the EV accelerates from 0 to 60 km/h, climbing a hill 30 m high. The traction energy required by the EV excluding losses is the sum of the kinetic energy of EV at 60 km/h and its potential energy at the top of the hill. It is appropriate to assume that the battery will supply the system losses. Taking Nissan Leaf as the sample EV, and assuming that the weights of the driver and additional HESS components are roughly 80 kg and 360 kg (260 kg for the battery pack and 100 kg for the SC pack and DC/DC converter), respectively, the sum of the EV's kinetic and potential energies is 194.6 Wh. Consequently, the SC pack capacity would be sized so that it can store 194.6 Wh at its maximum voltage.

The battery pack dimensions were chosen to meet the pack total voltage and energy specifications. The voltage specification is associated with the acceleration performance, which is governed by the desired τ_{max} and ω_{base} of traction motor system. The DC bus voltage must be sufficiently high to support the desired τ_{max} and ω_{base}. For the desired τ_{max}=370 N.m and ω_{base}=534 rad/s, the DC bus voltage was set to 363 V. Consequently, the number of series battery cells in a string and parallel strings in the pack for both

topologies are 110 and 30, respectively. This battery pack dimensions are used in both SC-DC and Bat-DC topologies. This means that, for Bat-DC topology, the DC bus voltage could be higher than 363 V, as the battery is connected at the low voltage side and SC at the DC bus. The SC voltage will normally be boosted by the battery. The reason for dimensioning the battery pack to have a high voltage in Bat-DC topology is that in some situations, the SC voltage level could drop to that of the battery. Consequently, the battery voltage will be clamped to that of the DC bus; thus, the battery voltage must be sufficiently high to meet the acceleration performance requirement.

The total number of SC cells in the pack must be chosen such that the total energy capacity of the SC pack matches the specified value mentioned above, which was 194.6 Wh. The energy capacity of a single SC cell can be calculated by (2-23). Consequently, the required total number of SC cells to meet the energy specification is found to be 641. However, this number will be increased to 660 to allow for higher SC pack dimensioning versatility, as the number of possible pack dimensions increases significantly for 660 compared to 641.

To determine the dimensions of the SC pack for both SC-DC and Bat-DC topologies, an iterative process is followed. For SC-DC topology, the nominal DC bus voltage that is set by the battery is 363 V. The low-side voltage of the DC/DC converter must be lower than the DC bus voltage and higher than the minimum value that is restricted by the duty cycle. If a 10% duty cycle is assumed as a lower limit, then the minimum low-side voltage would be about 50 V, as per equations (2-59) and (2-67). Subsequently, Table 3-8 summarizes the possible dimensions of the SC pack in the SC-DC topology. Dimension no. 9 will be omitted, as the SC only has a maximum of 5 V voltage excursion. Similarly, the possible dimensions of the SC pack on the DC bus for Bat-DC topology are summarized in Table 3-9. Dimension no. 1 will be omitted because the SC pack maximum voltage is too high for EV applications. At such high DC bus voltage, the traction inverter modulation index will be very low at low speeds. The modulation index may get saturated at the minimum value, which would impact operation. Also, the traction inverter switching losses will be high, as they are proportional to the DC bus voltage [56].

Table 3-8: Possible dimensions of SC pack for SC-DC topology

Dimension no.	Maximum pack voltage (V)	Number of series cells (n_{sc})	Number of parallel strings (m_{sc})
1	330.0	132	5
2	275.0	110	6
3	165.0	66	10
4	150.0	60	11
5	137.5	55	12
6	110.0	44	15
7	82.5	33	20
8	75.0	30	22
9	55.0	22	30

Table 3-9: Possible dimensions of SC pack for Bat-DC topology

Dimension no.	Maximum pack voltage (V)	Number of series cells (n_{sc})	Number of parallel strings (m_{sc})
1	825	330	2
2	550	220	3
3	412.5	165	4

The urban drive cycle simulation was performed with different SC pack dimensions for both SC-DC and Bat-DC topologies. Accordingly, the battery capacity fading after a single drive cycle was calculated and the results are given in Figure 3.7 for both HESS topologies. For SC-DC topology, the least capacity fading occurs for the SC pack dimensions of n_{sc}=110 and m_{sc}=6. Similarly, for the Bat-DC topology, the least capacity fading occurs for the SC pack dimensions of n_{sc}=220 and m_{sc}=3. Consequently, these dimensions will be used in the processing analysis as they yield the least battery capacity fading for both HESS topologies.

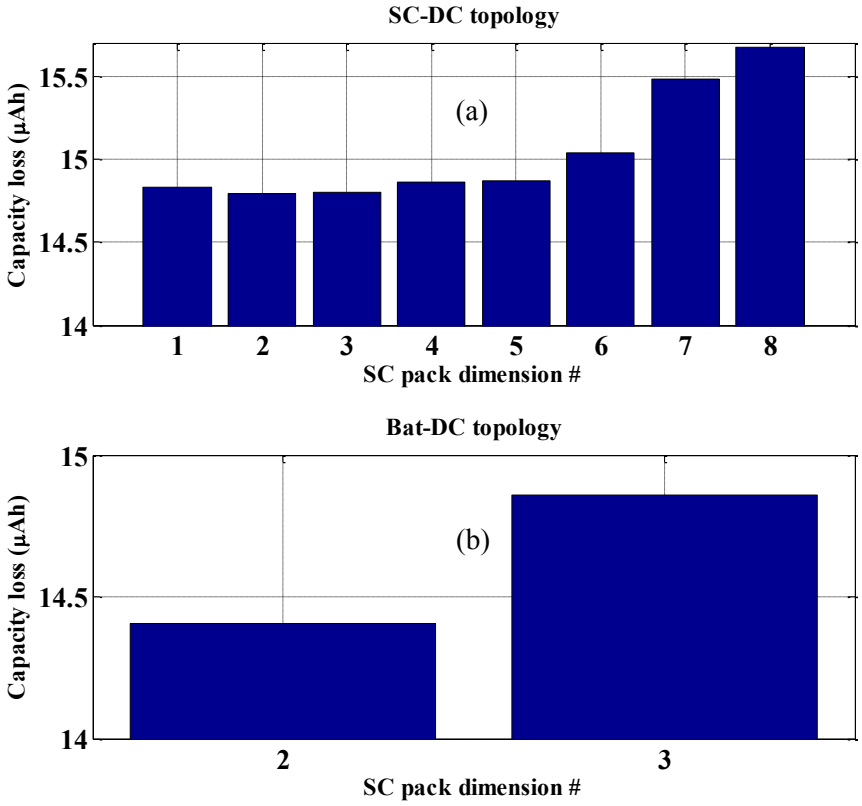


Figure 3.7: Battery capacity loss after a single urban drive cycle with different SC pack dimensions: (a) SC-DC topology and (b) Bat-DC topology

Consequently, both urban and highway drive cycles were simulated for SC-DC HESS, Bat-DC HESS, and battery-only ESS. The following assumptions were used in conducting the simulation for all case studies, unless otherwise stated:

- At the end of the drive cycle, the battery is recharged to 90% SoC at a C-rate of $0.23 \times m_b$ for the next drive cycle (the battery manufacturer recommends a charging C-rate of 0.23 per cell).
- Driver weight is 80 kg.
- 1 kW auxiliary load is added across the battery.

Figure 3.8 shows battery SoC, SC voltage, and DC/DC converter low-side current for SC-DC and Bat-DC topologies in both urban and highway drive cycles. For SC-DC topology, the SC voltage trajectory resulting from the optimal energy management looks similar to the battery SoC trajectory in charge depletion mode in HEV applications. However, for Bat-DC topology, the optimal energy management seeks to bypass the DC/DC converter and clamp the battery voltage to the DC bus. The energy management

issues a DC/DC converter low-side current set-points that are almost equal to zero over the entire drive cycle. Also, in some time periods, the energy management commands the DC/DC converter to draw power from the SC at the DC bus and feed the auxiliary load on the low-side. The reason for bypassing the DC/DC converter is to avoid supplying its losses, which would incur higher Ah_{proc} for the battery.

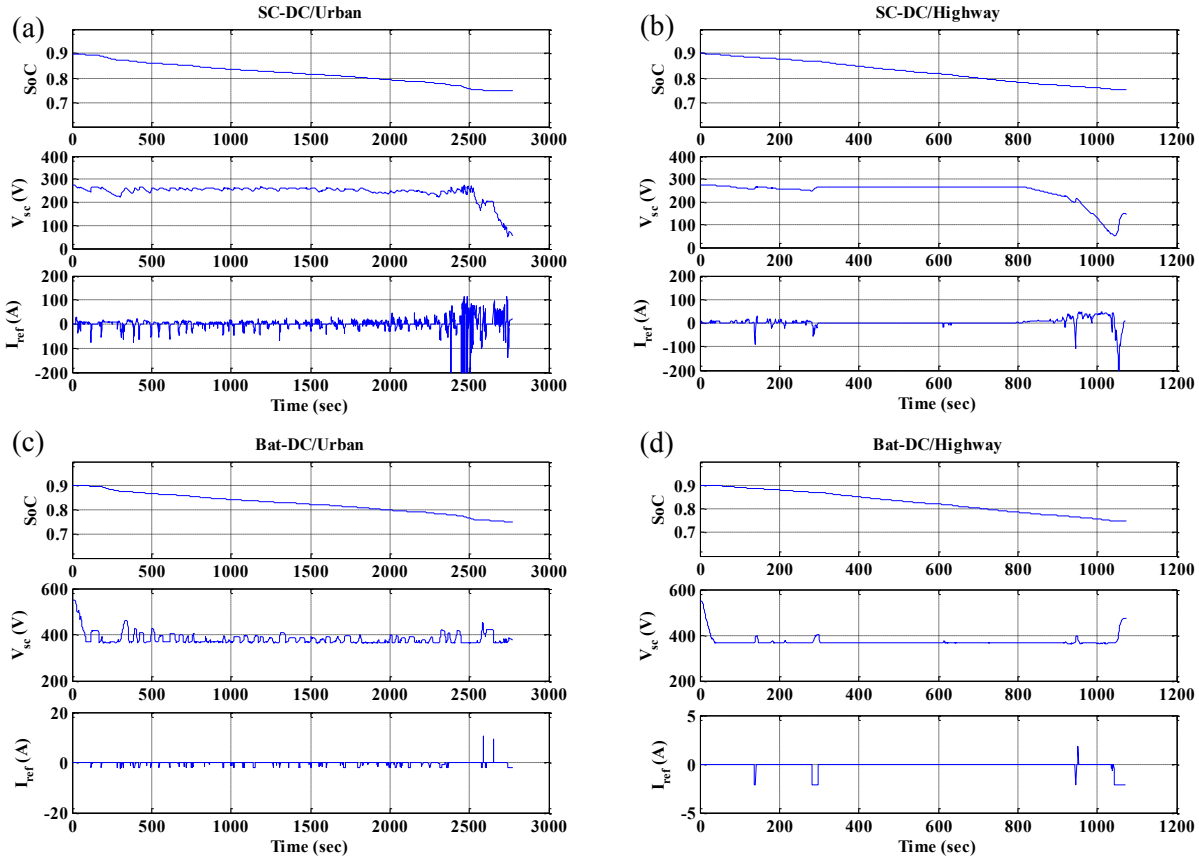


Figure 3.8: System states and control trajectories with 100% initial SC SoC for (a) SC-DC topology in urban driving, (b) SC-DC topology in highway driving, (c) Bat-DC topology in urban driving, (d) Bat-DC topology in highway driving

Figure 3.9 shows the normalized battery capacity versus the number of drive cycles for SC-DC HESS, Bat-DC HESS, and battery-only ESS. In the urban drive cycle, the battery in Bat-DC topology experiences the least capacity fading, followed by the battery in SC-DC and battery-only topologies in ascending order. From simulations, it was observed that the battery in the SC-DC topology processed more Ah compared to the battery in Bat-DC topology. The SC is meant to process regenerative braking energy and use that energy at a later time. In SC-DC topology, the regenerative braking energy supplies the DC/DC converter losses,

whereas in Bat-DC topology, the regenerative braking energy is captured directly by the SC at the DC bus. The difference between the regenerative braking energy values captured by the SCs in the two HESS topologies is supplied by the battery, which would incur more Ah processed. Also, the mass of the DC/DC converter in SC-DC topology is higher than that in Bat-DC topology. The additional mass increases the traction demand; thus, more Ah is drawn from the battery.

In the highway drive cycle, the battery capacity fading rates for both SC-DC and Bat-DC are almost the same. This is due to the fact that the magnitude and occurrence of regenerative braking energy in highway drive cycles is low. Consequently, the SC is mostly assisting the battery by supplying its initial stored energy.

The battery end-of-life (EoL) is assumed to be reached if the battery capacity has degraded to 80% of its rated value [9], [38]. Consequently, from battery capacity fading plots in Figure 3.9, the battery lifetime can be estimated as a number of drive cycles. It was demonstrated in [9] that the slopes of the battery normalized capacity curves do not change as the number of drive cycles increases; thus, it is not necessary to run the drive cycle simulation for many times until the battery reaches EoL. Consequently, the normalized battery capacity curves in Figure 3.9 can be linearly extrapolated until 80% is reached on the y-axis. The battery lifetime results are summarized in Table 3-10. For the highway drive cycle, the battery lifetime extension due to HESS is minimal, which is about 4.4% for both topologies. However, for the urban drive cycle, the battery lifetime extension is significant, especially for Bat-DC topology, whereby the battery lifetime is extended by about 18%.

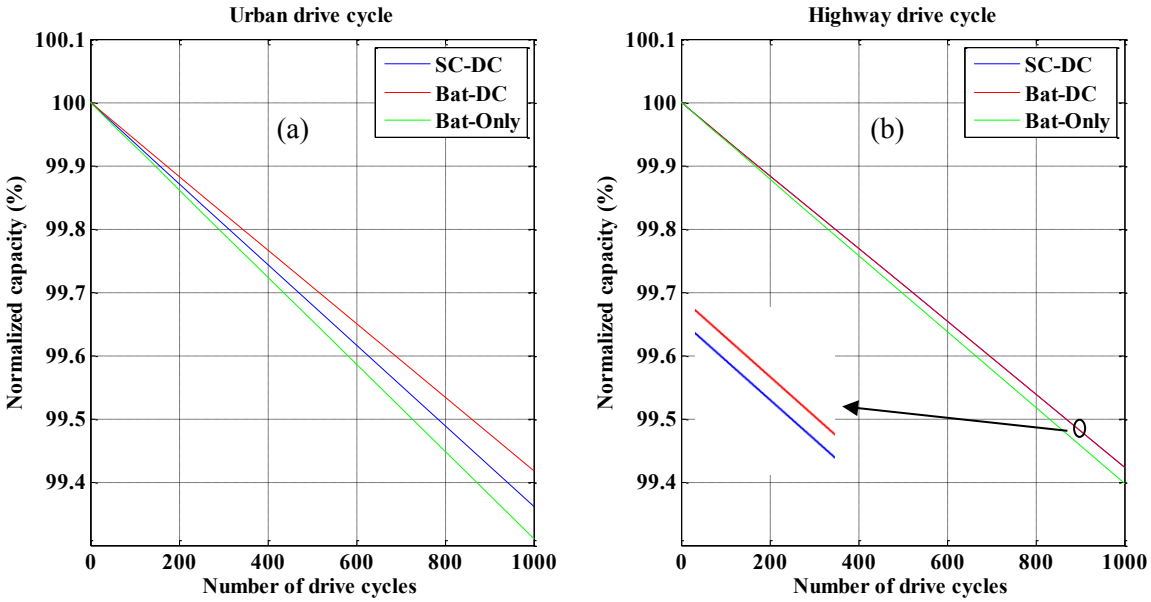


Figure 3.9: Battery normalized capacity versus number of drive cycles with 100% initial SC SoC for (a) urban drive cycle and (b) highway drive cycle

Table 3-10: Battery pack lifetime in terms of number drive cycles with 100% initial SC SoC

		Battery lifetime (no. of drive cycles)	Battery lifetime extension (%)
Urban drive cycle	Battery-only	29,010	-------
	SC-DC	31,338	8.02
	Bat-DC	34,300	18.24
Highway drive cycle	Battery-only	33,162	-------
	SC-DC	34,631	4.43
	Bat-DC	34,644	4.47

One caveat in the previous simulation results is that the SC voltage was set to the maximum value at the beginning of the simulation. It is worth investigating how the simulation results may change if the SC initial voltage is set to its minimum value. In Bat-DC topology, the initial SC voltage was set to 369, which is the same as the battery open circuit voltage. The SC voltage cannot be lower than the battery voltage in Bat-

DC topology. To conduct a meaningful comparison, the initial SC voltage in SC-DC topology must be set to a value such that its SC initial stored energy would the same as that of the SC in Bat-DC topology. The effective capacitance of the SC pack in Bat-DC topology is 4.77 F; thus, its stored energy at 369 V is 90.3 Wh. Accordingly, the initial SC pack voltage in SC-DC topology must be 184.5 V in order to have the same initial stored energy as that of the SC pack in Bat-DC topology. Consequently, the simulation results are shown in Figure 3.10 and Figure 3.11.

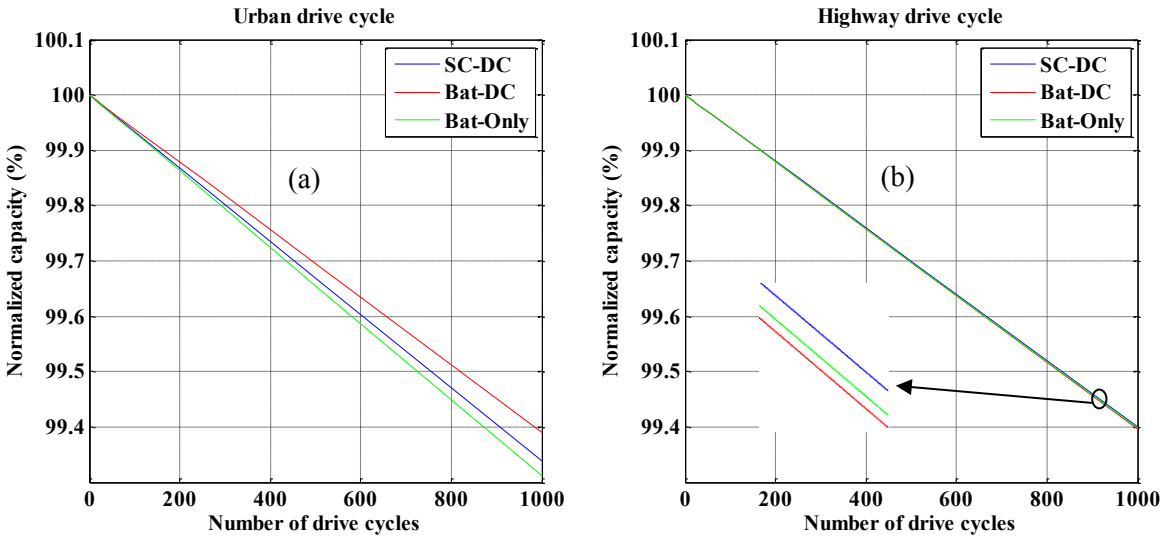


Figure 3.10: Normalized battery capacity versus number of drive cycles with 45% SC initial SoC for (a) urban drive cycle and (b) highway drive cycle

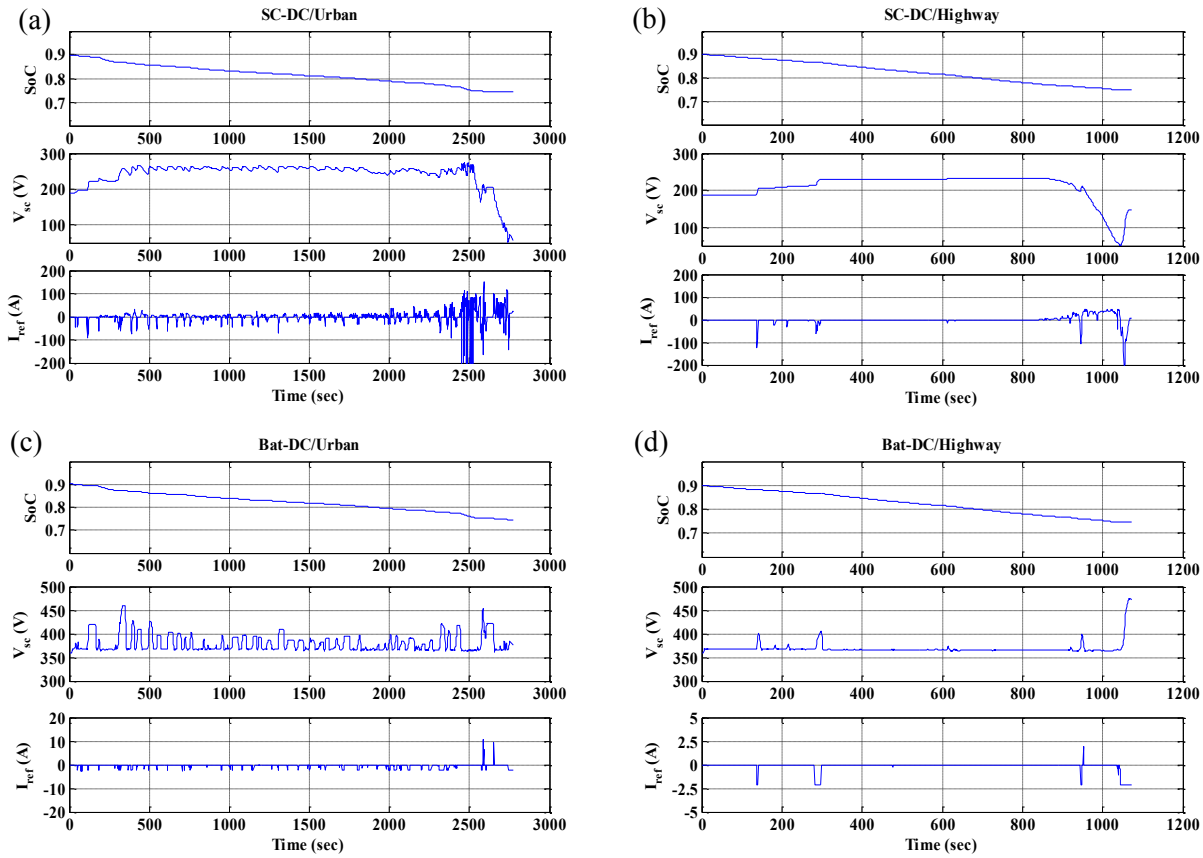


Figure 3.11: System states and control trajectories with 45% SC initial SoC for (a) SC-DC topology in urban driving, (b) SC-DC topology in highway driving, (c) Bat-DC topology in urban driving, (d) Bat-DC topology in highway driving

In the highway drive cycle, battery capacity fading for all three systems is almost the same. But, analytically, battery capacity loss in Bat-DC topology was slightly higher than that in battery-only ESS. This is due to the fact that the magnitude and occurrence of regenerative braking are low in the highway drive cycle; thus, the SC is not serving its purpose of processing regenerative braking energy. Also, the weight of the SC and DC/DC converter increase the weight the vehicle and traction power demand. This explains why the battery capacity loss is slightly higher for Bat-DC topology. On the other hand, the reason why the battery capacity loss is analytically lower in SC-DC HESS than in battery-only ESS is that all of the SC initial stored energy was fully extracted. But, in Bat-DC topology, the SC energy could not be extracted as the SC voltage was clamped to that of the battery.

For the urban drive cycle, the battery capacity fading results are similar to what was observed in the previous simulation with 100% initial SC SoC. But, the battery capacity fading rates for SC-DC and Bat-DC topologies are higher compared to those in the simulation results with 100% initial SC SoC. This is mainly due to the reduction in the SC initial stored energy. Subsequently, the battery lifetime results for all three topologies are summarized in Table 3-11.

Table 3-11: Battery pack lifetime in terms of number drive cycle with 45% initial SC SoC

		Battery lifetime (no. of drive cycles)	Battery lifetime extension (%)
Urban drive cycle	Battery-only	29,010	-------
	SC-DC	30,213	4.15
	Bat-DC	32,831	13.17
Highway drive cycle	Battery-only	33,162	-------
	SC-DC	33,260	0.30
	Bat-DC	33,147	-0.05

The optimal energy management for Bat-DC topology is similar to what was observed in the previous simulation with 100% initial SC SoC. The energy management seeks to bypass the converter and clamp the battery voltage to the DC bus. Similarly, for SC-DC topology, the optimal energy management follows the charge depletion mode of operation. However, near the begging of the drive cycle, the energy management seeks to charge the SC via regenerative braking to increase its voltage to operate the DC/DC converter in the high-efficiency region.

3.4 Case study 2: effect of restricting final SC SoC

SC must be used as a power buffer rather than a power supply. Consequently, the net energy expenditure by the SC over the drive cycle must be zero. Thus, the final SC voltage at the end of the drive cycle will be restricted to be equal to its initial voltage when solving for the optimal energy management. In this case study, the initial SC voltage will be set to the maximum value. A more realistic and meaningful choice for the initial SC voltage is its minimum value, as the SC will most probably be discharged at the start of most trips. The issue with this choice is that it is implicitly assumed that the SC voltage in Bat-DC topology

cannot be lower than the battery voltage, as the SC is connected to the DC bus. Therefore, the initial SC voltage will be set to the maximum value. Subsequently, the simulation results are shown in Figure 3.12 and Figure 3.13.

The battery capacity fading in the urban drive cycle is similar to what was previously observed. For the highway drive cycle, the battery capacity fading for all three systems is very close. But, analytically, the battery capacity fading in SC-DC HESS is higher than that in battery-only ESS. The reason is that the SC is not supplying any net energy to the load over the drive cycle while adding weight to the vehicle. This additional weight increases the traction power demand. Although the SC is processing regenerative braking energy, it is not sufficient to reduce the battery capacity fading, as the magnitude and occurrence of regenerative braking energy are low in highway drive cycles.

The system states and control trajectories are similar to what was observed in the previous case study; except that at the end of the drive cycle, the battery charges the SC to 100% SoC.

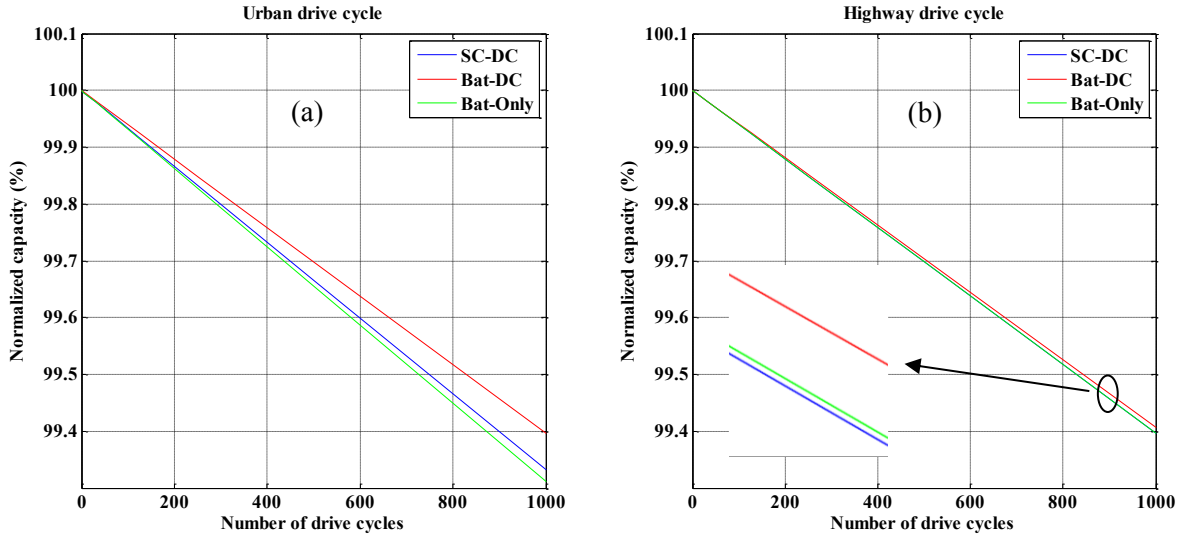


Figure 3.12: Normalized battery capacity versus number of drive cycles with 100% SC initial and final SoC for (a) urban drive cycle and (b) highway drive cycle

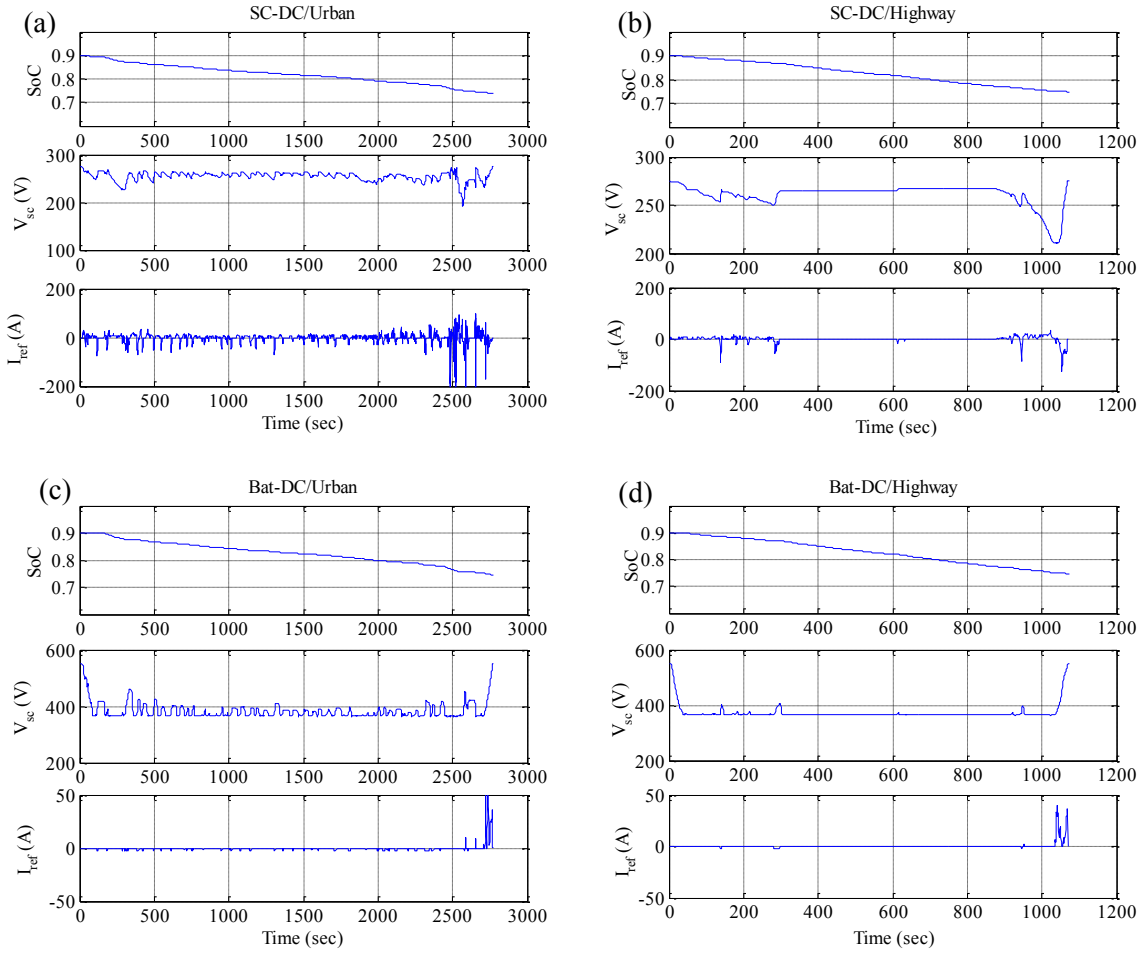


Figure 3.13: System states and control trajectories with 100% SC initial and final SoC for (a) SC-DC topology in urban driving, (b) SC-DC topology in highway driving, (c) Bat-DC topology in urban driving, (d) Bat-DC topology in highway driving

3.5 Case study 3: effect of realistic urban-highway hybrid drive cycle

In this case study, a realistic drive cycle is used to test the battery capacity fading. The drive cycle is shown in Figure 3.14. The drive cycle is divided into three sections. The first section resembles driving near a residential area. The second section resembles highway driving, and the third section resembles city driving. Further, the drive cycle is duplicated to emulate a round trip. The total driving distance of the drive cycle is about 68 km. Also, it was assumed that EV accommodates four passengers each weighing 80 kg. In addition, the SC initial SoC was set to 100%.

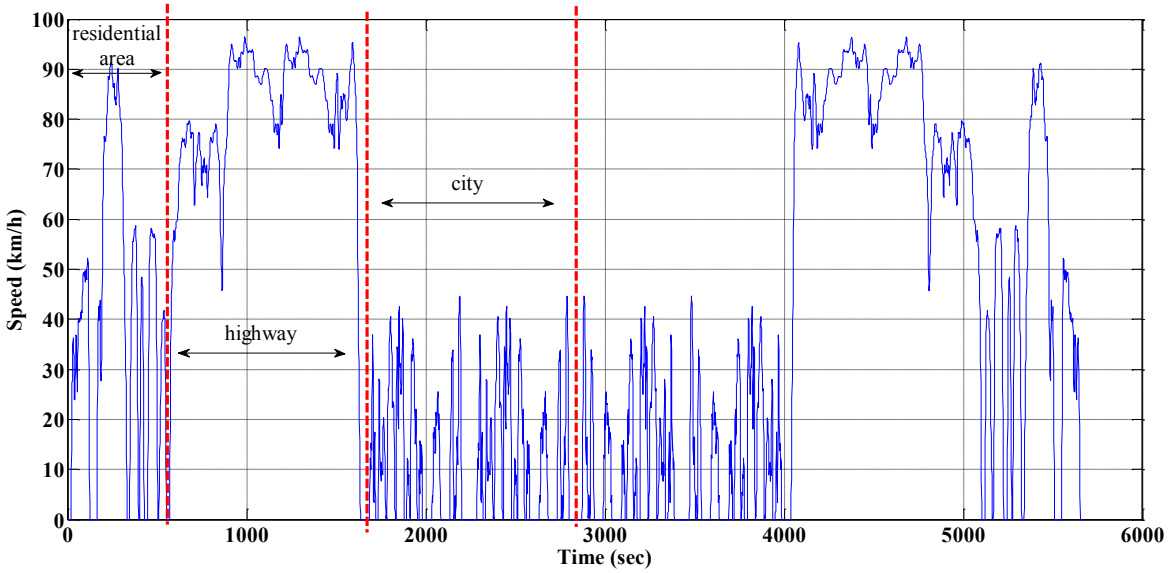


Figure 3.14: Realistic daily commute drive cycle

The battery capacity fading results are shown in Figure 3.15. The battery capacity fading rate is the highest in battery-only ESS, followed by SC-DC and Bat-DC HESSs, in descending order. Consequently, the battery lifetime was estimated from Figure 3.15, and the results are summarized in Table 3-12. The battery lifetime extension for both topologies is much lower compared to the results observed in case study no. 1 for the urban drive cycle, due to the highway driving portion.

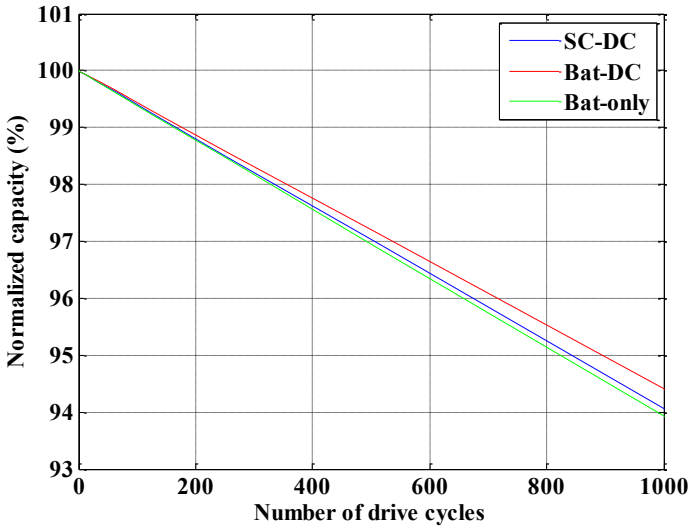


Figure 3.15: Normalized battery capacity versus number of drive cycles

Table 3-12: Battery lifetime as a number of drive cycles

Topology	Battery lifetime (no. of drive cycle)	Battery lifetime extension (%)
Battery-only	3,290	-------
SC-DC	3,369	2.4
Bat-DC	3,575	8.7

3.6 Case study 4: effect of increasing the battery pack size in battery-only ESS for extending the battery lifetime

In order to hybridize the battery-only ESS with SC, the battery pack size must be reduced to accommodate the volumes and weights of the SC pack and DC/DC converter. In the previous case studies, the battery pack size for both HESS topologies and battery-only ESS was the same. Thus, to further refine the comparison, the battery pack in battery-only ESS will be expanded by adding more battery strings in parallel. The monetary value of these additional battery strings will be equal to the total monetary value of the SC pack and DC/DC converter of HESS. The costs of SC and battery cells are $7.3 and 7.0, respectively [57], [58]. The cost per kilowatt ($/kW) of commercial DC/DC converters will be taken as $200/kW. Consequently, the total cost of the SC and DC/DC converter in SC-DC and Bat-DC topologies are $12,818 and $6,818, respectively. These monetary values are roughly equivalent to 16 and 8 battery strings, respectively.

As a result, SC-DC HESS will be compared with a battery-only ESS that has battery pack dimensions of n_b=110 and m_b=46. Similarly, Bat-DC HESS will be compared with a battery-only ESS that has battery pack dimensions of n_b=110 and m_b=38. For the urban-highway hybrid drive cycle, the battery capacity fading simulation results are shown in Figure 3.16. These results show that by simply increasing the battery pack size, battery lifetime in battery-only ESS will increase significantly compared to that in either HESS topologies. This is due to the fact that in a larger battery pack, the processed Ah and DoD of the individual battery cell are lower.

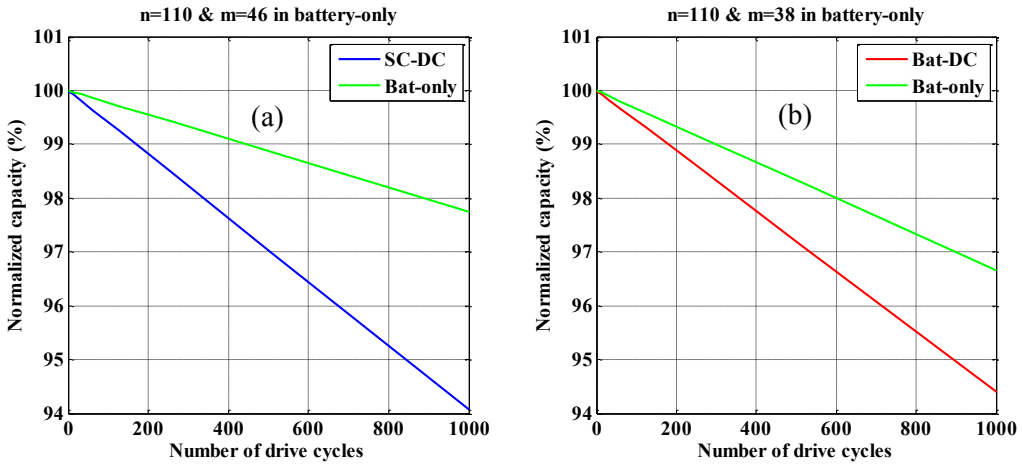


Figure 3.16: Normalized battery capacity fading with expanded battery pack in battery-only ESS (a) n_b=110, m_b=46 and (b) n_b=110, m_b=38

3.7 Summary

In this chapter, the battery capacity fading analysis was conducted via simulation. Using dynamic programming, the optimal energy management that minimizes battery capacity loss is determined for each HESS topology and drive cycle to ensure unbiased comparisons of the HESS topologies. HESS was most effective for urban drive cycles. For the sample EV (Nissan Leaf), it was demonstrated that the battery lifetime would be extended by 18.24 and 8.02% for Bat-DC and SC-DC topologies, respectively, in typical urban drive cycles. But for typical highway drive cycles, the battery lifetime would be extended by only 4.47 and 4.43 % for Bat-DC and SC-DC topologies, respectively. Further, for a realistic hybrid drive cycle that exhibits both highway and urban driving, the battery lifetime extension was 8.7 and 2.4% for Bat-DC and SC-DC topologies, respectively. Consequently, for all simulation case studies, Bat-DC was superior to SC-DC in extending the battery lifetime.

From simulations, it was observed that in Bat-DC topology, the DC/DC converter is normally bypassed as a result of the optimal energy management. Consequently, this may imply that the passive HESS with a diode connecting the battery to the DC bus is a superior solution to Bat-DC topology, as it calls for no DC/DC converter while yielding a battery capacity loss similar to that in Bat-DC topology. However, in situations where there is excessive regenerative braking, e.g., during a downhill drive, the SC voltage may exceed its rated value. Thus, the DC/DC converter is needed to draw power from the DC bus and feed the battery and auxiliary load to lower the DC bus voltage. This operation cannot be realized by the modified passive HESS topology that uses a diode to connect the battery to the DC bus.

Further, in regards to the operation performance of both HESS topologies, authors in [10], [24], [26], [27], [59], [60] have deduced that Bat-DC is superior to SC-DC. As a result, it can be concluded that Bat-DC is the superior topology in regards to both operational performance and battery capacity fading.

In the last case study, a comparison was conducted in which the number of battery cells of the pack in battery-only ESS was increased. The monetary value of the additional battery cells was equal to the total monetary value of the SC pack and DC/DC converter of HESS. It was observed that in the urban-highway hybrid drive cycle, the battery-only ESS with expanded battery pack was superior to both HESS topologies in extending the battery lifetime. However, in the next chapter, it will be demonstrated how Bat-DC HESS with an integrated onboard charger scheme will be a cheaper solution in extending the battery lifetime than expanding the battery for urban drive cycles.

The core material of this chapter has appeared in the published conference paper [61].

Chapter 4
Integrated Charger

In North America, the Society of Automotive Engineers (SAE) has categorized the rated power for EV battery charging into three groups, namely, Level-1, Level-2, and Level-3. Table 4-1 summarizes the specifications of these charging levels. Normally, all EVs are equipped with an onboard Level-1 charger. This charging level uses the regular 120 V electrical outlet in houses. The shortcoming of Level-1 charging is the long charging time. For example, it would take about 17 hours to fully charge Nissan Leaf's 24 kWh battery from 0% initial SoC. Consequently, EV makers offer another onboard charger option, i.e., Level-2 charging. Nissan provides the option of a 6.6 kW onboard charger, which could fully charge the battery in about 3.5 hours from 0% initial SoC. Level-2 charging requires 208 or 240 V electrical outlets.

Level-3 charging can only take place at charging stations. At 50 kW charging power, Nissan Leaf's battery can be fully charged in about half an hour. However, using Level-3 charging requires the owner to go to the charging station, which might cause inconvenience. Thus, Level-2 charging strikes a good balance between charging time and convenience.

Table 4-1: Specifications of charging levels [62]

	Leve-1	Level-2	Level-3
Voltage (V)	120	208 or 240	200 to 450
Current type	AC	AC	DC
Nominal power (kW)	1.4 kW	7.2 kW	50 kW
Maximum power (kW)	1.9 kW	19.2 kW	150 kW

The two stage converter topology is the most promising topology for onboard battery chargers [63]. An AC/DC converter is used to generate and regulate the DC bus voltage as well as perform the power factor correction function to draw power at unity power factor from the utility grid. Further, a DC/DC converter draws power from the DC bus and supplies a well-regulated current to the battery. Figure 4.1 depicts the circuit-level structure of a two-stage onboard battery charger [63]. The charger topology is composed of AC/DC full-bridge converter and DC/DC half-bridge converter.

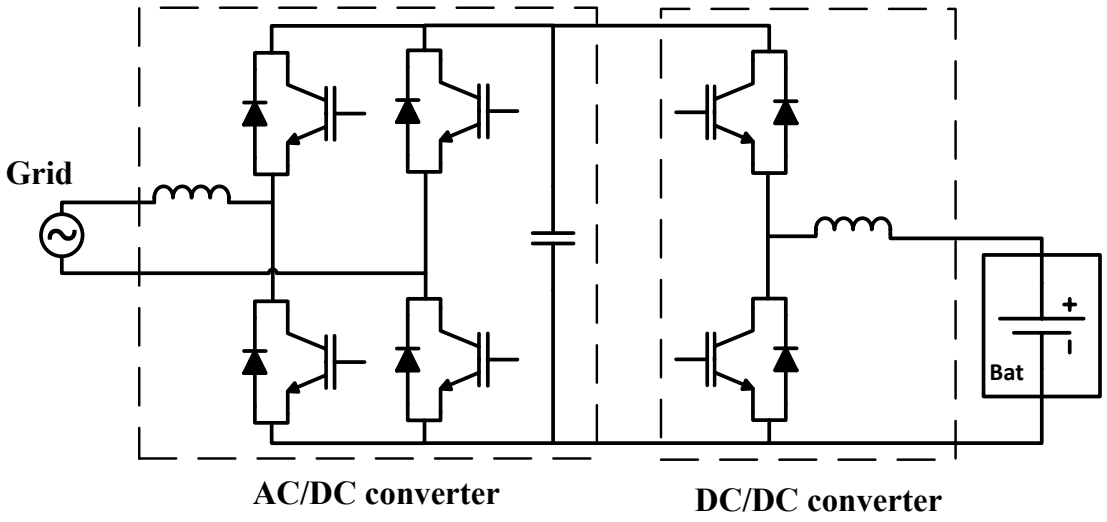


Figure 4.1: Two-stage onboard battery charger topology

Figure 4.2 shows the connection of onboard charger with the battery in the EV. Two single-pole-double-throw (SPDT) switches are used to bypass the onboard charger when Level-3 charging is used. The SPDT switches are connected to position 1 when using the onboard charger (Level-1 and Level-2 charging) and connected to position 2 when using Level-3 charging at charging stations.

The onboard charger topology of Figure 4.1 can be realized by the existing converter in Bat-DC HESS and the traction inverter of the EV. The charger DC/DC converter is the same as the DC/DC converter in Bat-DC HESS. Further, the full-bridge active rectifier can be realized from two legs of the traction inverter. As a result, the onboard charger can be integrated into the EV electric powertrain that is equipped with HESS. In order to realize this system, a second pair of SPDT switches must be installed between the traction inverter and motor as shown in Figure 4.3. SPDT switches in the green color are normally connected to the default position, *d*, which connects the traction inverter to the motor. For Level-1 or 2 charging using the onboard charger, all SPDT switches are connected to position 1. Further, for Level-3 charging, SPDT switches in red color are connected to position 2. Consequently, with the integrated charger scheme, the active rectifier in the original onboard charger can be eliminated, which results in a significant cost reduction. Further, two SPDT contactors must be added to the system between the traction inverter and motor. However, the cost of the contactors is much lower than the cost of the active rectifier.

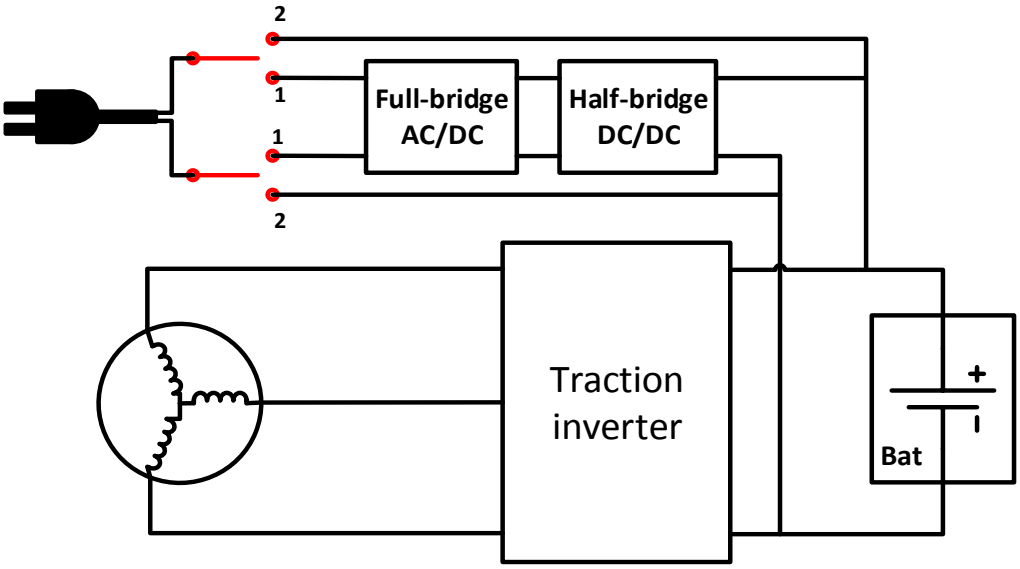


Figure 4.2: Connection diagram of EV onboard charger

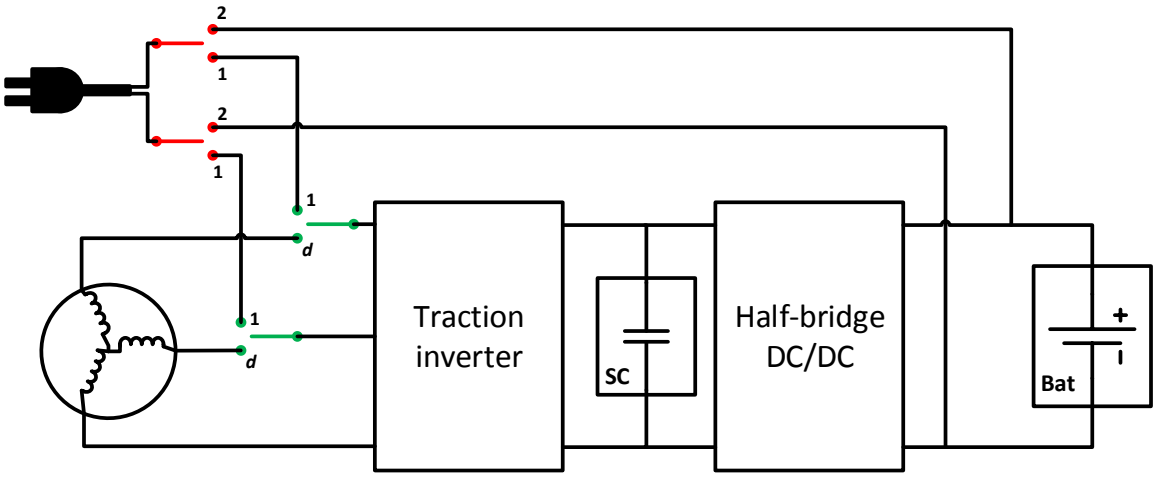


Figure 4.3: Connection diagram of EV onboard integrated charger with Bat-DC HESS topology

Therefore, for extending the battery lifetime, it might be less expensive to install a HESS instead of expanding the battery pack, as the cost of the active rectifier is saved. In the previous chapter, the number of cells in the battery and SC packs were 3,300 and 660, respectively. Also, assume the rating of the DC/DC converter in Bat-DC HESS is 6.6 kW (note that from simulations in Chapter 3, a 6.6 kW rating for the DC/DC converter would be sufficient for propulsion), which is the same as Nissan Leaf's onboard Level-2

charger. Thus, the net cost of HESS installation would be the cost of SC pack plus the cost of 2 SPDT contactors minus the cost the active rectifier of the base onboard charger. Recall, the cost the SC cell was $7.3. In addition, the cost of a single SPDT contactor is taken to be $50. Similarly, the cost per power rating for active rectifiers is taken to be $300/kW [64], [65]. Consequently, the net cost of the HESS, excluding the battery pack, is $2,938. This is equivalent to 420 battery cells. The original battery pack had 3,300 cells with dimensions of n_b=110 and m_b=30. Subsequently, the total available number of battery cells has increased to 3,720 for the battery-only ESS. The dimension of the larger battery pack needs to be readjusted to accommodate the higher number of battery cells available. The number of series battery cells in a string must respect the DC bus voltage constraint that is set according to the desired acceleration performance. The nominal DC bus voltage must be greater than 363 V. Consequently, the new dimension of the battery pack in battery-only ESS is n_b=120 and m_b=31.

Subsequently, the drive cycle simulation will be conducted to test the battery capacity fading for the battery-only ESS with a larger battery pack and Bat-DC HESS with the intergraded charger scheme. All three drive cycles presented in the previous chapter will be used in the simulation. These include urban, highway, and urban-highway hybrid drive cycle, shown in Figure 3.6 (a), Figure 3.6 (b), and Figure 3.14, respectively. Figure 4.4 shows the battery capacity fading for all three drive cycles. For both highway and hybrid drive cycles, the battery capacity in Bat-DC HESS fades faster than that in battery-only ESS with expanded battery pack. However, for the urban drive cycle, the battery capacity in Bat-DC HESS fades more slowly than that in battery-only ESS with expanded battery pack. This indicates that the battery pack in Bat-DC HESS with integrated charger scheme will last longer than that in battery-only ESS, yet the costs of the two systems are the same. As a better interpretation of this comparison, one can say that by reducing the number of battery cells in the battery pack and adding an SC with integrated charger scheme that has the same monetary value as saved battery cells, the EV's ESS will last longer. In fact, the battery lifetime extension was estimated from Figure 4.4 (a) to be about 4%.

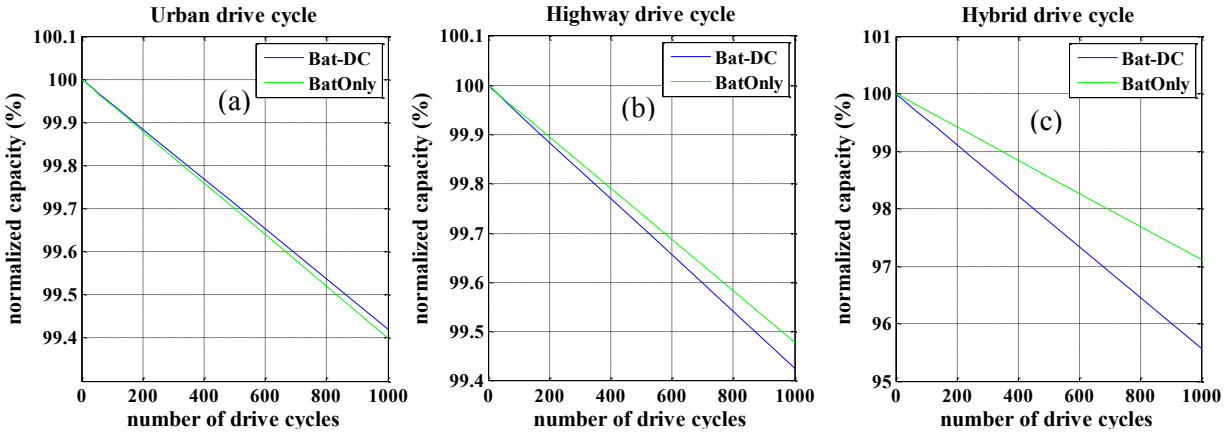


Figure 4.4: Battery normalized capacity versus number of drive cycles for (a) urban drive cycle, (b) highway drive cycle, and (c) hybrid drive cycle

Table 4-2: Battery lifetime as a number of drive cycles

		Battery lifetime (no. of drive cycles)	Battery lifetime extension (%)
Urban drive cycle	Battery-only	33,194	-------
	Bat-DC	34,459	3.8
Highway drive cycle	Battery-only	38,254	-------
	Bat-DC	34,760	-9.1
Hybrid drive cycle	Battery-only	6,911	-------
	Bat-DC	4,513	-35

Chapter 5
Conclusion

5.1 Summary

In Chapter 1, it was discussed that the common battery-only ESS exhibits accelerated capacity fading due to the aggressive traction power demand, which exhibits both high power fluctuations and regenerative braking. Consequently, battery-supercapacitor HESS was proposed to use the SC to buffer the high-frequency component of power demand and process regenerative braking power. A literature review was then presented that discussed possible HESS topologies through which the SC and battery are interfaced with the DC bus. Two partially-decoupled topologies have proved to be the most promising solutions, as they use a single DC/DC converter that could support any energy management that is supported by the fully-decoupled topology. In the first topology, which was abbreviated as SC-DC, the battery is connected to the DC bus, and the SC is connected to the DC bus through the DC/DC converter. In the second topology, which was abbreviated as Bat-DC, the SC is connected to the DC bus, and the battery is connected to the DC bus through a DC/DC converter with a bypass diode.

In Chapter 2, the background knowledge necessary to conduct the analysis and study of the research was presented. First, the EV powertrain power model was covered, which consisted of vehicle longitudinal dynamics, transmission, motor drive system, and HESS. Next, dynamic programming, a mathematical technique used for solving optimal control problem of dynamical systems, was described.

In Chapter 3, the performance of HESS was studied through simulations. HESS was used to drive the EV through a drive cycle, and accordingly the battery capacity loss was computed. Various case studies were performed. It was observed that HESS was most effective in urban drive cycles rather than highway drive cycles. In urban drive cycles, the lifetime extensions of the battery pack in Bat-DC HESS and SC-DC HESS compared to that in the battery-only ESS were 18 and 8%, respectively. Further, another case study was conducted in which the battery pack in the battery-only ESS was extended. The monetary value of the battery pack extension was equal to the total monetary value of the SC pack and DC/DC converter. It was observed that by extending the battery pack in battery-only ESS instead of using HESS, the battery pack would incur a higher lifetime extension.

In Chapter 4, an integrated charger scheme was presented whereby the traction inverter and HESS DC/DC converter were used to form the onboard battery charger. Also, two SPDT switches had to be added to the system to connect the traction inverter to either the motor or onboard charger outlet. In the integrated

charger scheme, the active rectifier in the original onboard charger is eliminated, which incurs significant monetary savings. It was observed, for urban drive cycles only, that the battery lifetime was extended by 4% in Bat-DC HESS with integrated charger compared to that in battery-only ESS with extended battery pack. The monetary value of battery pack extension in battery-only ESS is equal to the cost of the SC minus the cost of the original active rectifier.

5.2 Contributions

The main contributions of this research are two folds:

- **A simulation platform quantifying the battery lifetime**

  The platform was built in Matlab and Simulink. The drive cycle and vehicle parameters are the inputs to the platform, and the battery lifetime and optimal energy management of HESS are the outputs. Based on this platform, a conference paper has been published [61].

- **An integrated onboard charger scheme**

  The proposed charger scheme eliminates the active rectifier in the original onboard charger and utilizes the traction inverter and HESS DC/DC converter to realize the onboard charger.

5.3 Future Work

A meaningful continuation of this work is to quantify the battery capacity fading experimentally rather than using empirical capacity fading models. Building a full-scale HESS is expensive; thus, down-scaling of the HESS is necessary. Although the battery and SC packs can be scaled down proportionally, this is not the case for the power losses in the DC/DC converter. In the full-scale HESS, the DC/DC converter will operate in the high-efficiency region of its efficiency map. However, in the scaled-down HESS, the DC/DC converter might be operated in the low-efficiency region of its efficiency map, due to the low voltage levels in the scaled-down version of HESS. However, with appropriate design of the DC/DC converter, the scaled-down DC/DC converter can also be operated in the high-efficiency region. However, designing such DC/DC converter is difficult. Consequently, another approach to emulate a scaled-down version of HESS is to cycle a single battery cell with a current that is cycled by a single battery string in the EV drive cycle simulation. Using this method, the laboratory testbed is much cheaper and easier to operate. Also, the implication with the un-proportional scaling of the DC/DC converter efficiency is avoided.

Another meaningful continuation of this work is optimal sizing of the battery and SC packs in Bat-DC topology while considering the battery capacity fading.

Appendix A

Table A-1: Parameters of battery cell equivalent circuit [40]

R_s					
R_{s_0d}	R_{s_0c}	T_{refR_sd}	T_{refR_sc}	T_{shiftR_sd}	T_{shiftR_sc}
0.0048	0.0055	31.0494	22.2477	-15.3253	-11.5943
R_1					
R_{10_d}	R_{10_c}	R_{11_d}	R_{11_c}	R_{21_d}	R_{21_c}
7.1135×10^{-4}	0.0016	-4.3865×10^{-4}	-0.0032	2.3788×10^{-4}	0.0045
$T_{refR_{1d}}$	$T_{refR_{1c}}$	$T_{shiftR_{1d}}$	$T_{shiftR_{1c}}$		
347.4707	159.2819	-79.5816	-41.4548		
C_1					
C_{10_d}	C_{10_c}	C_{11_d}	C_{11_c}	C_{12_d}	C_{12_c}
335.4518	523.215	3.1712×10^{3}	6.4171×10^{3}	-1.3214×10^{3}	-7.5555×10^{3}
C_{13_d}	C_{13_c}	C_{14_d}	C_{14_c}	C_{15_d}	C_{1d_c}
53.2138	50.7107	-65.4786	-131.2298	44.3761	162.4688
R_2					
R_{20_d}	R_{20_c}	R_{21_d}	R_{21_c}	R_{22_d}	R_{22_c}
0.0288	0.0113	-0.073	-0.027	0.0605	0.0339
$T_{refR_{2d}}$	$T_{refR_{2c}}$				
16.6712	17.0224				
C_2					
C_{20_d}	C_{20_c}	C_{21_d}	C_{21_c}	C_{22_d}	C_{22_c}
3.1887×10^{4}	6.2449×10^{4}	-1.1593×10^{5}	-1.055×10^{5}	1.0493×10^{5}	4.4432×10^{4}
C_{23_d}	C_{23_c}	C_{24_d}	C_{24_c}	C_{25_d}	C_{2d_c}
60.3114	198.9753	1.0175×10^{4}	7.5612×10^{3}	-9.5924×10^{3}	-6.9365×10^{3}
V_{oc}					
a_1	a_2	a_3	a_4	a_5	a_6
-0.5863	21.90	3.414	0.1102	-0.1718	0.008

References

[1] "Source of Greenhouse Gas Emissions," EPA United States Protection Agency, 2016. [Online]. Available: https://www3.epa.gov/climatechange/ghgemissions/sources.html. [Accessed 25 April 2016].

[2] "2013 UK Greenhouse Gas Emissions, Final Figures," Department of Energy & Climate Change, London, UK, 2016, https://www.gov.uk/government/uploads/system/uploads/attachment_data/file/407432/20150203_2013_Final_Emissions_statistics.pdf. [Accessed June 2016].

[3] "Summary of GHG Emissions for France," United Nations Climate Change Secretariat, 2012, https://unfccc.int/files/ghg_emissions_data/application/pdf/fra_ghg_profile.pdf. [Accessed June 2016].

[4] M. Ehsani, T. Gao, S. E. Gay and A. Emadi, Modern Electric, Hybrid Electric, and Fuel Cell Vehicles Fundamentals, Theory, and Design, USA: CRC Press, 2005.

[5] "Canadian Environmental Sustainability Indicators Greenhouse Gas Emissions," Environment and Climate Change Canada, Gatineau, QC, Canada, 2016, https://www.ec.gc.ca/indicateurs-indicators/F60DB708-6243-4A71-896B-6C7FB5CC7D01/GHGEmissions_EN.pdf. [Accessed June 2016].

[6] "BC Air Quality," 2016. [Online]. Available: http://www.bcairquality.ca/topics/vehicle-pollutants.html. [Accessed 20 April 2016].

[7] "Alternative Fuels Data Center," U.S. Deparment of Energy, 2016. [Online]. Available: http://www.afdc.energy.gov/vehicles/electric_emissions.php. [Accessed 10 April 2016].

[8] "2016 Nissna Leaf," Nissan, 2016. [Online]. Available: http://www.nissanusa.com/electric-cars/leaf/. [Accessed 10 April 2016].

[9] L. Lam, "A Practical Circuit-based Model for State of Health Estimation of Li-ion Battery Cells in Electric Vehicles," in *Masters Thesis, Delft University of Technology*, Delft, Netherlands, 2011.

[10] J. Cao and A. Emadi, "A New Battery/UltraCapacitor Hybrid Energy Storage System for Electric, Hybrid, and Plug-In Hybrid Electric Vehicles," *IEEE Transaction on Power Electronics,* vol. 27, no. 1, pp. 122-132, 2012.

[11] N. Jinrui, W. Zhifu and R. Qinglian, "Simulation and Analysis of Performance of a Pure Electric Vehicle with a Super-capacitor," in *IEEE Vehicle Power Propulsion Conference*, Windsor, 2006.

[12] M. Ortuzar, J. Moreno and J. Dixon, "Ultracapacitor-Based Auxiliary Energy System for an Electric Vehicle: Implementation and Evaluation," *IEEE Transactions on Industrial Electronics,* vol. 54, no. 4, pp. 2147-2156, 2007.

[13] L. Shao, M. Moshirvaziri, C. Malherbe, A. Moshirvaziri, A. Eski, S. Dallas, F. Hurzook and O. Trescases, "Ultracapacitor/Battery Hybrid Energy Storage System with Real-Time Power-Mix Control Validated Experimentally in a Custom Electric Vehicle," in *IEEE Applied Power Electronics Conference and Exposition*, Charlotte, 2015.

[14] S. M. Lukic, J. Cao, R. C. Bansal, F. Rodriguez and A. Emadi, "Energy Storage Systems for Automotive Applications," *IEEE Transaction on Industrial Electronics,* vol. 55, no. 6, pp. 2258-2267, 2008.

[15] "Energy Storage Technologies," CAP-xx, 6 April 2016. [Online]. Available: http://www.cap-xx.com/resource/energy-storage-technologies/. [Accessed 1 June 2016].

[16] R. A. Dougal, S. Liu and R. E. White, "Power and Life Extension of Battery-Ultracapacitor Hybrids," *IEEE Transactions on Components and Packaging Technologies,* vol. 25, no. 1, pp. 120-131, 2002.

[17] L. Gao, R. A. Dougal and S. Liu, "Power Enhancement of an Actively Controlled Battery/Ultracapacitor Hybrid," *IEEE Transaction on Power Electronics,* vol. 20, no. 1, pp. 236-243, 2005.

[18] Z. Shuo, X. Rui and Z. Xuan, "Comparison of the Topologies for a Hybrid Energy-Storage System of Electric Vehicles via a Novel Optimization Method," *SCIENCE CHINA Technological Sciences,* vol. 58, no. 7, pp. 1173-1185, July 2015.

[19] R. Carter, A. Cruden and P. J. Hall, "Optimizing for Efficiency or Battery Life in a Battery/Supercapacitor Electric Vehicle," *IEEE Transaction on Vehicular Technology,* vol. 61, no. 4, pp. 1526-1533, 2012.

[20] J. Silvestre, "Half-bridge bidirectional DC-DC Converter for small Electric Vehicle," in *International Symposium on Power Electronics, Electric Drives, Automation and Motion*, Ischia, pp. 884-888, 2008.

[21] M.-E. Choi, J.-S. Lee and S.-W. Seo, "Real-Time Optimization for Power Management Systems of a Battery/Supercapacitor Hybrid Energy Storage System in Electric Vehicles," *IEEE Transactions on Vehicular Technology,* vol. 63, no. 8, pp. 3600-3611, 2014.

[22] M. E. Ortuzar, "Design, Implementation and Evaluation of an Auxiliary Energy System for Electric Vehicles, Based on Ultracapacitors and Buck-Boost Converter," in *PhD thesis, Pontifical Catholic University of Chile*, Chile, 2005.

[23] A. F. Burke, J. E. Hardin and E. J. Dowgiallo, "Application of Ultracapacitors in Electric Vehicle Propulsion Systems," in *Power Sources Symposium*, Cherry Hill, New Jersy, U.S., pp. 328-333, June 1990.

[24] J. Cao and A. Emadi, "A New Battery/Ultr-Capacitor Hybrid Energy Storage for Electic, Hybrid and Plug-in Hybrid Electric Vehicles," in *IEEE Vehicle Power and Propulsion Conference*, Dearborn, MI, USA, pp. 941-946, 2009.

[25] Z. Song, J. Li, X. Han, L. Xu, L. Lu, M. Ouyang and H. Hofmann, "Multi-objective optimization of a semi-active battery/supercapacitor energy storage system for electric vehicles," *ELSEVIER Applied Energy,* vol. 135, pp. 212-224, 2014.

[26] A. Ostadi, "Optimal Sizing of Battery/Ultracapacitor-Based Energy Storage Systems," in *PhD thesis*, University of Waterloo, Waterloo, Canada, 2015.

[27] K. Zhuge, "Development of an Efficient Hybrid Energy Storage System (HESS) for Electric and Hybrid Electric Vehicles," in *Mater thesis*, Waterloo, Canada, 2013.

[28] Z. Song, H. Hofmann, J. Li, X. Han, X. Zhang and M. Ouyang, "A comparison study of different semi-active hybrid energy storage system topologies for electric vehicles," *ELSEVIER Journal of Power Soureces,* vol. 274, pp. 400-411, 2015.

[29] A. Khaligh and Z. Li, "Battery, Ultracapacitor, Fuel Cell, and Hybrid Energy Storage Systems for Electric, Hybrid Electric, Fuel Cell, and Plug-In Hybrid Electric Vehicles: State of the Art," *IEEE Transaction on Vehicular Technology,* vol. 59, no. 6, pp. 2806-2814, 2010.

[30] F. R. Kalhammer, B. M. Kopf, D. H. Swan, V. P. Roan and M. P. Walsh, "Status and Prospects for Zero Emissions Vehicle Technology Report of the ARB Independent Expert Panel 2007," State of California Air Resources, Sacramento, California, USA, 2007.

[31] M. Shnayerson, The Car That Could: The Inside Story of GM's Revolutionary Electric Vehicle, New York: Random House, 1996.

[32] "Battery University," 2016. [Online]. Available: http://batteryuniversity.com/learn/article/secondary_batteries. [Accessed 20 April 2016].

[33] "CAA Electric Vehicles," 2016. [Online]. Available: http://electricvehicles.caa.ca/electric-vehicles-available-in-canada/. [Accessed 20 April 2016].

[34] A. Dinger, R. Matrin, X. Mosquet, M. Rabl, D. Rizoulis, M. Russo and G. Sticher, "Batteries for Electric Cars Challenges, Opprotunities, and the Outlook to 2020," The Boston Consulting Group, Boston, Massachusetts, USA, 2010, https://www.bcg.com/documents/file36615.pdf.

[35] L. Lam and P. Bauer, "Practical Capacity Fading Model for Li-Ion Battery Cells in Electric Vehicles," *IEEE Transactions on Power Electronics,* vol. 28, no. 12, pp. 5910-5918, 2013.

[36] L. Lam, P. Bauer and E. Kelder, "A Practical Circuit-based Model for Li-ion Battery Cells in Electric Vehicle Applications," in *IEEE 33rd International Telecommunications Energy Conference*, Amesterdam, Netherlands, pp. 1-9, 2011.

[37] "APR18650 Li-ion battery cell datasheet," A123 Systems, 2009, http://www.batteryspace.com/prod-specs/6612.pdf. [Accessed June 2016].

[38] G.-A. Nazri and G. Pistoia, Lithium Batteries: Science and Technology, Springer, 2009.

[39] M. Chen and G. A. Rincon-Mora, "Accurate Electrical Battery Model Capable of Predicting Runtime and I–V Performance," *IEEE Transactions on Energy Conversion,* vol. 21, no. 2, pp. 504-511, 2006.

[40] H. E. Perez, J. B. Siegel, X. Lin, A. G. Stefanopoulou, Y. Ding and M. P. Castanier, "Parameterization and Validation of an Integrated Electro-Thermal Cylindrical LFP Battery Model," in *ASME 5th Annual Dyanmic Systems and Control Conference*, Fort Lauderdale, Florida, USA, 2012.

[41] X. Lin, H. E. Perez,, J. B. Siegel, A. G. Stefanopoulou,, Y. Li, D. Anderson, Y. Ding and M. P. Castanier, "Online Parameterization of Lumped Thermal Dynamics in Cylindrical Lithium Ion Batteries for Core Temperature Estimation and Health Monitoring," *IEEE Transaction on Control Systems Technology,* vol. 21, no. 5, pp. 1745-1755, 2013.

[42] "ANR26650 Li-ion battery cell datasheet," A213 Systems, 2011, http://www.a123systems.com/Collateral/Documents/English-US/A123%20Systems%20ANR26650%20Data%20Sheet.pdf. [Accessed June 2016].

[43] E. Tironi and V. Musolino, "Supercapacitor characterization in power electronic applications: Proposal of a new model," in *Clean Electric Power*, Capri, Italy, pp. 276-382, 2009.

[44] "Nissan," Nissan, 2016. [Online]. Available: http://www.nissanusa.com/. [Accessed 1 September 2015].

[45] "Combustion Engines Information," IEEE, 2016. [Online]. Available: http://www.globalspec.com/learnmore/motion_controls/engines_components/industrial_engines. [Accessed 13 June 2016].

[46] S. J. Chapman, Electrical Machinery and Power System Fundamentals, McGraw-Hill, 2002.

[47] R. M. Schupbach and J. C. Balda, "Comparing DC-DC Converters for Power Management in Hybrid Electric Vehicles," in *IEEE Electric Machines and Drives Conference*, Madison, Wisconsin, USA, pp. 1369-1374, 2003.

[48] D. Graovac and M. Purshel, "IGBT Power Losses Calculation Using the Data-Sheet Parameters," Infineon Application note, 2009, https://www.element14.com/community/docs/DOC-20553/l/igbt-power-losses-calculation-using-the-data-sheet-parameters. [Accessed June 2016].

[49] "SKM 300GB066D IGBT module," Semikron, https://www.semikron.com/dl/service-support/downloads/download/semikron-datasheet-skm300gb066d-21915520.

[50] U. Nicolai and A. Wintrich, "Application Note AN 1403: Determining switching losses of SEMIKRON IGBT modules," Semikron, 2014, https://www.semikron.com/dl/service-support/downloads/download/semikron-application-note-an-1403-switchinglosses-en. [Accessed June 2016].

[51] L. Guzzella and A. Sciarretta, Vehicle Propulsion Systems Introduction to Modeling and Optimization, Berlin: Springer, 2013.

[52] "Automobile drag coefficiency," Wikipedia, 2016. [Online]. Available: https://en.wikipedia.org/wiki/Automobile_drag_coefficient#cite_note-107. [Accessed December 2015].

[53] "Living LEAF," 2016. [Online]. Available: http://livingleaf.info/2010/11/nissan-leaf-electric-motor-and-transmission/. [Accessed January 2016].

[54] "SmartPower Stacks 50 kW DC-DC Cconverter datasheet," Methode Electronics, 2014, http://www.methode.com/Documents/TechnicalLibrary/SmartPower_Stack_50kW_DC-DC_L1_Spec_Sheet_v6_2014-09-03.pdf. [Accessed June 2016]].

[55] X. Jia, D. Xu, S. Du, C. Hu, M. Chen and P. Lin, "A High Power Density and Efficiency Bi-Directional DC/DC Converter for Electric Vehicles," in *9th International Conference on Power Electronics and ECCE Asia*, Seoul, pp. 874-880, 2015.

[56] A. Tazdani and R. Iravani, Voltage-Sourced Converters in Power Systems: Modeling, Control, and Applications, Wiley, 2010.

[57] "Mouser Electronics," Maxwell Technologies, 2016. [Online]. Available: http://www.mouser.com/ProductDetail/Maxwell-Technologies/BCAP0350-E270-T11/?qs=SLym9Mzz6zOkA1n1aMfE2Q%3d%3d. [Accessed 22 May 2016].

[58] "buylithiumbatteries," 2016. [Online]. Available: http://www.buylithiumbatteries.com/ANR26650_Lithium_Ion_Cylindrical_Cell_p/disc-300475-306.htm. [Accessed 22 May 2016].

[59] A. Ostadi and M. Kazerani, "Hybrid Energy Storage System (HESS) in Vehicular Applications: A Review on Interfacing Battery and Ultra-capacitor Units," in *IEEE Transportation Electrification Conference and Expo*, Detroit, MI, pp. 1-7, 2013.

[60] A. Ostadi and M. Kazerani, "A Comparative Analysis of Optimal Sizing of Battery-Only, Ultracapacitor-Only, and Battery–Ultracapacitor Hybrid Energy Storage Systems for a City Bus," *IEEE Transactions on Vehicular Technology,* vol. 64, no. 10, pp. 4449-4460, 2015.

[61] A. Abuaish and M. Kazerani, "Comparative Evaluation of Partially-Decoupled Battery-Supercapacitor HESS Topologies for EVs from Battery Pack Capacity Fading Viewpoint," in *IEEE Transportation Electrification Conference and Expo*, Dearborn, MI, 2016.

[62] *Electric Vehicle Charing Stations Technical Installation Guide.* [Performance]. Hydro Quebec, 2015, http://www.hydroquebec.com/transportation-electrification/pdf/technical-installation-guide.pdf. [Accessed June 2016].

[63] J. Morris, "Design and Testing of a Bidirectional Smart Charger Prototype," in *MASc thesis*, Univerisity of Waterloo, 2015.

[64] Z. Alnasir and M. Kazerani, "A small-scale standalone wind energy conversion system featuring SCIG, CSI and a novel storage integration scheme," *ELSEVIER, Renewable Energy ,* vol. 89, pp. 360-370, 2015.

[65] "Anhui Hummer Dynamo 10 kW wind inverter datasheet," 2014. [Accessed a hardcopy provided by the company].

[66] "Why Toyota will offer two battery choices in the 2016 Prius," ecomento, 27 November 2015. [Online]. Available: http://ecomento.com/2015/11/27/why-toyota-will-offer-two-battery-choices-in-the-2016-prius/. [Accessed 4 May 2016].

[67] Z. Song, H. Hofmman, J. Li, X. Han and X. Zhang, "A Comparison Study of Different Semi-active Hybrid Energy Storage System Topologies for Electric Vehicles," *ELSEVIER Journal of Power Sources,* vol. 274, pp. 400-411, 2015.